

## University of Southampton Research Repository ePrints Soton

Copyright © and Moral Rights for this thesis are retained by the author and/or other copyright owners. A copy can be downloaded for personal non-commercial research or study, without prior permission or charge. This thesis cannot be reproduced or quoted extensively from without first obtaining permission in writing from the copyright holder/s. The content must not be changed in any way or sold commercially in any format or medium without the formal permission of the copyright holders.

When referring to this work, full bibliographic details including the author, title, awarding institution and date of the thesis must be given e.g.

AUTHOR (year of submission) "Full thesis title", University of Southampton, name of the University School or Department, PhD Thesis, pagination

**UNIVERSITY OF SOUTHAMPTON**

FACULTY OF PHYSICAL SCIENCES AND ENGINEERING

Optoelectronics Research Centre

**Waveguide Lasers in Ytterbium Doped Tantalum  
Pentoxide for Integrated Photonic Circuits**

By

**Armen Aghajani**

Thesis for the degree of Doctor of Philosophy

September 2015



UNIVERSITY OF SOUTHAMPTON

ABSTRACT

FACULTY OF PHYSICAL SCIENCES AND ENGINEERING

Doctor of Philosophy

Thesis for the degree of Doctor of Philosophy

**Waveguide Lasers in Ytterbium Doped Tantalum Pentoxide for Integrated Photonic  
Circuits**

By Armen Aghajani

This thesis investigates ytterbium doped tantalum pentoxide as a material system for realising waveguide lasers on silicon substrate, as a basis to provide the next generation of mass-producible, low-cost planar devices with many interlocking photonic circuits for multi-functionality.

Numerical modelling of symmetrical rib waveguide in Ta<sub>2</sub>O<sub>5</sub> was carried out finding an optimum waveguide design for a near-circular mode profile with maximum confinement of light within the core with various etch depths and rib widths. A numerical study investigating the feasibility of integrated Kerr lens elements for future mode-locking was carried out, predicting that a Kerr lens slab with a length of 20 μm with input and out waveguides was able to achieve a 9% modulation depth for input intensity of 6 GW/m<sup>2</sup>.

Thin films were fabricated by RF magnetron sputtering onto a silicon substrate with 2.5 μm silica layer from a powder pressed Yb:Ta<sub>2</sub>O<sub>5</sub> target, with shallow rib waveguides realised using photolithography and ion beam milling. The excited-state lifetime of Yb:Ta<sub>2</sub>O<sub>5</sub> was measured to be 0.25 ± 0.03 ms, and peak emission and absorption cross-sections were determined to be 2.9 ± 0.7 × 10<sup>-20</sup> cm<sup>2</sup> and 2.75 ± 0.2 × 10<sup>-20</sup> cm<sup>2</sup> respectively, with the fluorescence spectrum giving a broadband emission from 990 nm to 1090 nm.

Finally a 10.8 mm long waveguide laser in Ta<sub>2</sub>O<sub>5</sub> doped with ≈ 6.2 × 10<sup>20</sup> Yb atoms/cm<sup>3</sup> of ytterbium oxide was demonstrated with a laser cavity formed from a combination of high reflective mirrors with output couplers or reflections from the bare end-facets with Fresnel reflectivity of 12%. In a 5.4 μm wide waveguide, lasing was observed between 1015 nm and 1030 nm when end-pumped with a 977 nm laser diode with the highest output power of 25 mW at a wavelength of 1025 nm with an absorbed pump power of 120 mW for a cavity formed by a high reflector mirror and a bare end-facet at the output. In this case, the absorbed pump power threshold and slope efficiency were measured to be ≈ 30 mW and ≈ 26% respectively. The results presented in this thesis demonstrate that tantalum pentoxide has great potential for mass-producible, integrated optical circuits on silicon using conventional CMOS fabrication technologies.



# Table of Contents

Table of Contents .....	i
List of Figures .....	v
List of Tables .....	ix
Declaration of Authorship.....	xi
Acknowledgements .....	xiii
Nomenclature .....	xv
List of Publications .....	xvii
CHAPTER 1 Introduction.....	1
1.1 Motivations .....	1
1.2 Project aims.....	2
1.3 Material selection.....	2
1.4 Achievements and synopsis of the thesis .....	3
1.5 Review of ytterbium doped waveguide lasers.....	4
1.5.1 Rare-earth doped waveguide lasers.....	4
1.5.2 Ytterbium doped waveguide lasers .....	7
1.6 Conclusion .....	10
1.7 Bibliography.....	11
CHAPTER 2 Planar Waveguides and Devices in Tantalum Pentoxide.....	17
2.1 Introduction.....	17
2.2 Optical waveguide theory and operation.....	18

2.3	Approximate theoretical methods for analysis and design of rib structured waveguides	24
2.3.1	Single mode condition for rib waveguides	24
2.3.2	Effective index method	26
2.4	Simulations of mode profiles of rib waveguides	27
2.5	Simulations of integrated planar Kerr lens in Ta <sub>2</sub> O <sub>5</sub>	34
2.6	Conclusion	39
2.7	Bibliography	40
CHAPTER 3	Yb:Ta <sub>2</sub> O <sub>5</sub> Waveguide Fabrication and Characterisation	43
3.1	Introduction	43
3.2	Fabrication of Yb:Ta <sub>2</sub> O <sub>5</sub> rib waveguides	43
3.2.1	Inspection and cleaning of substrate (Wafer preparation)	45
3.2.2	Yb:Ta <sub>2</sub> O <sub>5</sub> core layer	45
3.2.3	Silica over clad layer	49
3.2.4	Dicing and optical polishing of end-facets	49
3.2.5	Fabrication results	50
3.3	Mode profile simulation of sloped edge rib waveguides	51
3.4	Characterisation and analysis of mode intensity profiles	53
3.5	Optical loss measurements	56
3.5.1	Transmission measurements at 1064 nm	56
3.5.2	Fabry-Perot propagation loss analysis	60
3.6	Conclusion	63
3.7	Bibliography	64
CHAPTER 4	Spectroscopy of Yb:Ta <sub>2</sub> O <sub>5</sub> Waveguides	67
4.1	Introduction	67
4.1.1	Ytterbium rare-earth ion	67

4.2	Absorption spectrum and cross-section.....	68
4.3	Emission spectrum and cross-section.....	70
4.4	Excited-state lifetime .....	74
4.5	Discussion .....	75
4.6	Conclusion .....	76
4.7	Bibliography.....	77
CHAPTER 5 CW Yb:Ta <sub>2</sub> O <sub>5</sub> Waveguide Lasers .....		79
5.1	Introduction.....	79
5.2	Basic principles of operation for Yb-doped lasers .....	80
5.2.1	Basic principles of laser operation .....	80
5.2.2	Theory of quasi-three-level lasers .....	82
5.3	Experimental set-up for waveguide laser performance characterisation.....	88
5.3.1	Determination of launch efficiency of experimental set-up.....	88
5.4	Continuous wave laser performance .....	93
5.5	Yb:Ta <sub>2</sub> O <sub>5</sub> laser spectrum.....	95
5.6	Conclusion .....	97
5.7	Bibliography.....	98
CHAPTER 6 Conclusion and Future Work .....		101
6.1	Conclusion .....	101
6.2	Future work.....	103
6.3	Bibliography.....	105
Appendix A	Matlab code for determination of FWHM of Gaussian beam profile .....	107
Appendix B	Background theory of knife edge method .....	109



# List of Figures

Figure 2.1 Optical waveguide side 2D schematic illustrating the over-cladding, waveguide core and under-cladding typical for planar structures.....	19
Figure 2.2 2D cross-section of planar waveguide, showing the dimensional parameters considered when designing a slab waveguide.....	21
Figure 2.3 TE modes normalised dispersion curves plotted using equation (2.30). ....	23
Figure 2.4 Examples of different waveguide cross-sections.....	24
Figure 2.5 A Ta <sub>2</sub> O <sub>5</sub> rib waveguide cross-section where the dimensions are represented by $W$ (width of the waveguide), $H$ (rib height), $D$ (etch depth) and $h$ (slab region height).....	25
Figure 2.6 Single mode condition for $\alpha = 0$ and $\alpha = 0.3$ . ....	25
Figure 2.7 Effective index method.....	26
Figure 2.8 Rib waveguide structure showing the dimensions and materials properties used in the COMSOL model. ....	27
Figure 2.9 COMSOL simulated rib waveguide mode profile. Rib dimensions: height $H = 1 \mu\text{m}$ , width $W = 2 \mu\text{m}$ and etch depth $D = 150 \text{ nm}$ . ....	28
Figure 2.10 Fundamental mode profile of rib waveguide with height $H = 1 \mu\text{m}$ , width $W = 2 \mu\text{m}$ and etch depth $D = 150 \text{ nm}$ with cut line (white dotted line) in a) horizontal direction, $wy$ & c) vertical direction, $wx$ along with the corresponding normalised electric fields in b) horizontal direction, $wy$ & d) vertical direction, $wx$ . ....	29
Figure 2.11 Normalised electric field with arrows illustrating direction of electric (white) and magnetic field (black) for polarisations a) quasi-TM & c) quasi-TE, along with the corresponding vertical and horizontal components of the electric field for polarisations b) quasi-TM & d) quasi-TE. Rib dimensions: height $H = 1 \mu\text{m}$ , width $W = 2 \mu\text{m}$ and etch depth $D = 500 \text{ nm}$ . ....	30
Figure 2.12 Fundamental mode effective indices for quasi-TM polarisation of rib waveguides with etch depths of a) 150 nm, b) 300 nm, c) 500 nm, & d) 1 $\mu\text{m}$ . ....	31
Figure 2.13 Comparison of effective indices for different etch depths from COMSOL simulation and effective index method. Width $w = 0.3 \mu\text{m}$ . ....	32
Figure 2.14 FWHM of spot sizes in the horizontal and vertical direction for a rib with 150 nm etch depth.....	32
Figure 2.15 FWHM of spot sizes in the horizontal and vertical direction for a rib with 300 nm etch depth.....	33
Figure 2.16 FWHM of spot sizes in the horizontal and vertical direction for a rib with 500 nm etch depth.....	33

Figure 2.17 FWHM of spot sizes in the horizontal and vertical direction for a rib with 1 $\mu\text{m}$ etch depth. ....	33
Figure 2.18 Self-focusing mechanism of wave front passing through $\chi^{(3)}$ medium utilizing the Kerr effect. ....	34
Figure 2.19 2D top down view of planar Kerr lens element in $\text{Ta}_2\text{O}_5$ enclosed in $\text{SiO}_2$ over- and under-cladding. ....	35
Figure 2.20 COMSOL electric field simulation of planar Kerr element showing the light diffracting within Kerr element. Dimensions of the model: input and output waveguide widths, $W = 1 \mu\text{m}$ & Kerr element length, $K_L = 300 \mu\text{m}$ . Input intensity, $I = 1.5 \text{ GW/m}^2$ . White dotted lines highlight the boundary between outer slab regions and inner rib and Kerr element. ....	36
Figure 2.21 FWHM of the spot sizes in the y direction (horizontal direction of a rib waveguide cross-section) of the propagating along the Kerr element for various input intensities. ....	37
Figure 2.22 COMSOL electric field simulation of planar Kerr element showing self-focusing as input intensity is increased. The beam propagating along the Kerr element is shown for input intensities a) $I = 1.5 \text{ GW/m}^2$ , & b) $I = 8 \text{ GW/m}^2$ . ....	38
Figure 2.23 Coupling efficiency between input and output waveguides of the Kerr element as length ( $K_L$ ) is increased, for increasing input intensities. ....	39
Figure 2.24 Coupling efficiency between input and output waveguides of the Kerr element as input intensity is increased, for different Kerr element lengths ( $K_L$ ). ....	39
Figure 3.1 Partially etched rib waveguide structure with intended fabrication dimensions. ....	44
Figure 3.2 RF sputtering process for thin film material deposition. ....	46
Figure 3.3 2D cross sectional presentation of photolithography process. ....	48
Figure 3.4 Argon ions attacking the unprotected areas of $\text{Yb}:\text{Ta}_2\text{O}_5$ . ....	48
Figure 3.5 Enhanced SEM cross-section image of fabricated $\approx 5 \mu\text{m}$ wide waveguide, a) showing the different layers of thin film material, b) zoomed in section highlighting the double sloped side wall. ....	50
Figure 3.6 Cross-section of the ideal straight edged rib waveguide and the sloped fabricated rib waveguide. ....	51
Figure 3.7 COMSOL simulation of the electric field of the fundamental mode of a rib waveguide with an etch depth of 150 nm for a rib width of 1 $\mu\text{m}$ : a) sloped edge rib waveguide; c) straight edge rib waveguide & COMSOL simulation of the mode intensity profiles for the fundamental mode in the horizontal and vertical directions for a rib waveguide with an etch depth of 150 nm for a rib width of 1 $\mu\text{m}$ : b) sloped edged rib waveguide; d) straight edge rib waveguide. ....	52
Figure 3.8 Comparison between straight and sloped side walls simulated FWHM mode intensity profiles at 980 nm. ....	53
Figure 3.9 Comparison between straight and sloped side walls simulated effective indices at 980 nm. ....	53
Figure 3.10 Free space set-up of $\text{Yb}:\text{Ta}_2\text{O}_5$ waveguide modal profile characterization. ....	54
Figure 3.11 Mode intensity profile of rib waveguide with a width of 1 $\mu\text{m}$ , captured with camera. ....	54
Figure 3.12 Mode intensity profiles in a) vertical and b) horizontal directions for various rib widths. ....	55

Figure 3.13 Experimental set-up for transmission loss measurement at 1064 nm.....	56
Figure 3.14 Illustration of top down view of laser diode pig-tailed fibre launching laser.....	57
Figure 3.15 COMSOL simulation comparison of FWHM of the fundamental mode intensity profiles in the horizontal and vertical directions between laser pump (980 nm) and transmission measurement wavelength (1064 nm). ....	59
Figure 3.16 Theoretical model of coupling efficiency between 1064 nm input laser beam (FWHM MFD, $w_0= 6.2 \mu\text{m}$ ) and mode intensity profiles of rib waveguide found with COMSOL simulations. ....	59
Figure 3.17 Coupling efficiencies for different rib widths when minimum beam waist of the 1064 nm laser output fibre is at position $z \approx 0$ from the waveguide end-facet, assuming perfect alignment (x, y). ....	60
Figure 3.18 FP loss measurement experimental set-up.....	61
Figure 3.19 Propagation loss measurement in Yb:Ta <sub>2</sub> O <sub>5</sub> rib waveguide using the FP method. Data plotted for a waveguide with a width of 10 $\mu\text{m}$ . ....	62
Figure 3.20 Propagation loss measurement in Yb:Ta <sub>2</sub> O <sub>5</sub> rib waveguide using the FP method for all waveguides measured, showing the variation in the measurements taken.....	63
Figure 4.1 Energy level diagram for Yb:YAG laser .....	68
Figure 4.2 Set-up of Yb:Ta <sub>2</sub> O <sub>5</sub> waveguide absorption spectrum analysis. ....	69
Figure 4.3 Yb:Ta <sub>2</sub> O <sub>5</sub> attenuation spectrum of a 3 mm long sample.....	69
Figure 4.4 Yb:Ta <sub>2</sub> O <sub>5</sub> absorption cross-section.....	70
Figure 4.5 Set-up of Yb:Ta <sub>2</sub> O <sub>5</sub> waveguide fluorescence spectrum analysis.....	71
Figure 4.6 Fluorescence Spectrum of Yb:Ta <sub>2</sub> O <sub>5</sub> waveguide.....	72
Figure 4.7 Absorption and emission cross-sections of ytterbium ions in Ta <sub>2</sub> O <sub>5</sub> waveguide. The emission cross-section was calculated from the absorption cross-section using McCumber theory. ....	73
Figure 4.8 Emission cross-section spectrum scaled in accordance with to McCumber analysis applied to the absorption cross-section. ....	73
Figure 4.9 Experimental set-up for the analysis of excited-state lifetime for ytterbium ions in Ta <sub>2</sub> O <sub>5</sub> waveguides.....	74
Figure 4.10 Radiative decay curve with multi-exponential fit.....	75
Figure 5.1 Light absorption and emission for two-level model .....	80
Figure 5.2 Schematic of a typical laser system, showing the three most important components; pump source, gain medium, & optical cavity.....	81
Figure 5.3 Longitudinal modes of an optical cavity formed by two mirrors. ....	82
Figure 5.4 Energy level diagram of a typical quasi-three-level laser.....	83
Figure 5.5 Theoretical laser threshold vs. cavity length for cavity with a HR mirror and 10% OC, with zoomed in insert.....	86

Figure 5.6 Theoretical laser slope efficiency vs. output coupler transmission for various propagation losses. ....	87
Figure 5.7 Experimental set-up for laser characterization of Yb:Ta <sub>2</sub> O <sub>5</sub> with high reflector (HR) mirror and output coupler (OC) with top down view of waveguide device. ....	88
Figure 5.8 Razor edge of a blade moving across a beam. ....	89
Figure 5.9a) 3D Gaussian beam distribution with partial beam coverage, b) optical power vs. position of the razor blade [29]. ....	89
Figure 5.10 Experimental set-up for knife edge method with the razor blade moving across the investigated beam in the <i>x</i> axis for different positions from the lens along the <i>z</i> axis. ....	90
Figure 5.11 Complementary error function fit for knife edge scan of beam at a <i>z</i> = 2.0 mm giving a 1/e <sup>2</sup> radius of 115 μm. ....	90
Figure 5.12 Gaussian beam waist fit of beam radius (1/e <sup>2</sup> ), <i>w</i> found from the ....	91
Figure 5.13 Theoretical model of coupling efficiency between 980 nm input laser beam (FWHM MFD, <i>w</i> <sub>0</sub> = 0.81 μm) and mode intensity profiles of rib waveguide found with COMSOL simulations. ....	92
Figure 5.14 Maximum coupling efficiencies for different rib widths when minimum beam waist of the 980 nm laser focused with aspheric lens is at position <i>z</i> ≈ 0 mm (minimum beam waist) from the waveguide end-facet. ....	93
Figure 5.15 Mode intensity profiles for 5.4 μm wide waveguide of a) both the pump and lasing wavelengths, and b) only the lasing wavelength. Image taken with Hamamatsu C2741-03 camera with 40x microscope objective collection lens. ....	93
Figure 5.16 Laser output power vs absorbed pump power plotted for different mirror configurations with calculated coupling efficiency of 44%. Mirror configurations used: a) EF/EF & EF/HR, b) 10%OC/HR & 5%OC/HR. ....	94
Figure 5.17 Lasing spectrum of Yb:Ta <sub>2</sub> O <sub>5</sub> waveguide with a width of 5.4 μm, focusing around region lasing occurs with lasing spectrum development just below (blue) and above (yellow) threshold for cavity formed with a HR mirror and 5% OC. ....	95
Figure 5.18 Lasing spectra for different width waveguides of a cavity formed from a HR mirror and 5% OC with waveguides widths of a) 4 μm, b) 5.4 μm (from figure 5.17), c) 6 μm, d) 7 μm, e) 8 μm, & f) 9 μm. ....	96
Figure B.1 Knife edge scans at various distances from the input aspheric lens. ....	110

# List of Tables

Table 1.1 Comparison of the material and laser properties of some recently realised Yb-doped waveguide lasers. <i>*These cross-sections have been extracted from diagrams in the literature as accurately as possible</i> .....	8
Table 2.1 Units and numerical values of Maxwells equations.....	18
Table 2.2 Classification of the types of longitudinal compents .....	21
Table 2.3 Dimensional and material properties of Ta <sub>2</sub> O <sub>5</sub> Kerr element used in the simulation of planar Kerr element. The dimensions of the rib waveguide ( <i>H</i> , <i>D</i> , & <i>W</i> ) used to calculate the effective indices of the inner rib region and outer slab region used in the Kerr lens simulations are in blue.....	36
Table 3.1 Sputtering chamber conditions for Yb:Ta <sub>2</sub> O <sub>5</sub> deposition.....	46
Table 3.2 Sputtering chamber conditions for SiO <sub>2</sub> deposition.....	49
Table 3.3 Transmission loss measurement data.....	60
Table 3.4 Waveguides and their corresponding propagation losses calculated using the FP method at different centre wavelengths. ....	63
Table 4.1 Comparison of the spectroscopic properties of the Yb:Ta <sub>2</sub> O <sub>5</sub> studied in this work (red) with other Yb-doped glass (blue) and crystal (green) material systems. <i>*These cross-sections have been extracted from diagrams in the literature as accurately as possible</i> .....	76
Table 5.1 Values established from complementary error function fit.....	91
Table 5.2 Laser parameters for different mirror configurations established experimentally and estimated theoretically. ....	94



# Declaration of Authorship

I, Armen Aghajani declare that this thesis entitled “*Waveguide Lasers in Ytterbium Doped Tantalum Pentoxide for Integrated Photonic Circuits*” and the work presented in it are my own and have been generated by me as the result of my own original research.

I confirm that:

1. This work was done wholly or mainly while in candidature for a research degree at this University;
2. Where any part of this thesis has previously been submitted for a degree or any other qualification at this University or any other institution, this has been clearly stated;
3. Where I have consulted the published work of others, this is always clearly attributed;
4. Where I have quoted from the work of others, the source is always given. With the exception of such quotations, this thesis is entirely my own work;
5. I have acknowledged all main sources of help;
6. Where the thesis is based on work done by myself jointly with others, I have made clear exactly what was done by others and what I have contributed myself;
7. Either none of this work has been published before submission, parts of this work have been published as [please see List of Publications]:

Signed: .....

Date:.....



# Acknowledgements

I would like to begin by thanking my supervisor, James S Wilkinson for being a fantastic mentor and giving me the opportunity to work on this fascinating project. Thank you for putting up with my continuous visits to your office to ask random questions that have occurred to me, for without your support and guidance my PhD could not have happened. Thank you for all the lunches and dinners you bought during trips to Nice and Paris, with all the interesting discussions that occurred after a few drinks.

I would like to show my appreciation to Vasilis Apostolopoulos for being a great co-supervisor and friend with your guidance and help during my PhD. Thank you for all the great work and non-work related discussions and all the small helpful tips in the labs for when I was stuck. I would also like to thank the Terahertz group members Paul Gow, Lewis Maple, Elena Mavrona, Sam Berry, Jo Carty, Duncan McBryde, Mark Barnes and Geoff Daniell for making me feel welcome into the group, even though I would only appear once a week for group meetings. I am glad that we were able to get to know each other better and have an amazing time as a group in Munich.

I would like to thank Senthil G Murugan because his important support and knowledge has helped me immensely in completing my PhD. Thanks for all the useful discussions and advice for the work in the cleanroom and in the labs, and for being a good drinking partner outside of office. Many thanks to Neil Sessions for his amazing support and advice in the cleanrooms and in the SEM lab.

I would like to thank the rest of my group members of Integrated Photonic Devices group, Dave Rowe, Jonathan Butement, Vinita Mittal, Amy Tong, Alina Karabchevsky, Shahab Bakhtiari Gorajoobi and of course my lab buddy Mohd Narizee, that have helped with support in the labs and with their friendship making my PhD experience a fantastic one.

Many thanks to Olav Hellesø and his group for their warm welcome during my trip to Tromsø in Norway for help with my COMSOL modelling of planar Kerr lenses. I had a lot of fun, especially the lunch time visits to the underground archive room where daily table tennis matches occurred, my first attempt at fishing, my first experience of midnight sun and of course the Friday group meetings which always had great tasting cakes.

I would like to extend my gratitude to Ping Hua for teaching and helping me with the tedious task of polishing and Amol Choudhary for teaching me the fine art of placing mirrors on to the end of waveguides. I would like to thank Michalis Zervas for so many stimulating discussions on lasers, helping me to understand my results.

And finally I would like to thank my sisters and my parents for giving me the tremendous support during my life and giving me the drive to succeed during the good and bad times for without them I would never have pursued this work in this extremely interesting field.

# Nomenclature

ASE	Amplified spontaneous emission
CCD	Charge-coupled device
CMOS	Complementary-metal–oxide–semiconductor
Cr	Chromium
DFB	Distributed feedback grating
DFS	Distributed feedback system
Er	Erbium
FHD	Flame hydrolysis deposition
FP	Fabry-Perot
FSR	Free spectral range
FWHM	Full width at half maximum
Ho	Holmium
HR	High reflective
IBM	Ion beam milling
IC	Integrated circuit
IPA	Isopropyl alcohol
IR	Infrared radiation
KLM	Kerr lens modelocking
KOH	Potassium hydroxide
LD	Laser diode
LPE	Liquid phase epitaxy
MM	Multimode

NA	Numerical aperture
Nd	Neodymium
ND	Neutral density
OC	Output coupler
OSA	Optical spectrum analyser
PMF	Polarization maintaining fibre
PSF	Point spread function
RF	Radio-frequency
RIE	Reactive ion etching
SEM	Scanning electron microscope
SESAM	Semiconductor saturable absorber mirror
SM	Single mode
TE	Transverse electric
TLS	Tuneable laser source
TM	Transverse magnetic
Tm	Thulium
ULI	Ultrafast laser inscribing
UV	Ultraviolet
Yb	Ytterbium

# List of Publications

## Journals

1. **A. Aghajani**, G. S. Murugan, N. P. Sessions, S. J. Pearce, V. Apostolopoulos and J. S. Wilkinson, “*Spectroscopy of ytterbium-doped tantalum pentoxide rib waveguides on silicon*,” *Optical Materials Express*, Vol.4 (8) pp.1505-1514 (2014).
2. D. McBryde, P. Gow, S. A. Berry, M. E. Barnes, **A. Aghajani** and V. Apostolopoulos, “*Multiple double-metal bias-free terahertz emitter*,” *Applied Physics Letters*, Vol.104 pp. 201108 (2014).
3. V. Mittal, **A. Aghajani**, L. G. Carpenter, J. C. Gates, J. Butement, P. G. R. Smith, J. S. Wilkinson, G. S. Murugan, “*Fabrication and characterization of high-contrast mid-infrared GeTe<sub>4</sub> channel waveguides*,” *Optics Letters*, Vol.40(9) pp.2016-2019 (2015).
4. **A. Aghajani**, G. S. Murugan, N. P. Sessions, V. Apostolopoulos and J. S. Wilkinson, “*Waveguide lasers in ytterbium-doped tantalum pentoxide on silicon*,” *Optics Letters*, Vol.40(11) pp.2549-2552 (2015).

## Conferences

1. **A. Aghajani**, G. S. Murugan, N. P. Sessions, V. Apostolopoulos and J. S. Wilkinson, “*Ytterbium-doped tantalum pentoxide waveguides: spectroscopy for compact waveguide lasers*,” *Advanced Solid State Lasers (ASSL)*, Paris, France, AM4A.38 (2013).
2. **A. Aghajani**, G. S. Murugan, N. P. Sessions, V. Apostolopoulos and J. S. Wilkinson, “*Ytterbium-doped tantalum pentoxide waveguide lasers*,” *European Conference on Integrated Optics and Microoptics Conference (ECIO-MOC)* Nice, France (2014).
3. **A. Aghajani**, G. S. Murugan, N. P. Sessions, V. Apostolopoulos and J. S. Wilkinson, “*Spectroscopy of high index contrast Yb:Ta<sub>2</sub>O<sub>5</sub> waveguides for lasing applications*,” *Sixth International Conference on Optical, Optoelectronic and Photonic Materials and Applications (ICOOPMA '14)* Leeds, England (2014).
4. **A. Aghajani**, G. S. Murugan, N. P. Sessions, V. Apostolopoulos and J. S. Wilkinson, “*CMOS-Compatible High Index Contrast Ytterbium-Doped Tantalum Pentoxide Rib Waveguide Lasers*,” *European Conference on Lasers and Electro-Optics (CLEO Europe)* Munich, Germany, CJ-P.27 (2015).
5. C. Lacava, **A. Aghajani**, P. Hua, D. J. Richardson, P. Petropoulos and J. S. Wilkinson, “*Nonlinear Optical Properties of Ytterbium-doped Tantalum Pentoxide rib Waveguides on Silicon at Telecom Wavelengths*,” *Optical Fiber Communication Conference and Exposition (OFC)* Anaheim, California, USA (2016).



*Dedicated to my family*



# CHAPTER 1

## Introduction

### 1.1 Motivations

Optical waveguides in planar and channel formats offer many advantages for laser systems include maintaining a high optical intensity due to no beam divergence, leading to achieving high optical gain and gain efficiency when pumped at low power. Furthermore, the waveguide geometry gives the opportunity to tailor the size of the propagating modes for the pump and laser beam propagating in the waveguide and increase the overlap of pump and laser waveguide modes, which causes the laser threshold to reduce [1]. Additionally the waveguide geometry can be tailored to control the group-velocity dispersion within the channel [2] which is important for increasing the effectiveness of several nonlinear optical processes such as, soliton-effect pulse compression (compression of pulse based on initial narrowing phase before higher order solitons form their original shape at multiples of the soliton period), four-wave mixing (interaction of two wavelengths produces two additional wavelengths normally known as “signal and idlers”) [3], and soliton generation (pulse that maintains its shape while propagating at constant velocity caused as a result of nonlinear and dispersive effects within the medium cancelling one another) [4]. Waveguide lasers have the added benefits of being optically pumped by a low cost laser diode for lasing in regions where diode lasers do not exist or perform poorly [5], and have a high degree of thermal immunity as planar structures have beneficial temperature dissipation geometry [6]. The compact nature of channelled waveguide lasers allows for the possibility of integration with on-chip devices on a single substrate, while being compatible with optical fibre systems.

Lasers doped with the rare-earth ion ytterbium have been favoured for many high-powered and pulsed laser applications because of its relatively simple energy transition levels between the upper manifold  $^2F_{5/2}$  and the lower manifold  $^2F_{7/2}$ , with the other energy levels in the ultra-violet wavelength region. The result of having a simple two-manifold energy structure is that undesired phenomena such as up-conversion, excited-state absorption and cross-relaxation processes are halted, allowing for high power lasers [7], [8]. It has the advantage that it can be pumped by a wide selection of solid-state lasers such as InGaAs laser diodes (typical spectral range between 900 - 1000 nm) due to its broad absorption band, ranging from 850 nm to above 1070 nm [9]. Other

advantages include long excited-state lifetimes, typically in the order of 500  $\mu\text{s}$  to 1.4 ms [8] giving rise to longer storage of energy, and a low quantum defect, the energy difference between the pump and laser photons, because of the close pump and lasing wavelength allowing for highly efficient lasers [10].

A powerful fabrication platform for creating devices on single substrates is based complementary metal-oxide semiconductor (CMOS) technology. Compatibility with this platform is an important feature for future integrated photonic devices because the large investment worldwide in microelectronics has created an avenue for mass-market, low-cost photonic systems. This fabrication technology is mostly used in the research field of silicon photonics but recent demonstrations have shown dielectric and silicon materials being combined to create integrated optical circuits to exploit both linear and non-linear optical properties of dielectric films for many different applications [11], [12], ranging from frequency comb generation [13] to waveguide lasers [14] and is an attractive method of device creation.

## 1.2 Project aims

This thesis is to explore the potential of Yb-doped tantalum pentoxide waveguides on silicon substrates for waveguide laser applications. The objectives of this work can be summarised to:

- Design and optimisation of waveguides for high intensity, circular mode profiles and the fabrication of single mode waveguides.
- Investigation of the spectroscopic properties of Yb:Ta<sub>2</sub>O<sub>5</sub> as laser host material.
- Demonstration of lasing near 1  $\mu\text{m}$  wavelength in Ta<sub>2</sub>O<sub>5</sub> on a silicon substrate.
- Numerical feasibility study of potential Kerr elements for future mode-locking.

## 1.3 Material selection

Ta<sub>2</sub>O<sub>5</sub> is a promising material for mass-producible, multifunctional, integrated photonic circuits on silicon, exhibiting excellent electrical, mechanical and thermal properties and good compatibility with complementary-metal-oxide-semiconductor (CMOS) technologies [15]. Its high refractive index ( $n \approx 2.124$  at  $\lambda \approx 980$  nm) [16], allows high index contrast between the waveguide core and silica cladding, providing for low-loss, tight bend radii thereby enabling the development of compact photonic circuits due to the strong confinement of the optical modes, and offering the potential for 2-D photonic crystal operation. Ta<sub>2</sub>O<sub>5</sub> rib waveguide losses of  $\approx 0.2$  dB/cm have been obtained at a wavelength of 1.07  $\mu\text{m}$  [17] and Ta<sub>2</sub>O<sub>5</sub> is an excellent host for rare-earth ions, as waveguide lasers were demonstrated with neodymium [17] and erbium [14], and also provides a large third-order nonlinearity ( $n_2 \approx 7.25 \times 10^{-19}$  m<sup>2</sup>/W at  $\lambda \approx 980$  nm) [18] for all-optical processing. Ta<sub>2</sub>O<sub>5</sub> offers high transparency and low two-photon absorption in the NIR compared with silicon, due to the band-gap being greater than 3.8 eV for Ta<sub>2</sub>O<sub>5</sub>, compared with 1.12 eV for silicon,

corresponding to absorption band-edges at below  $\lambda \approx 330$  nm for Ta<sub>2</sub>O<sub>5</sub> compared with  $\lambda \approx 1100$  nm for silicon. Also it features excellent rare-earth compatibility compared with silicon and silicon nitride [19], and high index-contrast and large third-order nonlinearity compared with aluminium oxide ( $n \approx 1.726$ ;  $n_2 \approx 0.31 \times 10^{-19}$  m<sup>2</sup>/W at  $\lambda \approx 1064$  nm [20]) rendering it of particular interest for the realization of mode-locked lasers. Ta<sub>2</sub>O<sub>5</sub> has also been used in biological applications with integrated rib waveguides used to optically sort and guide red blood cells with input powers of up to 1.8 W [21], illustrating further diversity of the material's capabilities.

## 1.4 Achievements and synopsis of the thesis

This thesis documents the development of ytterbium doped tantalum pentoxide as a new active medium for integrated optical devices, demonstrating for the first time a waveguide laser in this material system. The achievements of the thesis can be summarised below

- Establishment of a set of parameters for designing Ta<sub>2</sub>O<sub>5</sub> rib waveguide channels for yb-doped lasers, allowing the tailoring of the mode intensity profiles of the propagating fundamental mode. These parameters include the rib width, height and etch depth.
- In addition, a study was performed to investigate the feasibility of an integrated planar Kerr lens as modelocking element for pulsed laser applications, utilizing the third-order nonlinearity of Ta<sub>2</sub>O<sub>5</sub>. From the study possible dimensional parameters for future waveguide were established and also the loss modulation achievable was estimated.
- A comprehensive investigation of the spectroscopic properties of Ta<sub>2</sub>O<sub>5</sub> doped with ytterbium ions was realised for the first time. Important parameters such as the absorption and emission cross-sections, size of the fluorescence bandwidth and excited-state lifetime were measured to demonstrate the possibility of laser action.
- An Yb:Ta<sub>2</sub>O<sub>5</sub> waveguide laser was realised for the first time in this material system with a cavity formed from a combination of high-reflector mirrors, output couplers and bare end-facets. Laser performance characterisation was carried out by measuring the output power with respect to input pump power, as well as investigating the lasing spectrum produced by the waveguide laser.

Chapter 1 summarises the thesis and also includes a brief literature review looking at the origin of waveguide lasers and the recent development of ytterbium doped waveguide lasers.

Chapter 2 presents the basic theory and operation of waveguides and introduces the theoretical methods used for analysing and designing of rib waveguides. Simulations, using finite element analysis software, were carried out to investigate the effect that the dimensions of a symmetrical Ta<sub>2</sub>O<sub>5</sub> rib with silica over- and under-cladding has on the shape and size of a propagating

fundamental mode intensity profile. The aim was to calculate a set of parameters for the design of compact channel waveguides. The chapter ends with simulations of integrated Kerr lens elements in Ta<sub>2</sub>O<sub>5</sub>, investigating the feasibility using a planar Kerr lens element as a passive loss modulator, by modelling how the structure's dimensions and input intensity of the laser beam affects the loss of the Kerr lens device.

Chapter 3 describes the fabrication process used for the manufacturing of symmetrical Yb-doped Ta<sub>2</sub>O<sub>5</sub> rib waveguides on silicon with silica over- and under-cladding. The structuring of the rib waveguides was accomplished using a combination of photolithography and dry etching to create shallow rib waveguides. Also in this chapter the measurement of the mode intensities of the propagating waves in the rib waveguides are presented in chapter 2.

Chapter 4 presents the work carried out to discover the spectroscopic properties of the fabricated Yb-doped rib waveguides described in chapter 3. The absorption and fluorescence emission spectra were measured leading to determination of the transition cross-sections of the material. Finally the excited-state lifetime was measured using a mechanically chopped pump beam.

Chapter 5 reports laser action in Yb:Ta<sub>2</sub>O<sub>5</sub> rib waveguides. The chapter begins with a brief description of the basic principles of operation for ytterbium doped lasers. The experimental procedure for characterising the input pump beam for launch efficiency estimations and the lasing behaviour is described. The waveguide's lasing threshold and slope efficiencies are established through experimental measurements of the lasing output power with respect to the absorbed pump power, with the spectrum of Y:Ta<sub>2</sub>O<sub>5</sub> for different width waveguide measured.

The final chapter concludes this thesis with some remarks summarizing the work and a discussion of possible advancements and further work generated as a result of this project.

## 1.5 Review of ytterbium doped waveguide lasers

### 1.5.1 Rare-earth doped waveguide lasers

The earliest waveguide laser was demonstrated in 1961 by Snitzer [22] with a neodymium doped barium crown glass in a cylindrical waveguide core arrangement to achieve lasing at a wavelength of 1.06  $\mu\text{m}$ . After this early fibre laser action was demonstrated came the natural evolution of the development of laser systems utilizing planar and channel optical waveguide structures. This was an important step in the development of laser systems as many advantages beneficial for lasing are offered by waveguides in a channel or planar format [6], as introduced earlier. The most important of these is tailoring of the waveguide geometry for better mode overlap between the pump and laser beam propagating in the waveguide reducing laser threshold [1], having a high degree of thermal immunity as planar structures have a beneficial temperature dissipation geometry [6], and can be integrated for on-chip devices.

The first appearance of an optically pumped thin-film dye laser on a planar dielectric was by Kogelnik at Bell Telephone Laboratories [23] which occurred in 1971, a decade after the optical maser was first demonstrated by Snitzer [22]. Here a cavity was created using a distributed feedback (DFS) system in rhodamine G dyed gelatine on a glass substrate, with lasing reported at wavelength of 630 nm while pumped with a UV source. Soon after laser action with a rectangular channel waveguide filled with an organic liquid dye was reported [24]. Pumped by a frequency doubled neodymium doped YAG giant pulsed laser, the optical guided modes travelled within the liquid dye (rhodamine B dye dissolved in benzyl alcohol), with lasing generated with a cavity created from uncoated glass end-facets. A shift from dye waveguide materials to rare-earth doped waveguide media was demonstrated in 1972 with the first reported single crystal thin-film laser created with holmium doped aluminium garnet [25]. They reported coherent emission at 2.1  $\mu\text{m}$  in a laser structure consisting of a single crystal epitaxial grown garnet film.

Improvement of the output power that laser diodes could achieve reached a critical level towards the end of 1980s and became attractive for the optical pumping of active waveguide devices and laser materials [26]. This led to the first glass thin-film laser reported in 1989 by Hibino et al. [27]. A neodymium-doped silica thin-film was deposited on to a silicon substrate by flame hydrolysis deposition (FHD), with optical channels created using reactive ion etching (RIE). An optical cavity was created from dielectric mirrors deposited on the end-facet with lasing achieved using an 800 nm pump source, producing signal at a wavelength of 1.0515  $\mu\text{m}$  with a threshold of 150 mW. This achievement was only possible with the development of fabrication processes offering low loss glass thin-films, reducing laser threshold and increasing the slope efficiency. This achievement renewed the interest in planar and channel waveguides for laser devices.

Since the first demonstrations of laser action in planar waveguides in the early seventies, there has been a growing development of material processing resulting in a wide range of active thin-film materials for laser applications. This was driven by progress in waveguide fabrication technologies such as ion-exchange glass waveguides [28], growing of bulk crystals [29], liquid phase epitaxy (LPE) for semiconductor crystal layer growth [30], and chemical and physical deposition of optical thin-films, resulting in a wide range of active thin-film materials [31].

With the research in waveguide lasers expanding into many different approaches as a result of different fabrication techniques, more doping ions and host materials were investigated. One host material investigated extensively was yttrium aluminium garnet (YAG), a crystal first shown as a laser host in a rod configuration in 1964 [32], which is particularly favoured for high powered and pulsed lasers [9]. Planar waveguide lasers have been demonstrated by epitaxially grown YAG doped with neodymium (Nd) ions. This material system was able to produce a laser operation with a slope efficiency  $\approx 40\%$  with a low laser threshold of  $\approx 0.7$  mW, indicating very low propagation losses ( $\leq 0.05$  dB/cm) [33]. More recently Nd:YAG laser written waveguides using a femtosecond

laser were demonstrated by Siebenmorgan et al. [34]. Pumped at 808 nm, laser operation was achieved at a wavelength of 1064 nm with a slope efficiency of 23%. This was improved further by the same group leading to a Nd:YAG waveguide producing lasing output power of 1.3 W at 2.25 W launched pump power [35]. The direct femtosecond laser writing technology is a relatively new waveguide defining process which bypasses the need for photolithography step. It is a single step method, which can produce three-dimensional low loss waveguides caused by a refractive index change independent of the dopant ion within the thin-film host material [36].

In recent years optical glass and amorphous waveguides lasers in the near- and short-wavelength infrared regions have been developed. Erbium (Er) doped distributed feedback laser was demonstrated with a laser cavity consisting of a silicon nitride waveguide defined by wafer-scale immersion lithography and an aluminium oxide ( $\text{Al}_2\text{O}_3$ ) doped film deposited [37]. Pumped with a 1480 nm fibre laser, lasing was presented with a wavelength of 1563 nm with a threshold of 31 mW and slope efficiency of 7%. Er-doped tellurium oxide ( $\text{TeO}_2$ ) planar waveguide laser fabricated using RF magnetron sputtering using a co-sputtering system with tellurium and erbium targets demonstrated for the first time lasing, with laser emission at 1550 when pumped at 980 nm [38]. Amorphous thin-films in  $\text{Ta}_2\text{O}_5$  have demonstrated lasing, doped with neodymium [17] and Er [14] rare-earth ions which were sputtered onto silicon substrates, with rib waveguides structured using a combination of photolithography and ion beam milling (IBM). Nd: $\text{Ta}_2\text{O}_5$  obtained lasing at both 1066 nm and 1375 nm with the former having a slope efficiency of 21% but with a low threshold of 2.7 mW, and Er: $\text{Ta}_2\text{O}_5$  obtained lasing between 1556 and 1560 nm with threshold of 14 mW and low slope efficiency of 0.3%. With high refractive index  $n \approx 2.12$  at the pump wavelengths of laser diodes, this material system shows promise for compact integrated optical circuits in communication and medical applications.

For medical applications, free space optical communication, sensing and spectroscopy [39], the mid-IR region is an important section of optical radiation. Rare-earth ion such as thulium (Tm) are used as a dopant for host materials to produce laser operation at wavelengths  $\approx 2 \mu\text{m}$ . Compact monolithic laser cavities were formed from fluorogermanate glass waveguides doped with Tm demonstrating lasing at a wavelength of 1.9  $\mu\text{m}$  [40]. Pumped using a Ti:sapphire laser tuned to 791 nm, waveguides created using ultrafast laser inscribing (ULI) lasing was achieved with a slope efficiency of 6% and a maximum output power of 32 mW. In the same year a Tm:ZBLAN waveguide laser was demonstrated lasing at a wavelength of 1.88  $\mu\text{m}$  with a much higher slope efficiency of 50% [41]. The waveguide structures were fabricated using a femtosecond laser to directly write complex cylinder waveguides within the thin film. Mirrors butted against the end-facets created an optical cavity with maximum achievable output power, limited by the pump power of 48 mW. Longer wavelength emission at 2.9  $\mu\text{m}$  has only recently been demonstrated for the first time in a waveguide from a ZBLAN glass host doped with holmium (Ho). ULI was used to

fabricate a circular waveguide buried within bulk glass with losses  $\leq 0.4$  dB/cm leading to lasing with a threshold of 28 mW and slope efficiency of 20% [42]. Zinc selenide (ZnSe) doped with chromium (Cr) transition metal, demonstrated tunable waveguide lasers for lasing emission ranging between 2077 – 2770 nm with maximum output power of 120 mW at 2446 nm [43], the waveguides fabricated using ULI to create low loss waveguides (0.7 dB/cm) buried within the polycrystalline bulk material. More recently by the same group, ULI waveguides in ZeSe doped with iron demonstrated lasing at 4122 nm, with the optimum waveguide having a slope efficiency of 11% with a threshold of 210 mW while pumped at 808 nm [44].

### 1.5.2 Ytterbium doped waveguide lasers

Lasers based on rare-earth doped solid-state crystals and glasses operating in the spectral region of 1  $\mu$ m have become a reliable source for many different applications as a result of the possibility of highly efficient diode pumped laser systems. During the early years of laser diodes being used for optical pumping, the potential of the trivalent ytterbium ion was recognized as a dopant for laser applications [45], in comparison with Nd ion as Yb possesses a longer energy-storage lifetime, a smaller quantum defect and pumped optically by robust InGaAs laser diode in operating in the spectral range between 900 and 1000 nm [9]. Other attributes that make ytterbium an interesting rare-earth ion is its simple two-manifold structure where undesired phenomena such as up-conversion, excited-state absorption and cross-relaxation processes that can be detrimental to lasing operation do not occur. But operation in its quasi-three-level scheme poses challenges with design and implementation as thermal population at the lower laser levels is present [46].

Ytterbium combined with the advantages of waveguide lasers has created much interest in research for compact, integrated high power and modelocked lasers. Early demonstration of Yb-doped waveguide lasers were shown in YAG planar waveguides. Ion-implanted planar waveguides 10 mm long where pumped at a room temperature with a wavelength of 941 nm and exhibited laser operation at a 1030 nm with a threshold of 30 mW and low slope efficiency of 19% [47]. This was improved with Yb:YAG grown using LPE to produce lower loss thin films, producing laser action at wavelengths of 1030 nm and 1050 nm with the latter giving results of high slope efficiency of 77% with threshold of 43 mW [48]. In the same year laser action was demonstrated in Yb-indiffused lithium niobate (LiNbO<sub>3</sub>) channel waveguides with mirrors butted against the end-facets [49]. From a high reflector mirror and 7% output coupler configuration, lasing at 1008 nm occurred with slope efficiency of 16% and threshold of 85 mW. The performance of this laser system was limited by high waveguide losses and with photorefractive damage causing laser operation to last for only  $\approx 1$  minute. The problem with waveguide damage caused by high optical power for an ytterbium doped waveguide was partially solved by Fujimura nearly a decade later by using annealed proton-exchanged by diffusion of the Yb ions [50], while also allowing access to electro-optic tensor/non-linear optical tensor  $r_{33}/d_{33}$  of LiNbO<sub>3</sub>, which has not been possible with diffused

fabrication techniques [51]. Laser performance suffered for stability as the maximum output power which could be reached was 1.2  $\mu$ W for a threshold of 40 mW giving an extremely low efficiency of  $3 \times 10^{-5}$ . This meant that even with the fabricated  $\text{LiNbO}_3$  waveguides keeping its electro-optical, acousto-optical and non-linear optical effects the integration of such a low efficient waveguide laser into photonic devices is impractical.

YAG: Recent development in YAG has seen diode pumped waveguides fabricated using femtosecond writing, with light guided between a pair of micro-tracks. Pumped at 941 nm, lasing at 1063 nm with a slope efficiency of 75%, achieved for high output power  $\approx 0.8$  W. A planar waveguide laser was also demonstrated in Yb:YAG with double-side pump arrangement at 940 nm producing visible emission between 475 nm and 550 nm due a cooperative luminescence process [52].

Tungstates: Another promising group of single crystal host media are monoclinic potassium double tungstates, mostly used as gain media for high power Yb-doped waveguide lasers [53], partly due to their large emission and absorption cross-sections but also their ability to be doped heavily [54].

Host	$\text{Al}_2\text{O}_3$ [55]	ZBLAN [56]	Silicate glass [56]	$\text{LiYF}_4$ [57]	$\text{Y}_2\text{O}_3$ [58]	YAG [52]	Bismuthate glass [59]	$\text{KY}(\text{WO}_4)_2$ [60]	$\text{YVO}_4$ [61]
Refractive index	1.65	1.51	1.53	1.44	1.91	1.81	2.03	$\approx 2$	1.957
Fabrication method	Reactive co-sputtering	Fs-laser direct writing	Fs-laser direct writing	Liquid-phase epitaxy	Pulsed laser deposition	Adhesive-free contact bonding	Ultrafast laser inscription	Liquid-phase epitaxy	Czochralski technique
Ytterbium ion density, $N$ , ( $\times 10^{20} \text{ cm}^{-3}$ )	5.8	2.5 mol%	8 wt. %	4.6	1.85 at. %	2 wt. %	1.6	1.2 - 2.4 at. %	2
Pump wavelength, $\lambda_p$ , (nm)	976	974	974	960	965	940	975	980	984
Laser wavelength, $\lambda_l$ , (nm)	1021.2	1020-1045	1029	994	1030	1030	1030-1035	1025	1020
Slope efficiency, $\eta_{sl}$ , (%)	67	84	25	76	20	75	79	67.4	49
Laser threshold, $P_{th}$ , (mW)	10	31	44	400*	$\approx 2.5$ W*	$\approx 125$ *	35	80	650
Year published	2011	2013	2013	2013	2014	2011	2012	2006	2004

Table 1.1 Comparison of the material and laser properties of some recently realised Yb-doped waveguide lasers. \*These cross-sections have been extracted from diagrams in the literature as accurately as possible

Tungstates such as Yb-doped  $\text{KY}(\text{WO}_4)_2$  are a relatively new laser material, with laser operation demonstrated near 1  $\mu$ m reported with a maximum output power of 290 mW in the fundamental mode with slope efficiency above 80% in 2006 [60] and output power of 148 mW and slope efficiency of 62% in a monolithic micro-cavity [62]. The thin-films of the doped crystal were grown using LPE with undoped KYG under- and over-cladding. Diode pumped channel waveguides have also been fabricated using ULI and for laser operation at 1023 nm [63], with the maximum output achieved with this waveguide type was 18.6 mW with a threshold of 100 mW.

Micro-structured waveguides are also shown in LPE grown potassium double tungstates, with waveguides realised using a combination of photolithography and argon ion beam milling [64]. They were able to achieve high lasing powers of 650 mW and slope efficiency of 76% by making the output coupler larger, therefore reducing the amount of light fed backing into channel reducing the effect of the large intra-cavity propagation loss typical of ion beam milled waveguides. Other Yb-doped gain material has also recently been demonstrated with  $\text{LiYF}_4$  [57],  $\text{Y}_2\text{O}_3$  [58] and  $\text{YVO}_4$  [61] with a comparison of material and laser properties of these recently realised Yb-doped waveguide lasers shown in table 1.1.

*Phosphate glass:* Planar monolithic gain media in glass thin-films has been used to create waveguide lasers in Yb-glass such as phosphate ( $\text{P}_2\text{O}_5$ ) glass. A monolithic Yd-doped waveguide laser with a Bragg grating acting as a distributed-feedback (DFB) resonator was created using femtosecond-laser direct-writing in a single step [65]. Output powers up to 102 mW at wavelength of 1033 nm were reported, improving upon previous cavity designs for erbium- and ytterbium-doped phosphate glass host where lasing only was achieved with a high threshold of 639 mW lasing with a small maximum output power  $\approx 0.37$  mW, limited by pump power [66]. Yb-doped waveguides were also fabricated with ion-exchange with lasing occurring near the typical range of 1020 nm with a high slope efficiency of 67% [67]. Ion exchange was also used in the fabrication for silicate based waveguide lasers doped with a high Yb concentration of 12 wt.% [68]. This waveguide operated at a wavelength between 1020-1030 nm under 910 nm pump regime with threshold of 50 mW and efficiency of 5%.

Ultrafast laser direct-written waveguides in other high refractive index ( $n \approx 2$ ) glasses such as ZBLAN and IOG10 (silicate) have also reported successful lasing [56]. The fabrication technique produced high refractive index contrast waveguide ( $\Delta n = 2.3 \times 10^{-2}$ ) allowing for better confinement of light, leading to a slope efficiency of 84% with maximum output power of 170 mW in Yb:ZBLAN and in Yb:IOG10 a slope efficiency of 25% with maximum output power of 72 mW.

*CMOS compatible amorphous films:* CMOS fabrication technologies have been utilized to create compact, integrated waveguide lasers on silicon substrates, such as systems based on  $\text{Al}_2\text{O}_3$  and also based on different resonator schemes for example a ring resonator [69], and distributed-Bragg-reflector [55]. The micro-resonator was designed for compact, monolithic devices with a small foot print by combined layers of high refractive index material of silicon nitrate ( $n = 2$ ) and Yb: $\text{Al}_2\text{O}_3$  ( $n = 1.65$ ) for 160  $\mu\text{m}$  diameter ring resonators with small bend radii buried in silica. It was reported to have lasing output power of  $> 100$   $\mu\text{W}$  and a low threshold of 0.7 mW and double ended slope efficiency of 8.4% and it shows promise with fabrication and design optimization of more efficiency lasers that can be integrated with other optical to electronics devices. The distributed-Bragg-reflector channel in Yb: $\text{Al}_2\text{O}_3$  was co-sputtered using metal targets with the channels created

using photolithography and reactive ion etching, creating highly efficient (67%), low threshold (47 mW) waveguide lasers.

Amorphous and glass media typically have much broader transitions with bandwidths of the order of tens of nano-meters than typical crystal media [70]–[73], which is important for application such as modelocked lasing where the pulse temporal width is governed by the gain bandwidth [74], [75]. An exception is Yb-doped tungstate materials, such as Yb:NaGd(WO<sub>4</sub>)<sub>2</sub> where a disordered single crystal structure can create large gain bandwidth [7], [76], however, the emission curve of the crystal is not smooth with several peaks appearing in the spectrum. This can lead to difficulty of generating very short pulses for modelocked laser applications as it would create multi-pulsing.

## 1.6 Conclusion

Yb-doped optical materials are a very active research subject of lasers emitting at wavelengths near 1  $\mu\text{m}$  in bulk, disk and fiber configurations. Their attractive properties include broad absorption near 0.98  $\mu\text{m}$  for optical pumping from low-cost semiconductor sources, long excited-state lifetime for energy storage, broadband gain for wide wavelength selection, tunability and modelocking, a low quantum defect for good power-handling ability and lack of excited-state absorption or significant concentration-quenching effects, for efficient operation. Large absorption and emission cross-sections in several materials such as bismuthate glasses [77] and double tungstate crystals [73], lead to compact devices with the potential for very high gain coefficients. Gain coefficients close to 1000 dB/cm have been measured for the latter, comparable with semiconductor devices [78]. Efficient, low threshold, operation of this quasi-three-level laser system is enhanced by incorporation in a waveguide configuration, due to the excellent pump/signal mode overlap and tight, diffraction-free, containment of the modes yielding high inversion at low pump powers. While planar waveguides have the disadvantage of higher loss coefficients when compared with optical fibres, this is of minor importance in the case of a high-gain system such as Yb<sup>3+</sup> (in contrast to Er<sup>3+</sup>) and the planar configuration has the further advantages of monolithic integration of mass-produced devices and of straightforward heat removal [79]. Waveguide materials and processes that are compatible with silicon processing are strongly favoured for low-cost mass-manufacture. Silicon waveguides themselves are unsuitable for handling wavelengths below 1.1  $\mu\text{m}$  and exhibit two-photon absorption at wavelengths below 2  $\mu\text{m}$ , limiting their utility for pulsed and high-power applications in this range. This has led to CMOS-compatible dielectric waveguide systems such as silicon nitride [12], aluminium oxide [80] and tantalum pentoxide [18] being explored. Lasing in Er-doped [81] and Yb-doped [55] alumina and Nd-doped [17] and Er-doped [14] tantalum pentoxide have been demonstrated.

The advantages that Ta<sub>2</sub>O<sub>5</sub> has over many yb-doped lasers developed is it is high index contrast CMOS compatible material system that can enable the possibility of fabricating complex and

exotic, integrated photonic circuits on silicon substrates. Coupled with its ability to host rare-earth ions and high non-linearity, this material can lead to mass-producible, low-cost planar devices with many interlocking photonic circuits for multi-functionality.

## 1.7 Bibliography

- [1] W. P. Risk, "Modeling of longitudinally pumped solid-state lasers exhibiting reabsorption losses," *J. Opt. Soc. Am. B*, vol. 5, no. 7, p. 1412, Jul. 1988.
- [2] A. C. Turner, C. Manolatou, B. S. Schmidt, M. Lipson, M. A. Foster, J. E. Sharping, and A. L. Gaeta, "Tailored anomalous group-velocity dispersion in silicon channel waveguides," *Opt. Express*, vol. 14, no. 10, p. 4357, 2006.
- [3] G. P. Agrawal, *Nonlinear fiber optics*, 5th Edit. Oxford: Academic Press, 2013.
- [4] L. F. Mollenauer, R. H. Stolen, and J. P. Gordon, "Experimental observation of picosecond pulse narrowing and solitons in optical fibers," *Phys. Rev. Lett.*, vol. 45, no. 13, pp. 1095–1098, Sep. 1980.
- [5] E. Lallier, "Rare-earth-doped glass and LiNbO<sub>3</sub> waveguide lasers and optical amplifiers," *Appl. Opt.*, vol. 31, no. 25, pp. 5276–5282, 1992.
- [6] J. I. Mackenzie, "Dielectric solid-state planar waveguide lasers: A review," *IEEE Journal on Selected Topics in Quantum Electronics*, vol. 13, no. 3, pp. 626–637, 2007.
- [7] C. Cascales, M. D. Serrano, F. Esteban-Betegón, C. Zaldo, R. Peters, K. Petermann, G. Huber, L. Ackermann, D. Rytz, C. Dupré, M. Rico, J. Liu, U. Griebner, and V. Petrov, "Structural, spectroscopic, and tunable laser properties of Yb<sup>3+</sup>-doped NaGd(WO<sub>4</sub>)<sub>2</sub>," *Phys. Rev. B*, vol. 74, no. 17, p. 174114, Nov. 2006.
- [8] M. J. Dignonnet, *Rare-earth-doped fiber lasers and amplifiers, revised and expanded*, 2nd edit. CRC Press, 2001.
- [9] W. F. Krupke, "Ytterbium solid-state lasers — the first decade," *IEEE J. Sel. Top. Quantum Electron.*, vol. 6, no. 6, pp. 1287–1296, 2000.
- [10] J. Petit, P. Goldner, and B. Viana, "Laser emission with low quantum defect in Yb:CaGdAlO<sub>4</sub>," *Opt. Lett.*, vol. 30, no. 11, p. 1345, Jun. 2005.
- [11] D. J. Moss, R. Morandotti, A. L. Gaeta, and M. Lipson, "New CMOS-compatible platforms based on silicon nitride and Hydex for nonlinear optics," *Nat. Photonics*, vol. 7, no. 8, pp. 597–607, Jul. 2013.
- [12] J. S. Levy, A. Gondarenko, M. A. Foster, A. C. Turner-Foster, A. L. Gaeta, and M. Lipson, "CMOS-compatible multiple-wavelength oscillator for on-chip optical interconnects," *Nat. Photonics*, vol. 4, no. 1, pp. 37–40, Jan. 2010.
- [13] F. Ferdous, H. Miao, D. E. Leaird, K. Srinivasan, J. Wang, L. Chen, L. T. Varghese, and A. M. Weiner, "Spectral line-by-line pulse shaping of on-chip microresonator frequency combs," *Nat. Photonics*, vol. 5, no. 12, pp. 770–776, Oct. 2011.

- 
- [14] A. Z. Subramani, C. J. Oton, D. P. Shepherd, and J. S. Wilkinson, "Erbium-doped waveguide laser in tantalum pentoxide," *IEEE Photonics Technol. Lett.*, vol. 22, no. 21, pp. 1571–1573, Nov. 2010.
- [15] C. Chaneliere, J. L. Autran, R. a. B. Devine, and B. Balland, "Tantalum pentoxide ( $\text{Ta}_2\text{O}_5$ ) thin films for advanced dielectric applications," *Mater. Sci. Eng. R Reports*, vol. 22, no. 6, pp. 269–322, 1998.
- [16] A. Subramanian, "Tantalum pentoxide waveguide amplifier and laser for planar lightwave circuits," Ph.D. Thesis, University of Southampton, U.K., 2011.
- [17] B. Unal, M. C. Netti, M. A. Hassan, P. J. Ayliffe, M. D. B. Charlton, F. Lahoz, N. M. B. Perney, D. P. Shepherd, Chao-Yi Tai, J. S. Wilkinson, and G. J. Parker, "Neodymium-doped tantalum pentoxide waveguide lasers," *IEEE J. Quantum Electron.*, vol. 41, no. 12, pp. 1565–1573, Dec. 2005.
- [18] C.-Y. Tai, J. Wilkinson, N. Perney, M. Netti, F. Cattaneo, C. Finlayson, and J. Baumberg, "Determination of nonlinear refractive index in a  $\text{Ta}_2\text{O}_5$  rib waveguide using self-phase modulation," *Opt. Express*, vol. 12, no. 21, pp. 5110–5116, 2004.
- [19] S. Fathpour, "Emerging heterogeneous integrated photonic platforms on silicon," *Nanophotonics*, vol. 4, no. 1, Jan. 2015.
- [20] D. N. Christodoulides, I. C. Khoo, G. J. Salamo, G. I. Stegeman, and E. W. Van Stryland, "Nonlinear refraction and absorption: mechanisms and magnitudes," *Adv. Opt. Photonics*, vol. 2, no. 1, p. 60, Mar. 2010.
- [21] B. S. Ahluwalia, O. G. Hellesø, A. Z. Subramanian, J. S. Wilkinson, J. Chen, and X. Chen, "Integrated platform based on high refractive index contrast waveguide for optical guiding and sorting," in *SPIE 7613, Complex Light and Optical Forces IV, 76130R*, 2010, p. 76130R–76130R–8.
- [22] E. Snitzer, "Optical maser action of  $\text{Nd}^{+3}$  in a barium crown glass," *Phys. Rev. Lett.*, vol. 7, no. 12, pp. 444–446, 1961.
- [23] H. Kogelnik, "Stimulated emission in a periodic structure," *Appl. Phys. Lett.*, vol. 18, no. 4, p. 152, 1971.
- [24] G. Zeidler, "Optical waveguide technique with organic dye lasers," *J. Appl. Phys.*, vol. 42, no. 2, p. 884, 1971.
- [25] J. P. Van der Ziel, W. A. Bonner, L. Kopf, and L. G. Van Uitert, "Coherent emission from  $\text{Ho}^{3+}$  ions in epitaxially grown thin aluminum garnet films," *Phys. Lett. A*, vol. 42, no. 1, pp. 105–106, Nov. 1972.
- [26] T. Y. Fan and R. L. Byer, "Diode laser-pumped solid-state lasers," *IEEE J. Quantum Electron.*, vol. 24, no. 6, pp. 895–912, Jun. 1988.
- [27] Y. Hibino, T. Kitagawa, M. Shimizu, F. Hanawa, and A. Sugita, "Neodymium-doped silica optical waveguide laser on silicon substrate," *IEEE Photonics Technol. Lett.*, vol. 1, no. 11, pp. 349–350, Nov. 1989.
- [28] R. V. Ramaswamy and R. Srivastava, "Ion-exchanged glass waveguides: a review," *J. Light. Technol.*, vol. 6, no. 6, pp. 984–1000, Jun. 1988.

- 
- [29] R. Burkhalter, I. Dohnke, and J. Hulliger, "Growing of bulk crystals and structuring waveguides of fluoride materials for laser applications," *Prog. Cryst. Growth Charact. Mater.*, vol. 42, no. 1–2, pp. 1–64, Jan. 2001.
- [30] B. Ferrand, B. Chambaz, and M. Couchaud, "Liquid phase epitaxy: A versatile technique for the development of miniature optical components in single crystal dielectric media," *Opt. Mater. (Amst)*, vol. 11, no. 2–3, pp. 101–114, Jan. 1999.
- [31] M. Jelínek, "Progress in optical waveguiding thin films," *Czechoslov. J. Phys.*, vol. 53, no. 5, pp. 365–377, 2003.
- [32] J. E. Geusic, H. M. Marcos, and L. G. Van Uitert, "Laser oscillations in Nd-doped yttrium aluminum, yttrium gallium and gadolinium garnets," *Appl. Phys. Lett.*, vol. 4, no. 10, p. 182, 1964.
- [33] I. Chartier, B. Ferrand, D. Pelenc, S. J. Field, D. C. Hanna, A. C. Large, D. P. Shepherd, and A. C. Tropper, "Growth and low-threshold laser oscillation of an epitaxially grown Nd:YAG waveguide," *Opt. Lett.*, vol. 17, no. 11, p. 810, Jun. 1992.
- [34] J. Siebenmorgen, K. Petermann, G. Huber, K. Rademaker, S. Nolte, and A. Tünnermann, "Femtosecond laser written stress-induced Nd:Y<sub>3</sub>Al<sub>5</sub>O<sub>12</sub> (Nd:YAG) channel waveguide laser," *Appl. Phys. B*, vol. 97, no. 2, pp. 251–255, Oct. 2009.
- [35] T. Calmano, J. Siebenmorgen, O. Hellmig, K. Petermann, and G. Huber, "Nd:YAG waveguide laser with 1.3 W output power, fabricated by direct femtosecond laser writing," *Appl. Phys. B*, vol. 100, no. 1, pp. 131–135, Jul. 2010.
- [36] C. Grivas, "Optically pumped planar waveguide lasers, Part I: Fundamentals and fabrication techniques," *Prog. Quantum Electron.*, vol. 35, no. 6, pp. 159–239, Nov. 2011.
- [37] E. S. Hosseini, Purnawirman, J. D. B. Bradley, J. Sun, G. Leake, T. N. Adam, D. D. Coolbaugh, and M. R. Watts, "CMOS-compatible 75 mW erbium-doped distributed feedback laser," *Opt. Lett.*, vol. 39, no. 11, p. 3106, Jun. 2014.
- [38] K. Vu, S. Farahani, and S. Madden, "980nm pumped erbium doped tellurium oxide planar rib waveguide laser and amplifier with gain in S, C and L band," *Opt. Express*, vol. 23, no. 2, p. 747, Jan. 2015.
- [39] K. Scholle, S. Lamrini, P. Koopmann, and P. Fuhrberg, "2  $\mu\text{m}$  Laser Sources and Their Possible Applications," in *Frontiers in Guided Wave Optics and Optoelectronics*, InTech, 2010.
- [40] F. Fusari, R. R. Thomson, G. Jose, F. M. Bain, A. A. Lagatsky, N. D. Psaila, A. K. Kar, A. Jha, W. Sibbett, and C. T. A. Brown, "Lasing action at around 1.9  $\mu\text{m}$  from an ultrafast laser inscribed Tm-doped glass waveguide," *Opt. Lett.*, vol. 36, no. 9, p. 1566, May 2011.
- [41] D. G. Lancaster, S. Gross, H. Ebendorff-Heidepriem, K. Kuan, T. M. Monro, M. Ams, A. Fuerbach, and M. J. Withford, "Fifty percent internal slope efficiency femtosecond direct-written Tm<sup>3+</sup>:ZBLAN waveguide laser," *Opt. Lett.*, vol. 36, no. 9, p. 1587, May 2011.
- [42] D. G. Lancaster, S. Gross, H. Ebendorff-Heidepriem, M. J. Withford, T. M. Monro, and S. D. Jackson, "Efficient 2.9  $\mu\text{m}$  fluorozirconate glass waveguide chip laser," *Opt. Lett.*, vol. 38, no. 14, p. 2588, Jul. 2013.

- 
- [43] J. R. Macdonald, S. J. Beecher, A. Lancaster, P. A. Berry, K. L. Schepler, and A. K. Kar, "Ultrabroad Mid-Infrared Tunable Cr:ZnSe Channel Waveguide Laser," *IEEE J. Sel. Top. Quantum Electron.*, vol. 21, no. 1, pp. 375–379, Jan. 2015.
- [44] A. Lancaster, G. Cook, S. A. McDaniel, J. Evans, P. A. Berry, J. D. Shephard, and A. K. Kar, "Mid-infrared laser emission from Fe:ZnSe cladding waveguides," *Appl. Phys. Lett.*, vol. 107, no. 3, p. 031108, Jul. 2015.
- [45] P. Lacovara, H. K. Choi, C. A. Wang, R. L. Aggarwal, and T. Y. Fan, "Room-temperature diode-pumped Yb:YAG laser," *Opt. Lett.*, vol. 16, no. 14, p. 1089, Jul. 1991.
- [46] W. Koechner, *Solid-state laser engineering*, vol. 1. New York, NY: Springer New York, 2006.
- [47] D. C. Hanna, J. K. Jones, A. C. Large, D. P. Shepherd, A. C. Tropper, P. J. Chandler, M. J. Rodman, P. D. Townsend, and L. Zhang, "Quasi-three level 1.03  $\mu\text{m}$  laser operation of a planar ion-implanted Yb:YAG waveguide," *Optics Communications*, vol. 99, no. 3–4, pp. 211–215, 1993.
- [48] D. Pelenc, B. Chambaz, I. Chartier, B. Ferrand, C. Wyon, D. Shepherd, D. Hanna, A. Large, and A. Tropper, "High slope efficiency and low threshold in a diode-pumped epitaxially grown Yb:YAG waveguide laser," *Opt. Commun.*, vol. 115, no. 5–6, pp. 491–497, Apr. 1995.
- [49] J. K. Jones, J. P. de Sandro, M. Hempstead, D. P. Shepherd, A. C. Large, A. C. Tropper, and J. S. Wilkinson, "Channel waveguide laser at 1  $\mu\text{m}$  in Yb-indiffused LiNbO<sub>3</sub>," *Optics Letters*, vol. 20, no. 13, p. 1477, 1995.
- [50] M. Fujimura, H. Tsuchimoto, and T. Suhara, "Yb-diffused LiNbO<sub>3</sub> annealed/proton-exchanged waveguide lasers," *IEEE Photonics Technol. Lett.*, vol. 17, no. 1, pp. 130–132, Jan. 2005.
- [51] J. Amin, J. A. Aust, D. L. Veasey, and N. A. Sanford, "Dual wavelength, 980 nm-pumped, Er/Yb-codoped waveguide laser in Ti:LiNbO<sub>3</sub>," *Electron. Lett.*, vol. 34, no. 5, p. 456, 1998.
- [52] I. J. Thomson, F. J. F. Monjardin, H. J. Baker, and D. R. Hall, "Efficient operation of a 400 W diode side-pumped Yb:YAG planar waveguide laser," *IEEE J. Quantum Electron.*, vol. 47, no. 10, pp. 1336–1345, Oct. 2011.
- [53] A. A. Kaminskii, "Laser crystals and ceramics: Recent advances," *Laser Photonics Rev.*, vol. 1, no. 2, pp. 93–177, May 2007.
- [54] A. A. Lagatsky, N. V. Kuleshov, and V. P. Mikhailov, "Diode-pumped CW lasing of Yb:KYW and Yb:KGW," *Opt. Commun.*, vol. 165, no. 1–3, pp. 71–75, Jul. 1999.
- [55] E. H. Bernhardt, H. A. G. M. van Wolferen, K. Wörhoff, R. M. de Ridder, and M. Pollnau, "Highly efficient, low-threshold monolithic distributed-Bragg-reflector channel waveguide laser in Al<sub>2</sub>O<sub>3</sub>:Yb<sup>3+</sup>," *Opt. Lett.*, vol. 36, no. 5, pp. 603–605, 2011.
- [56] G. Palmer, S. Gross, A. Fuerbach, D. G. Lancaster, and M. J. Withford, "High slope efficiency and high refractive index change in direct-written Yb-doped waveguide lasers with depressed claddings," *Opt. Express*, vol. 21, no. 14, p. 17413, Jul. 2013.

- 
- [57] W. Bolaños, F. Starecki, A. Braud, J.-L. Doualan, R. Moncorgé, and P. Camy, “2.8 W end-pumped  $\text{Yb}^{3+}:\text{LiYF}_4$  waveguide laser,” *Opt. Lett.*, vol. 38, no. 24, pp. 5377–80, 2013.
- [58] S. J. Beecher, T. L. Parsonage, J. I. Mackenzie, K. A. Sloyan, J. A. Grant-Jacob, and R. W. Eason, “Diode-end-pumped 1.2 W  $\text{Yb}:\text{Y}_2\text{O}_3$  planar waveguide laser,” *Opt. Express*, vol. 22, no. 18, p. 22056, Sep. 2014.
- [59] R. Mary, S. J. Beecher, G. Brown, R. R. Thomson, D. Jaque, S. Ohara, and A. K. Kar, “Compact, highly efficient ytterbium doped bismuthate glass waveguide laser,” *Optics Letters*, vol. 37, no. 10, p. 1691, 2012.
- [60] Y. E. Romanyuk, C. N. Borca, M. Pollnau, S. Rivier, V. Petrov, and U. Griebner, “Yb-doped  $\text{KY}(\text{WO}_4)_2$  planar waveguide laser,” *Opt. Lett.*, vol. 31, no. 1, p. 53, 2006.
- [61] V. E. Kisel, A. E. Troshin, N. A. Tolstik, V. G. Shcherbitsky, N. V. Kuleshov, V. N. Matrosova, T. A. Matrosova, and M. I. Kupchenko, “Spectroscopy and continuous-wave diode-pumped laser action of  $\text{Yb}^{3+}:\text{YVO}_4$ ,” *Opt. Lett.*, vol. 29, no. 21, p. 2491, 2004.
- [62] F. M. Bain, A. A. Lagatsky, S. V. Kurilchick, V. E. Kisel, S. A. Guretsky, A. M. Luginets, N. A. Kalanda, I. M. Kolesova, N. V. Kuleshov, W. Sibbett, and C. T. A. Brown, “Continuous-wave and Q-switched operation of a compact, diode-pumped  $\text{Yb}^{3+}:\text{KY}(\text{WO}_4)_2$  planar waveguide laser,” *Opt. Express*, vol. 17, no. 3, p. 1666, Feb. 2009.
- [63] F. M. Bain, A. A. Lagatsky, R. R. Thomson, N. D. Psaila, N. V. Kuleshov, A. K. Kar, W. Sibbett, and C. T. A. Brown, “Ultrafast laser inscribed  $\text{Yb}:\text{KGd}(\text{WO}_4)_2$  and  $\text{Yb}:\text{KY}(\text{WO}_4)_2$  channel waveguide lasers,” *Opt. Express*, vol. 17, no. 25, pp. 22417–22422, 2009.
- [64] D. Geskus, E. H. Bernhardt, K. van Dalen, S. Aravazhi, and M. Pollnau, “Highly efficient  $\text{Yb}^{3+}$ -doped channel waveguide laser at 981 nm,” *Opt. Express*, vol. 21, no. 11, p. 13773, Jun. 2013.
- [65] M. Ams, P. Dekker, G. D. Marshall, and M. J. Withford, “Monolithic 100 mW Yb waveguide laser fabricated using the femtosecond-laser direct-write technique,” *Opt. Lett.*, vol. 34, no. 3, pp. 247–249, 2009.
- [66] G. D. Marshall, P. Dekker, M. Ams, J. A. Piper, and M. J. Withford, “Directly written monolithic waveguide laser incorporating a distributed feedback waveguide-Bragg grating,” *Opt. Lett.*, vol. 33, no. 9, p. 956, May 2008.
- [67] D. L. Veasey, D. S. Funk, P. M. Peters, N. A. Sanford, G. E. Obarski, N. Fontaine, M. Young, A. P. Peskin, W.-C. Liu, S. N. Houde-Walter, and J. S. Hayden, “Yb/Er-codoped and Yb-doped waveguide lasers in phosphate glass,” *J. Non. Cryst. Solids*, vol. 263–264, pp. 369–381, Mar. 2000.
- [68] C. Florea and K. A. Winick, “Ytterbium-doped glass waveguide laser fabricated by ion exchange,” *J. Light. Technol.*, vol. 17, no. 9, pp. 1593–1601, 1999.
- [69] J. D. B. Bradley, E. S. Hosseini, Purnawirman, Z. Su, T. N. Adam, G. Leake, D. Coolbaugh, and M. R. Watts, “Monolithic erbium- and ytterbium-doped microring lasers on silicon chips,” *Opt. Express*, vol. 22, no. 10, p. 12226, May 2014.
- [70] C. Hönninger, R. Paschotta, M. Graf, F. Morier-Genoud, G. Zhang, M. Moser, S. Biswal, J. Nees, A. Braun, G. A. Mourou, I. Johannsen, A. Giesen, W. Seeber, and U. Keller,

- “Ultrafast ytterbium-doped bulk lasers and laser amplifiers,” *Appl. Phys. B Lasers Opt.*, vol. 69, no. 1, pp. 3–17, 1999.
- [71] J. Y. Allain, M. Monerie, and H. Poignant, “Ytterbium-doped fluoride fibre laser operating at 1.02  $\mu\text{m}$ ,” *Electron. Lett.*, vol. 28, no. 11, pp. 988 – 989, 1992.
- [72] P. Nandi and G. Jose, “Ytterbium-doped  $\text{P}_2\text{O}_5$  - $\text{TeO}_5$  glass for laser applications,” *IEEE J. Quantum Electron.*, vol. 13, no. 2, pp. 101–103, 2006.
- [73] N. V. Kuleshov, A. A. Lagatsky, A. V. Podlipensky, V. P. Mikhailov, and G. Huber, “Pulsed laser operation of Yb-doped  $\text{KY}(\text{WO}_4)_2$  and  $\text{KGd}(\text{WO}_4)_2$ ,” *Optics Letters*, vol. 22, no. 17, p. 1317, 1997.
- [74] V. Cautaerts, D. J. Richardson, R. Paschotta, and D. C. Hanna, “Stretched pulse  $\text{Yb}^{3+}$  silica fiber laser,” *Opt. Lett.*, vol. 22, no. 5, p. 316, Mar. 1997.
- [75] D. T. Walton, J. Nees, and G. Mourou, “Broad-bandwidth pulse amplification to the 10- $\mu\text{J}$  level in an ytterbium-doped germanosilicate fiber,” *Opt. Lett.*, vol. 21, no. 14, p. 1061, Jul. 1996.
- [76] M. Rico, J. Liu, U. Griebner, V. Petrov, M. Serrano, F. Esteban-Betegon, C. Cascales, and C. Zaldo, “Tunable laser operation of ytterbium in disordered single crystals of  $\text{Yb}:\text{NaGd}(\text{WO}_4)_2$ ,” *Opt. Express*, vol. 12, no. 22, pp. 5362–5367, 2004.
- [77] S. Ohara and Y. Kuroiwa, “Highly ytterbium-doped bismuth-oxide-based fiber,” *Opt. Express*, vol. 17, no. 16, pp. 14104–14108, 2009.
- [78] D. Geskus, S. Aravazhi, S. M. García-Blanco, and M. Pollnau, “Giant optical gain in a rare-earth-ion-doped microstructure,” *Adv. Mater.*, vol. 24, no. 10, pp. OP19–OP22, Mar. 2012.
- [79] J. I. Mackenzie, “Dielectric solid-state planar waveguide lasers: A review,” *IEEE J. Sel. Top. Quantum Electron.*, vol. 13, no. 3, pp. 626–637, 2007.
- [80] G. N. van den Hoven, R. J. I. M. Koper, A. Polman, C. van Dam, J. W. M. van Uffelen, and M. K. Smit, “Net optical gain at 1.53  $\mu\text{m}$  in Er-doped  $\text{Al}_2\text{O}_3$  waveguides on silicon,” *Appl. Phys. Lett.*, vol. 68, no. 14, p. 1886, 1996.
- [81] J. D. Bradley, R. Stoffer, L. Agazzi, F. Ay, K. Wörhoff, and M. Pollnau, “Integrated  $\text{Al}_2\text{O}_3:\text{Er}^{3+}$  ring lasers on silicon with wide wavelength selectivity,” *Opt. Lett.*, vol. 35, no. 1, p. 73, Jan. 2010.

# CHAPTER 2

## Planar Waveguides and Devices in Tantalum Pentoxide

### 2.1 Introduction

Waveguide laser designs combine a gain medium with a waveguide resonator structure and appear in many different forms such as doped fibres and solid-state waveguides and appeared as early as 1961 [1][2]. Planar solid-state laser waveguides are a group of lasers based on rare-earth or transition metal ion-doped crystals or non-crystalline structures. The advantages offered by waveguides in a planar or channel format include maintaining high optical intensity due to no beam divergence that leads to achieving high optical gain and gain efficiency when pumped at low power, can be pumped by laser diodes for lasing in regions where diode lasers do not exist or perform poorly [3], and have a high degree of thermal immunity [4]. The compact nature of channel waveguide lasers allows for the possibility of integration with on-chip devices on a single substrate, while being compatible with optical fibre systems. Therefore the design of channelled and planar waveguides is important as it can determine the performance of a laser. In this chapter, basic waveguide theory is presented which is used as the foundation for the design and development of channel waveguides for lasers. Parameters for understanding the various characteristics of planar waveguides such as effective index and supported number of modes are introduced, in addition to dimensional variables. Rib waveguides in  $\text{Ta}_2\text{O}_5$ , which are sandwiched between an  $\text{SiO}_2$  over- and under-cladding are simulated using finite element modelling software. The intention is to establish a set of parameters which will aid in the design of compact channel waveguides and devices specific to a set of requirements for an integrated optical circuit. Continuing the development of integrated channel waveguides and devices, using finite element modelling software an investigation into integrating a Kerr lens element into a planar architecture in  $\text{Ta}_2\text{O}_5$  medium was carried out. The aim is to investigate the feasibility of using a planar Kerr lens element as a passive loss modulator, that can be integrated with a CW waveguide laser to create a passive mode locked laser know as a Kerr lens mode locked (KLM) laser [5], by modelling how the structure's dimensions and input intensity of the laser beam effects the attenuation of the Kerr lens device.

## 2.2 Optical waveguide theory and operation

The basics of the electromagnetic theory of light that is introduced in this chapter is based on “An Introduction to Fiber Optics” by A. Ghatak and K. Thyagarajan [6], and begins with the analysis of electromagnetic radiation passing through a medium or free space in the form of magnetic field ( $\mathbf{H}(r, t)$ ) and electric field ( $\mathbf{E}(r, t)$ ). The electric and magnetic fields are a set of perpendicular waves which collectively form an electromagnetic wave, where the magnitude depends on both time ( $t$ ) and position ( $r$ ). Maxwell’s equations describe the relationship between the electric and magnetic fields through a set of six defining equations considering the charge density  $\rho$ , electric and magnetic flux density,  $\mathbf{D}$  and  $\mathbf{B}$ , polarization density  $\mathbf{P}$  and the current density  $\mathbf{J}$  of the medium [7].

Maxwell’s equations (with the units and numerical values of the equations given in table 2.1) are

$$\nabla \cdot \mathbf{D} = \rho \quad (2.1)$$

$$\nabla \cdot \mathbf{B} = 0 \quad (2.2)$$

$$\nabla \times \mathbf{E} = -\frac{\delta \mathbf{B}}{\delta t} \quad (2.3)$$

$$\nabla \times \mathbf{H} = \mathbf{J} + \frac{\delta \mathbf{D}}{\delta t} \quad (2.4)$$

where  $\mathbf{D}$  and  $\mathbf{B}$  relationships are

$$\mathbf{D} = \varepsilon_0 \mathbf{E} + \mathbf{P} \quad (2.5)$$

$$\mathbf{B} = \mu_0 (\mathbf{H} + \mathbf{M}) \quad (2.6)$$

Symbol	Name	Units or Numerical Value
$\rho$	Charge density	$\text{Cm}^{-3}$
$\varepsilon$	Permittivity of material	$\text{Fm}^{-1}$
$\varepsilon_0$	Permittivity of free space	$8.85 \times 10^{-12} \text{ Fm}^{-1}$
$\mu_0$	Permeability of free space	$4\pi \times 10^{-7} \text{ Hm}^{-1}$
$\mathbf{E}$	Electric field	$\text{Vm}^{-1}$
$\mathbf{D}$	Electric flux density	$\text{Cm}^{-2}$
$\mathbf{H}$	Magnetic field	$\text{Am}^{-1}$
$\mathbf{B}$	Magnetic flux density	T (or $\text{V}\cdot\text{sm}^{-2}$ )
$\mathbf{P}$	Polarization density	$\text{Cm}^{-2}$
$\mathbf{M}$	Magnetization density	$\text{Am}^{-1}$
$\mathbf{J}$	Current density	$\text{Am}^{-2}$

Table 2.1 Units and numerical values of Maxwells equations

For a medium that is source-free ( $\rho = 0$  and  $\mathbf{J} = 0$ ), non-conductive and non-magnetic, isotropic and linear the Maxwell equations can be simplified into terms of the magnetic and electric field components only

$$\nabla \cdot \mathbf{E} = 0 \quad (2.7)$$

$$\nabla \cdot \mathbf{H} = 0 \quad (2.8)$$

$$\nabla \times \mathbf{E} = -\mu_0 \frac{\delta \mathbf{H}}{\delta t} \quad (2.9)$$

$$\nabla \times \mathbf{H} = \varepsilon \frac{\delta \mathbf{E}}{\delta t} \quad (2.10)$$

where the refractive index of the medium can be described by

$$n^2 = \frac{\varepsilon}{\varepsilon_0} \quad (2.11)$$

For a planar waveguide configuration, as shown in figure 2.1, a waveguiding planar film (refractive index  $n_1$ ) is sandwiched between two layers of lower refractive indices. As a result light is guided because of total internal reflection.

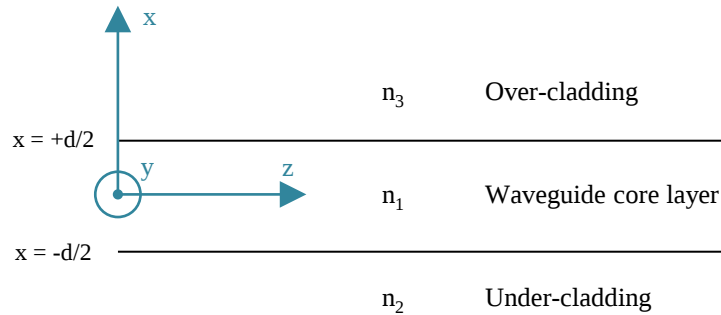


Figure 2.1 Optical waveguide side 2D schematic illustrating the over-cladding, waveguide core and under-cladding typical for planar structures.

Assuming the electric and magnetic fields are guiding along the  $z$  direction, they can be expressed as

$$\mathbf{E}(x, y, z, t) = \mathbf{E}(x, y)e^{j(\omega t - \beta z)} \quad (2.12)$$

$$\mathbf{H}(x, y, z, t) = \mathbf{H}(x, y)e^{j(\omega t - \beta z)} \quad (2.13)$$

Substituting the expressions (2.12) and (2.13) for the electric and magnetic fields into equations (2.9) and (2.10), taking the their  $x$ ,  $y$  and  $z$  components results in

$$i\beta \mathbf{E}_y = -i\omega\mu_0 \mathbf{H}_x \quad (2.14)$$

$$\frac{\delta \mathbf{E}_y}{\delta x} = -i\omega\mu_0 \mathbf{H}_z \quad (2.15)$$

$$-i\beta \mathbf{H}_x - \frac{\delta \mathbf{H}_z}{\delta x} = i\omega\epsilon_0 n^2(x) \mathbf{E}_y \quad (2.16)$$

$$i\beta \mathbf{H}_y = i\omega\epsilon_0 n^2(x) \mathbf{E}_x \quad (2.17)$$

$$\frac{\delta \mathbf{H}_y}{\delta x} = i\omega\epsilon_0 n^2(x) \mathbf{E}_z \quad (2.18)$$

$$-i\beta \mathbf{E}_x - \frac{\delta \mathbf{E}_z}{\delta x} = i\omega\mu_0 \mathbf{H}_y \quad (2.19)$$

The first three equations (2.14) - (2.16) are known as the transverse electric modes (TE) as the electric field has only a transverse  $\mathbf{E}_y$  component. The last three equations (2.17) - (2.19) are expressing the modes known as the transverse magnetic (TM) that have solutions containing only the  $\mathbf{H}_y$  component [6].

From Maxwell's equations we can begin to describe the modal analysis of a simple symmetric step index planar waveguide (figure 2.1), considering first the TE modes

$$\frac{d^2 \mathbf{E}_y}{dx^2} + [k_0^2 n^2(x) - \beta^2] \mathbf{E}_y = 0 \quad (2.20)$$

Where  $k_0 = \omega(\epsilon_0\mu_0)^{\frac{1}{2}} = \omega/c$  is the free space wavenumber and  $c = (\epsilon_0\mu_0)^{-\frac{1}{2}}$  is the speed of light in free space. Now assuming that there is an index profile like in figure 2.1

$$n(x) = \begin{cases} n_1; & |x| < \frac{d}{2} \\ n_2; & |x| > \frac{d}{2} \end{cases} \quad (2.21)$$

Solving equation (2.20) with the above results, the electromagnetic boundary condition must be continuous at  $x \pm d/2$  as a result of  $\mathbf{E}_y$  and  $d\mathbf{E}_y/dx$  leading to

$$\begin{aligned} \frac{d^2 \mathbf{E}_y}{dx^2} + k^2 \mathbf{E}_y &= 0; & |x| < \frac{d}{2} & \text{ waveguide layer} \\ \frac{d^2 \mathbf{E}_y}{dx^2} - \alpha^2 \mathbf{E}_y &= 0; & |x| > \frac{d}{2} & \text{ cladding layer} \end{aligned} \quad (2.22)$$

$$\begin{aligned} \mathbf{E}_y(x) &= A \cos kx + B \sin kx & |x| < d/2 & \text{ waveguide layer} \\ \mathbf{E}_y(x) &= C e^{\alpha x} & x < -d/2 & \text{ cladding} \\ \mathbf{E}_y(x) &= D e^{-\alpha x} & x > d/2 & \text{ cladding} \end{aligned} \quad (2.23)$$

For TM modes the same analysis for symmetric mode scan be made giving the conditions

$$\begin{aligned} \mathbf{H}_y(x) &= A \cos kx & |x| < \frac{d}{2} \\ \mathbf{H}_y(x) &= C e^{-\alpha|x|} & |x| > \frac{d}{2} \end{aligned} \quad (2.24)$$

Depending on whether the longitudinal components are zero, the solutions of the modes can be classified as transverse electric (TE), transverse magnetic (TM), transverse electric and magnetic (TEM) or hybrid.

$E_z=0$	$H_z=0$	TEM modes
$E_z=0$	$H_z \neq 0$	TE or H modes
$E_z \neq 0$	$H_z=0$	TM or E modes
$E_z \neq 0$	$H_z \neq 0$	Hybrid or HE or HE modes

Table 2.2 Classification of the types of longitudinal components

There are five parameters that need consideration when designing a slab waveguide that aid in understanding guiding characteristics such as mode field distribution and the effective refractive index and hence phase velocity. These parameters are the thin-film thickness  $d$ , the free space wavelength  $\lambda$  and the refractive indices of the under-cladding  $n_2$ , the waveguide core layer  $n_1$  and the over-cladding  $n_3$  [8] [9].

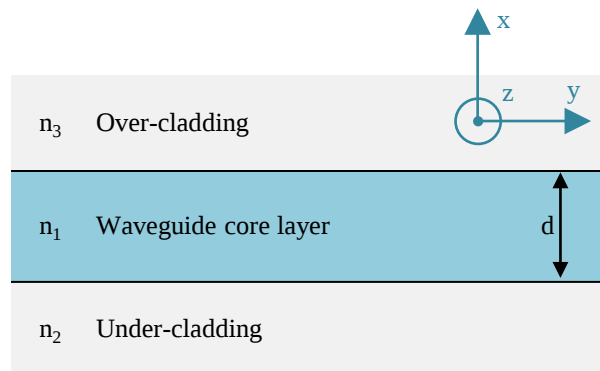


Figure 2.2 2D cross-section of planar waveguide, showing the dimensional parameters considered when designing a slab waveguide.

The normalised waveguide parameters are a set of dimensionless equations used to characterize modal properties of a waveguide. The normalized frequency  $V$  (also known as V number), is the first basic guiding parameter and is defined by

$$V = \frac{2\pi}{\lambda} d \sqrt{n_1^2 - n_2^2} \quad (2.25)$$

The V number can also give information on the number of propagating modes, where the number of guided modes is equal to  $V/\pi$  and single mode operation occurs when  $V < \pi$ .

The next parameter that needs consideration is the propagation constant  $\beta$ , related to the normalised guide index

$$b = \frac{\beta^2 - k_1^2}{k_1^2 - k_2^2} = \frac{n_{eff}^2 - n_2^2}{n_1^2 - n_2^2} \quad (2.26)$$

where  $k_1$  and  $k_2$  are the wave numbers given by

$$k_1 = \frac{n_1 \omega}{c} \quad \& \quad k_2 = \frac{n_2 \omega}{c} \quad (2.27)$$

where  $\omega$  is the angular frequency of the propagating wave and  $c$  is the speed of light in vacuum.

To describe the refractive index asymmetry of the waveguide, an asymmetry factor for TE modes,  $a_E$  and TM modes,  $a_M$  is used and described in equations (2.28) and (2.29).

For TE modes:

$$a_E = \frac{n_2^2 - n_3^2}{n_1^2 - n_2^2} \quad (2.28)$$

For TM modes:

$$a_M = \frac{n_1^4(n_2^2 - n_3^2)}{n_3^4(n_1^2 - n_2^2)} \quad (2.29)$$

For an asymmetric waveguide structure the TM asymmetry factor  $a_M$  is greater than the TE asymmetry factor  $a_E$ . While for a symmetric structure the refractive indices of the under-cladding  $n_2$  and the over-cladding  $n_3$  are equal leading to TM and TE asymmetry factor both equalling zero. Finally the equations for the modes in a waveguide in TE and TM polarizations are given by

For TE modes:

$$V\sqrt{1-b} = p\pi + \tan^{-1} \sqrt{\frac{b}{1-b}} + \tan^{-1} \sqrt{\frac{b+a_E}{1-b}} \quad (2.30)$$

For TM modes:

$$V\sqrt{1-b} = p\pi + \tan^{-1} \frac{n_1^2}{n_3^2} \sqrt{\frac{b}{1-b}} + \tan^{-1} \frac{n_1^2}{n_2^2} \sqrt{\frac{b+a_E}{1-b}} \quad (2.31)$$

where  $p = 0, 1, 2 \dots$  ( $p$  is the mode number, beginning with fundamental mode at  $p = 0$ ).

The equations for the propagating waveguide modes are also known as the normalised dispersion equations and are shown in figure 2.3 for TE modes. The fundamental, second, third, fourth and

fifth order propagation modes ( $p = 0, 1, 2, 3, 4$ ) are plotted for different asymmetry values of  $a_E = 0, 1$  and  $\infty$ .

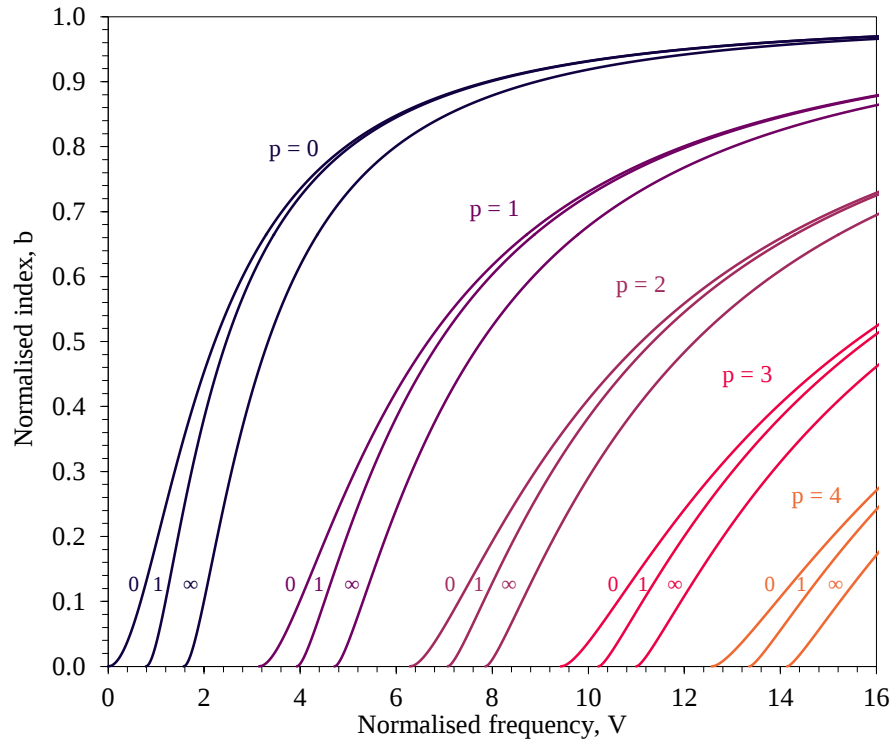


Figure 2.3 TE modes normalised dispersion curves plotted using equation (2.30).

At cut-off  $b = 0$  and  $p = 0$  for the lowest mode, the normalised dispersion equations for the fundamental modes in the TE and TM polarisations become

$$\text{TE modes: } V_0 = \tan^{-1} \sqrt{a} \quad (2.32)$$

$$\text{TM modes: } V_0 = \tan^{-1} \frac{n_1^2}{n_3^2} \sqrt{a} \quad (2.33)$$

The effective refractive index (or effective index,  $n_{eff}$ ) is a convenient waveguiding propagation parameter which describes the phase delay in a waveguide per unit length, relative to the phase delay in vacuum. This parameter depends on the wavelength of the propagating electromagnetic wave and the mode the lights propagating in [10]. The effective index is described by the expression

$$n_{eff} = \frac{c}{v_p} = \frac{\beta}{k} \quad (2.34)$$

where  $k$  is the wave number and  $v_p$  is the phase velocity given by

$$v_p = \frac{\omega}{\beta} = \frac{c}{n} \quad (2.35)$$

where  $\omega$  is the angular frequency of the propagating wave and  $c$  is the speed of light in vacuum.

## 2.3 Approximate theoretical methods for analysis and design of rib structured waveguides

This section introduces some of the theoretical methods for analysing and designing rib waveguides. The first method by Soref et al. [11], is a widely used and accepted approach for determining the single mode conditions for a rib waveguide from dimensions of the rib structure. The single mode guidance equation is used to determine the initial basic design of the rib waveguide as a starting point for accurate simulation of the modal characteristics introduced in section 2.4, to refine the design of the rib waveguide. The second method, the effective index method [12] [13] is a simple analysis tool to determine the approximate effective indices of channel waveguide modes using the refractive indices and thicknesses of the core and cladding layers.

### 2.3.1 Single mode condition for rib waveguides

A slab waveguide configuration discussed in the previous section highlighted some of the most important features of optical waveguide, but guiding the light radiation within a planar configuration is not useful for many practical applications because of the infinite spatial range of the propagating wave form in the plane parallel to the substrate. More complex channel waveguide structures, illustrated in figure 2.4, are used for most practical applications as the mode profile of the propagating structure can be tailored in both the horizontal,  $w_y$  and vertical directions,  $w_x$ . For this project a rib waveguide structure is developed because it is a structure that can be easily photolithographically defined using conventional photolithography fabrication technology due to its large cross-sectional dimensions of several microns while supporting SM mode waveguiding, have efficient coupling (due to large mode size) to input and output fibres, and tailored to be single moded with low losses.

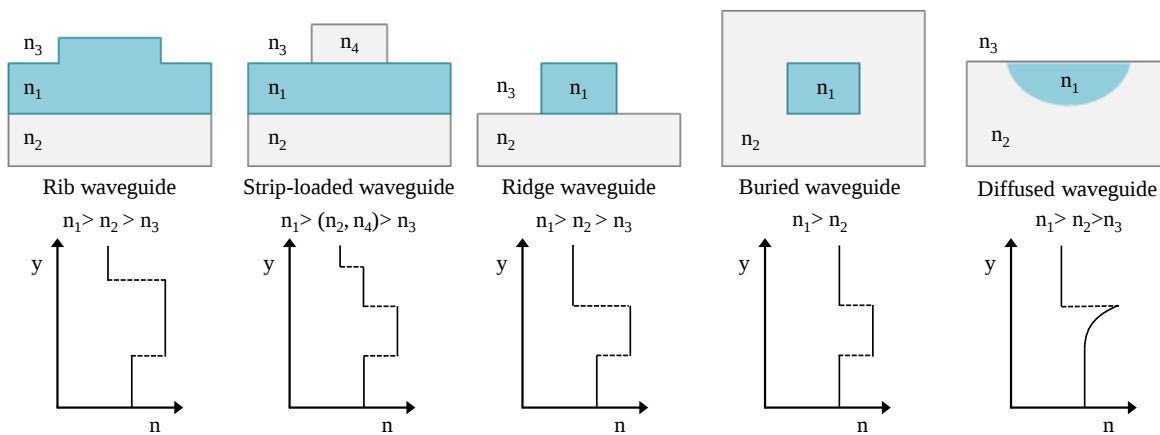


Figure 2.4 Examples of different waveguide cross-sections.

For rib waveguide structures the well-known approximate expression of Soref for single-mode condition [11], useful for initial estimates of waveguide parameters is given by

$$\frac{W}{H} \leq \alpha + \frac{r}{\sqrt{1-r^2}} \quad (2.36)$$

where  $W$  is the width of the waveguide,  $H$  is the rib height,  $r (= h/H)$  is the fractional height of the side slab regions compared to the inner rib centre,  $h (= H - D)$  is the slab region height,  $D$  is the etch depth and  $\alpha$  is a constant, as illustrated in figure 2.5. There are two conditions which need to be met for a good approximation: firstly the fractional height of the two regions, expressed by  $r$  must satisfy the condition  $0.5 \leq r < 1$ ; and secondly the waveguide dimensions needs to be greater than the operating wavelength [14].

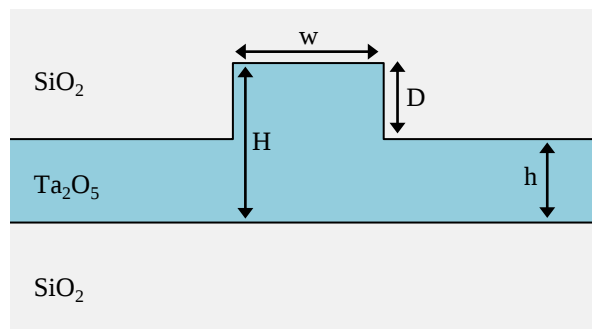


Figure 2.5 A  $\text{Ta}_2\text{O}_5$  rib waveguide cross-section where the dimensions are represented by  $W$  (width of the waveguide),  $H$  (rib height),  $D$  (etch depth) and  $h$  (slab region height).

The constant  $\alpha$  is a parameter whose value depends on the approximations used. This key parameter for the single mode guidance equation was established through the effective index method giving  $\alpha = 0$  [15] and by a mode matching analysis by Soref et al. giving  $\alpha = 0.3$  [11]. Figure 2.6 shows the boundary defining mono-mode operation in terms of  $W$ ,  $H$  and  $h$ , highlighting the difference between the two approximations for  $\alpha$ .

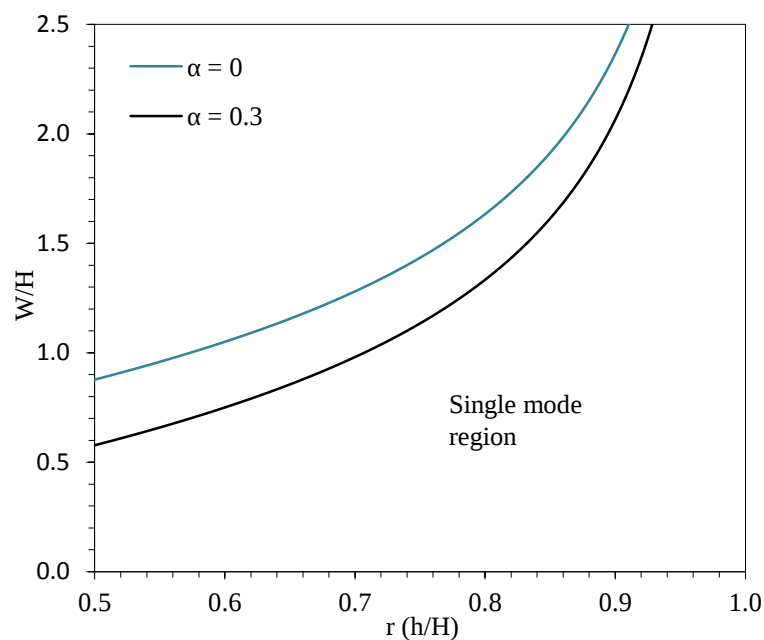


Figure 2.6 Single mode condition for  $\alpha = 0$  and  $\alpha = 0.3$ .

### 2.3.2 Effective index method

The effective index method is a method simplifying a 2D confined waveguide so that it can be approximately modelled as a slab waveguide for calculating an approximate value of the effective indices for propagating modes of complex channel waveguides. The concept behind the effective index method is to convert a 2D channel waveguide, figure 2.7a into two 1D planar waveguide structures, one in x and z axis (figure 2.7b) and the other in the z and y axis (figure 2.7c) [13]. The effective indices for the three separate regions I, II and III are calculated for each varying thickness of the film,  $H$ . These effective indices are calculated using the normalised waveguide parameters introduced in section 2.3 by firstly calculating the normalised frequency using equation (2.25), then using the normalised dispersion curves, figure 2.3 to select the corresponding normalised index,  $b$ . By rearranging equation (2.26) and substituting the normalised index, the effective index can be found. These calculated effective indices are then placed into the planar structure in x and z axis to represent the modal effective index in the z direction. These calculated effective indices are of a slab waveguide, therefore to calculate the effective index of the rib structure the width of the channel,  $W$  must be taken into consideration. This is achieved by recalculating the effective indices for  $W$  by using calculated effective indices for the slab geometry and following the same procedure outline above. For the effective index method to be an acceptable approximation the condition that the waveguide's width must be greater than its thickness must be satisfied [12].

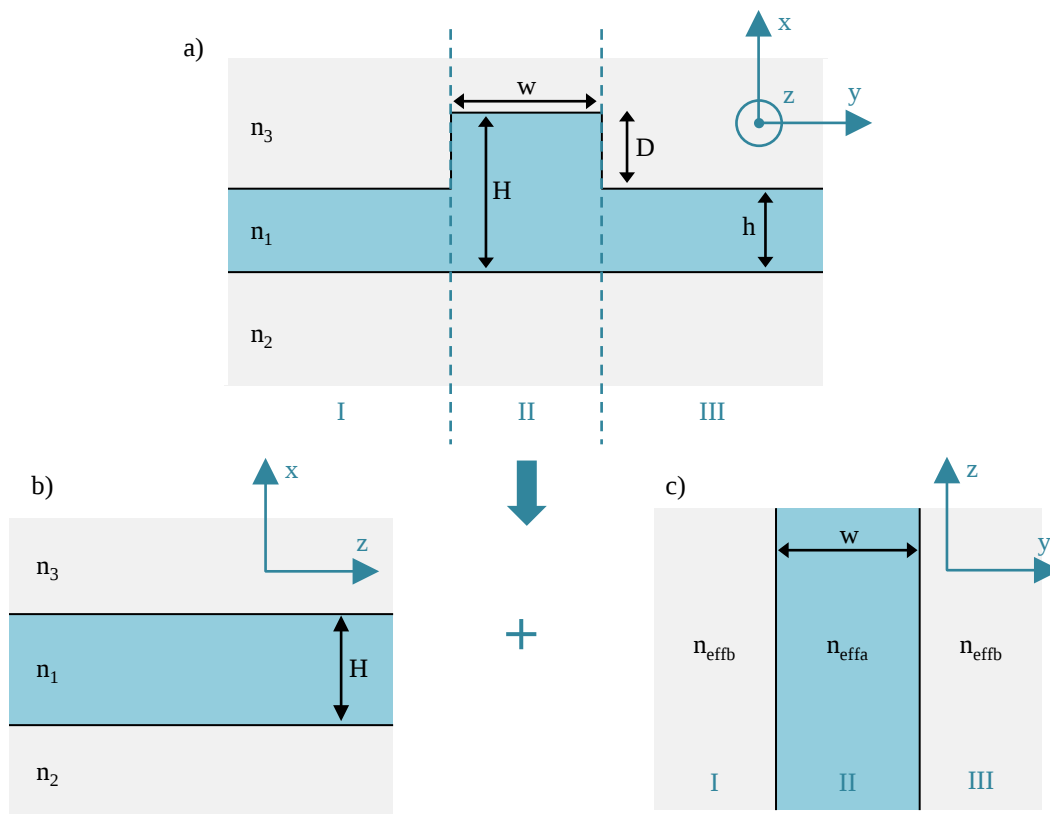


Figure 2.7 Effective index method.

## 2.4 Simulations of mode profiles of rib waveguides

This section presents the modelling procedure for the analysis of the propagating mode within a rib waveguide structure. The principal aim is to investigate how the dimensions of the rib structure changes the shape and size of the mode intensity profiles, with the intention of finding an optimum design for a circular mode profile with most of the light in the core for small spot sizes to maximize confinement of light. This will allow for better input/output fibre connectivity while reducing the intensity distribution within the waveguide to increased light intensity for a given modal power, leading to low threshold lasing and low power non-linear behaviour, because by reducing the spot size of the pump and lasing light propagating in a cavity will lead to lower laser thresholds [16]. The main tool used for the modelling and simulations of optical devices is COMSOL multi-physics finite element analysis software.

Knowing the effect of changing the dimensions of the waveguide channel on the propagating modes is important as not only does the shape of the mode profile change, but also the corresponding effective indices. Therefore the waveguide dimensional parameters which were varied to investigate mode profile through COMSOL simulations were the widths of the rib and etch depth (height of difference between the inner rib and outer slab heights) with the Ta<sub>2</sub>O<sub>5</sub> core thickness (inner rib region) and over- and under-cladding kept at a constant. The material properties entered into the model, shown in figure 2.8 were the refractive indices for the SiO<sub>2</sub> over- and under-cladding and the Ta<sub>2</sub>O<sub>5</sub> core layer. The wavelength of the propagating electromagnetic wave selected for the simulation was 980 nm, as it is close to range of the operating wavelength of the laser pump source  $\approx 977$  nm as well as close to the expect wavelength of a typical Yb-doped lasers [17]. At 980 nm the refractive index of SiO<sub>2</sub> is 1.46 [18] and for Ta<sub>2</sub>O<sub>5</sub> it is 2.124 [19], and these values were selected for the material properties in these simulations.

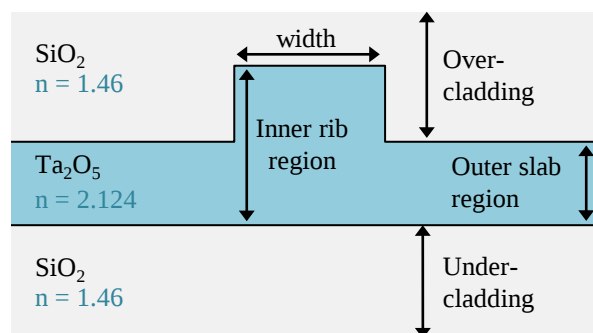


Figure 2.8 Rib waveguide structure showing the dimensions and materials properties used in the COMSOL model.

The designs of fabricated rib waveguides, the core layer (inner rib region) was taken to have a thickness of 1  $\mu\text{m}$ , SiO<sub>2</sub> under-cladding thickness of 2.5  $\mu\text{m}$  and over-cladding of 2  $\mu\text{m}$ . A 1  $\mu\text{m}$  rib height was chosen for the core as it would ensure good confinement of light in the vertical direction and would keep the amount of time required for deposition down, with deposition rate was found to be  $\approx 1.75$  nm/min for Ta<sub>2</sub>O<sub>5</sub> using a RF magnetron sputtering deposition system [19]. The over-

cladding acts as a protective layer for the rib waveguide from external influences and creates the symmetrical waveguide system. A thickness of 2  $\mu\text{m}$  is considered close to infinitely large for the decaying light so it will become negligible small hence adequate for this design. Rib widths were simulated from 0.3  $\mu\text{m}$  to 1.9  $\mu\text{m}$  (0.2  $\mu\text{m}$  increments) and between 2  $\mu\text{m}$  to 20  $\mu\text{m}$  (1  $\mu\text{m}$  increments) for etch depths of 150 nm, 300 nm, 500 nm and 1  $\mu\text{m}$ . The etch depth of 150 nm was selected as a starting point for the simulations. This starting value was chosen based upon Soref's single mode conditions by select the fractional height,  $r = 0.85$  as this value satisfies the condition  $0.5 \leq r < 1$ , which gives an outer slab region of 850 nm (etch depth of 150 nm) for film thickness of 1  $\mu\text{m}$  (inner rib region). The selected values for Soref's guidance equation imply that single mode propagation will occur for rib widths,  $w \leq 1.914 \mu\text{m}$  for an etch depth of 150 nm.

For each simulated rib waveguide design, the model was set to find the fundamental modes and their corresponding effective indices close to the expected effective index for the fundamental TE and TM modes, by using the effective index method [12]. From the different modes found by the simulation, the fundamental mode was selected by inspection of graphical plots of the electric field (using "electric field norm" which is a COMSOL defined absolute scalar value of the electric field). Figure 2.9 shows the normalised electric field for the fundamental mode of a rib with height 1  $\mu\text{m}$ , width 2  $\mu\text{m}$  and an etch depth of 150 nm.

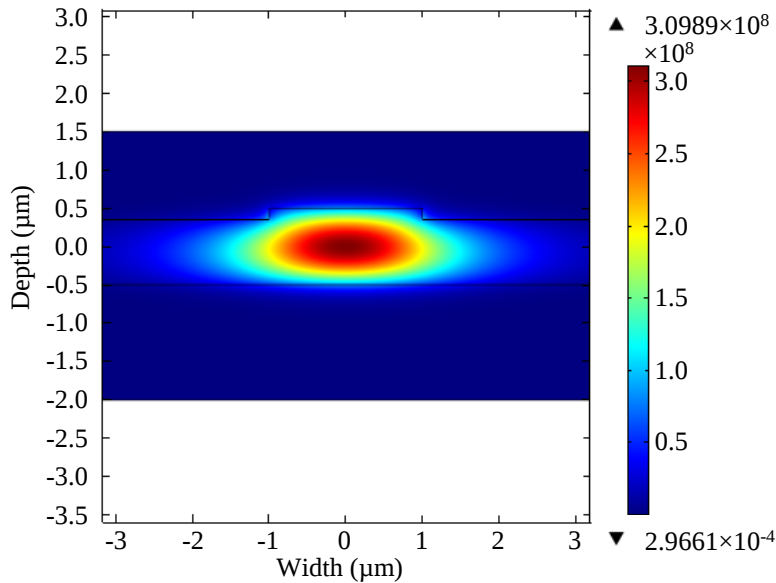


Figure 2.9 COMSOL simulated rib waveguide mode profile. Rib dimensions: height  $H = 1 \mu\text{m}$ , width  $W = 2 \mu\text{m}$  and etch depth  $D = 150 \text{ nm}$ .

The qualitative intensity profiles of the fundamental mode are presented by taking a line of data point, through the highest point of the electric field of the mode in both the horizontal and vertical directions, as shown in figure 2.10. The extrapolated electric field were exported to Matlab and their mode intensity profiles were calculated to find the spot sizes at full width at half maximum (FWHM) which were calculated using a Matlab script (Appendix A), in order to study minimisation and circularity of the modal distribution.

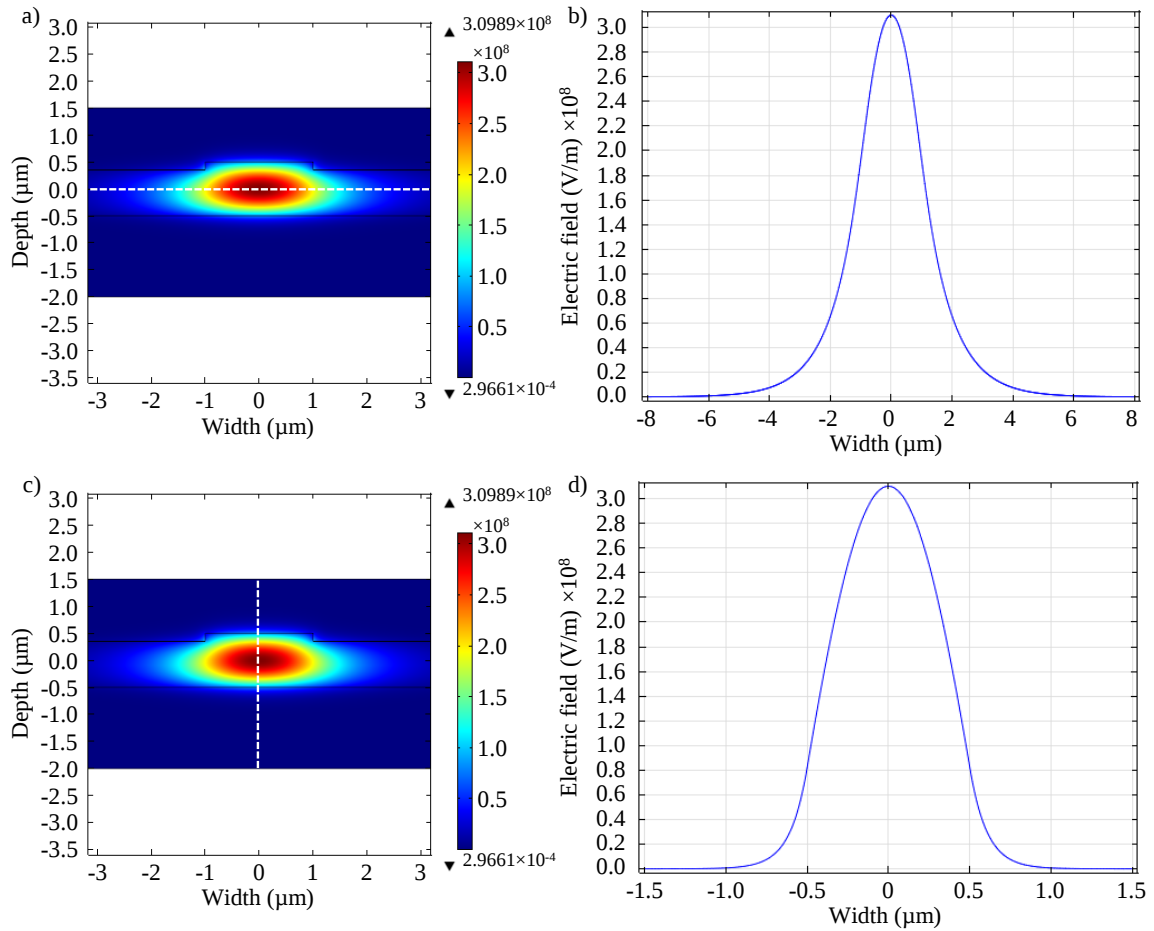


Figure 2.10 Fundamental electric field mode profile of rib waveguide with height  $H = 1 \mu\text{m}$ , width  $W = 2 \mu\text{m}$  and etch depth  $D = 150 \text{ nm}$  with cut line (white dotted line) in a) horizontal direction,  $w_y$  & c) vertical direction,  $w_x$  along with the corresponding normalised electric fields in b) horizontal direction,  $w_y$  & d) vertical direction,  $w_x$ .

To ascertain the polarization of the mode found by COMSOL, a comparison of the horizontal and vertical components of the electric field strength along the horizontal direction was made. If the mode exhibits a strong electric field for the horizontal component and weak electric field for the vertical component then the mode is quasi-TM. But if there is strong electric field for the vertical component and weak electric field for the horizontal component then the mode is quasi-TE [20]. The polarization was found by analysing the mode intensity profile by taking a cross-section cut line in the horizontal direction (same process used to calculate the FWHM) and then plotted the horizontal and vertical components against each other to compare the field strength. Figure 2.11 shows an example of the normalised electric field and mode profiles for a fundamental mode of different polarizations. The rib design has an inner rib height of  $1 \mu\text{m}$  etch, depth of  $500 \text{ nm}$  and a rib width of  $2 \mu\text{m}$ . The vector components of the electric (white arrows) and magnetic (black arrows) fields for single modes are shown on the normalised electric field plots, indicating that figure 2.11a is quasi-TM polarised and figure 2.11c is quasi-TE with effective indices of 2.074 and 2.066 respectively. The mode intensity profiles plotted in figure 2.11b and figure 2.11d shows corresponding vertical and horizontal components of the normalised electric field plots for the

fundamental mode, with strong electric field in the horizontal displaying quasi-TM polarisation and with strong electric field in the vertical displaying the quasi-TE polarisations.

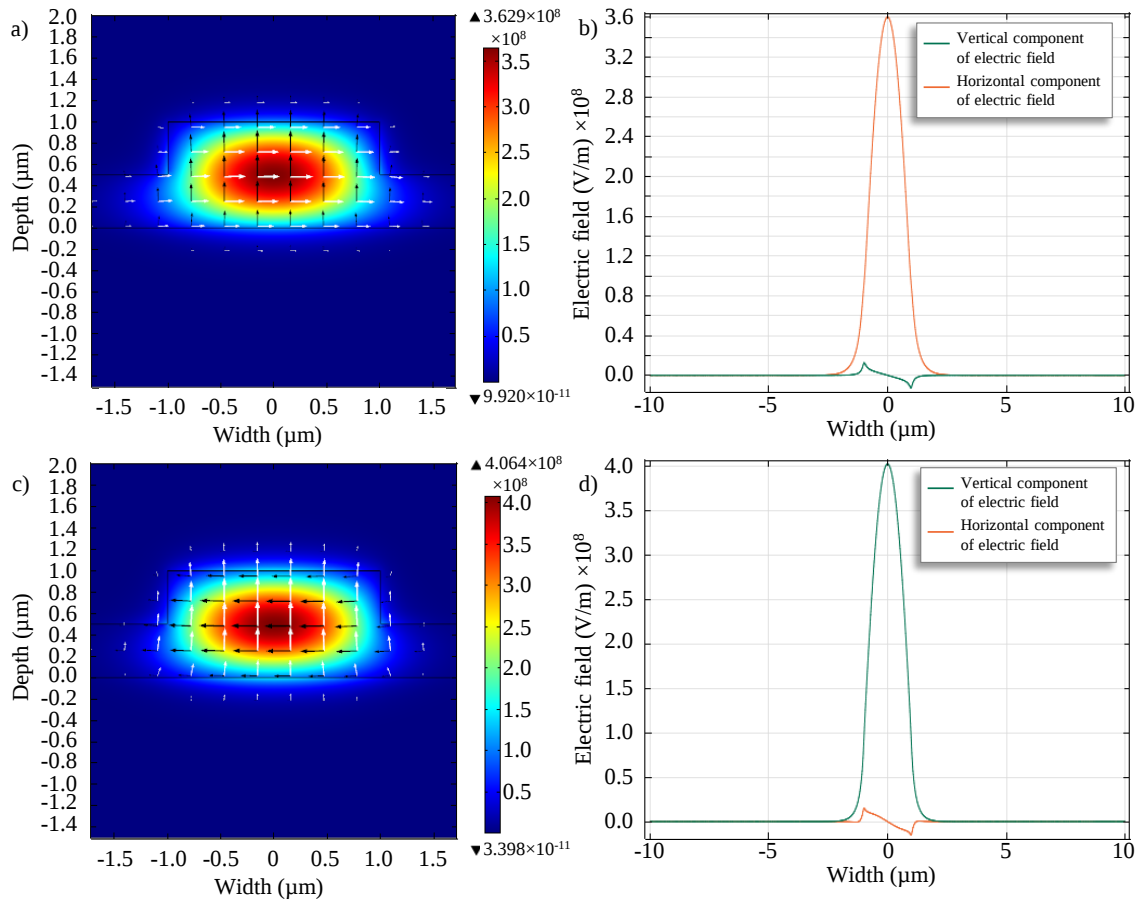


Figure 2.11 An example of normalised electric field with arrows illustrating direction of electric (white) and magnetic field (black) for polarisations a) quasi-TM & c) quasi-TE, along with the corresponding vertical and horizontal components of the electric field for polarisations b) quasi-TM & d) quasi-TE. Rib dimensions: height  $H = 1 \mu\text{m}$ , width  $W = 2 \mu\text{m}$  and etch depth  $D = 500 \text{ nm}$ .

Figure 2.12 shows the fundamental mode effective indices for quasi-TM polarisation of the simulated waveguide modes with respect to rib width for the four selected etch depths (150 nm, 300 nm, 500 nm and  $1 \mu\text{m}$ ). All the figures indicate a rapid increase in the effective index as the width of the rib increases from  $0.3 \mu\text{m}$  to  $5 \mu\text{m}$ , which approaches asymptotically the value of 2.085. This effective index value occurs due to the rib width increasing to a size where it begins to approximate a slab waveguide as the mode intensity profile no longer significantly penetrates the outer slab region. This was confirmed by evaluating the effective refractive index of a slab waveguide structure, giving an effective refractive index of 2.085 for a  $1 \mu\text{m}$  thick layer  $\text{Ta}_2\text{O}_5$  layer ( $n_1 = 2.124$ ) encapsulated in  $\text{SiO}_2$  ( $n_2 = n_3 = 1.46$ ) layers with a propagating wavelength of  $\lambda = 980 \text{ nm}$ . When the rib width is  $0.3 \mu\text{m}$  it is close to the structure of a slab waveguide with a thickness of the outer slab region. The rib waveguides were shown to begin to support multimode propagation for rib widths  $\geq 2.7 \mu\text{m}$  for 150 nm etch depth,  $\geq 1.9 \mu\text{m}$  for 300 nm etch depth,  $\geq 1.3 \mu\text{m}$  for 500 nm etch depth, with a buried channel (etch depth of  $1 \mu\text{m}$ ) displaying multimode support regardless of the width of the channel.

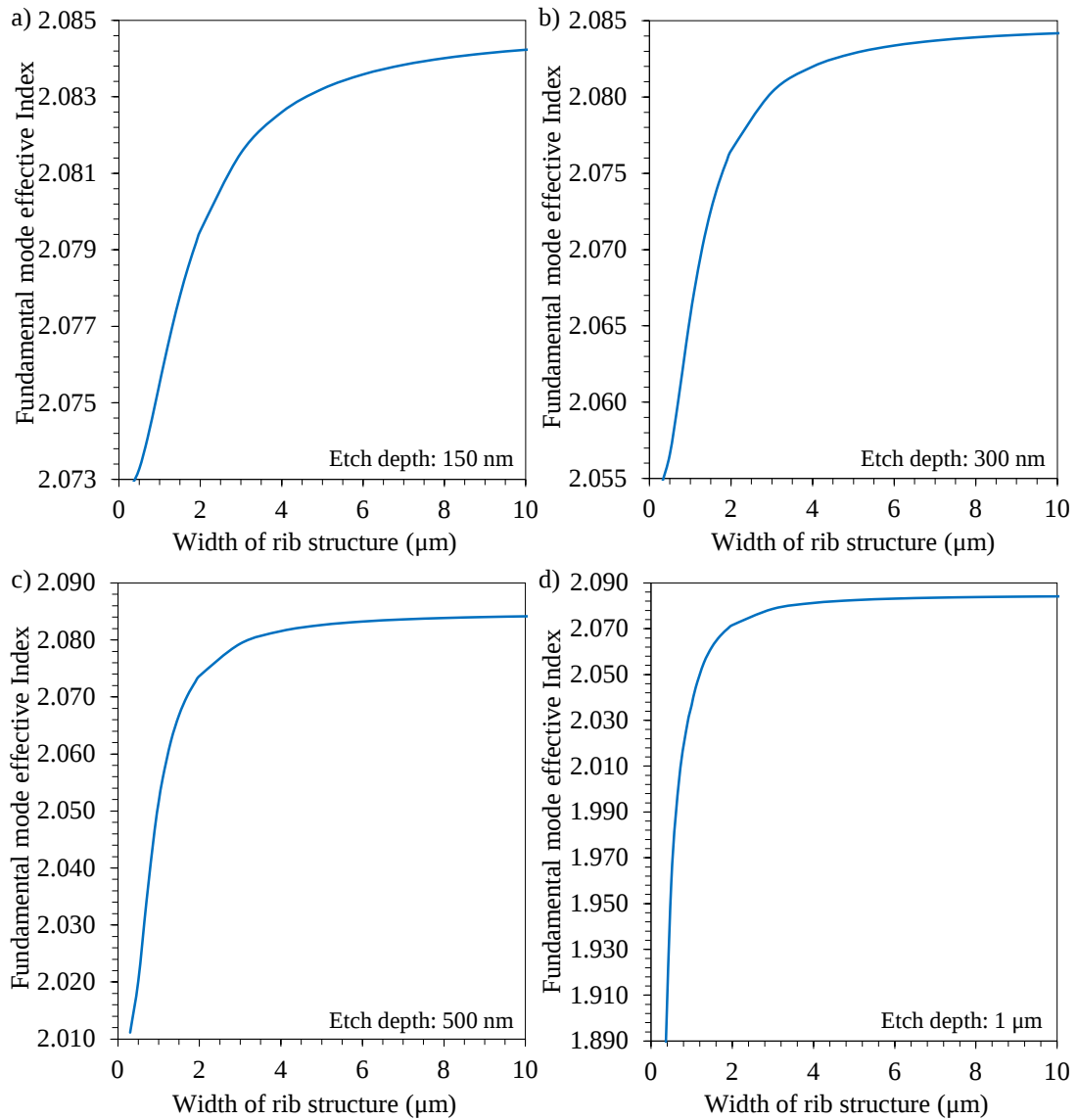


Figure 2.12 Fundamental mode effective indices for quasi-TM polarisation of rib waveguides with etch depths of a) 150 nm, b) 300 nm, c) 500 nm, & d) 1  $\mu\text{m}$ .

Figure 2.13 shows a comparison of the effective indices deduced from the COMSOL model and the effective index method. For the comparison, the simulation result of a rib width of 0.3  $\mu\text{m}$  for the different etch depths is used as this structure is close to that of a slab waveguide with a thickness of the outer slab region. Therefore by comparing to the effective index method for core thicknesses of 1  $\mu\text{m}$  (etch depth = 0  $\mu\text{m}$ ), 0.85  $\mu\text{m}$  (etch depth = 0.15  $\mu\text{m}$ ), 0.7  $\mu\text{m}$  (etch depth = 0.3  $\mu\text{m}$ ), 0.5  $\mu\text{m}$  (etch depth = 0.5  $\mu\text{m}$ ) we are able to validate effective indices determined by COMSOL. The effective indices calculated using the effective index method follow closely the COMSOL simulated structure until the etch depths gets closer to the limit of the effective index method, where the width of the waveguide becomes less than its thickness, in this case the thickness of the outer slab. The FWHM spot sizes of the mode intensity distributions calculated for etch depths of 150 nm, 300 nm, 500 nm and 1  $\mu\text{m}$  as a function of rib width is shown in figure 2.14 to figure 2.17. Spot sizes in the vertical direction increase from 0.55  $\mu\text{m}$  to 0.6  $\mu\text{m}$  but remain unchanged ( $\approx$  0.6  $\mu\text{m}$ ) for widths greater than 1  $\mu\text{m}$ .

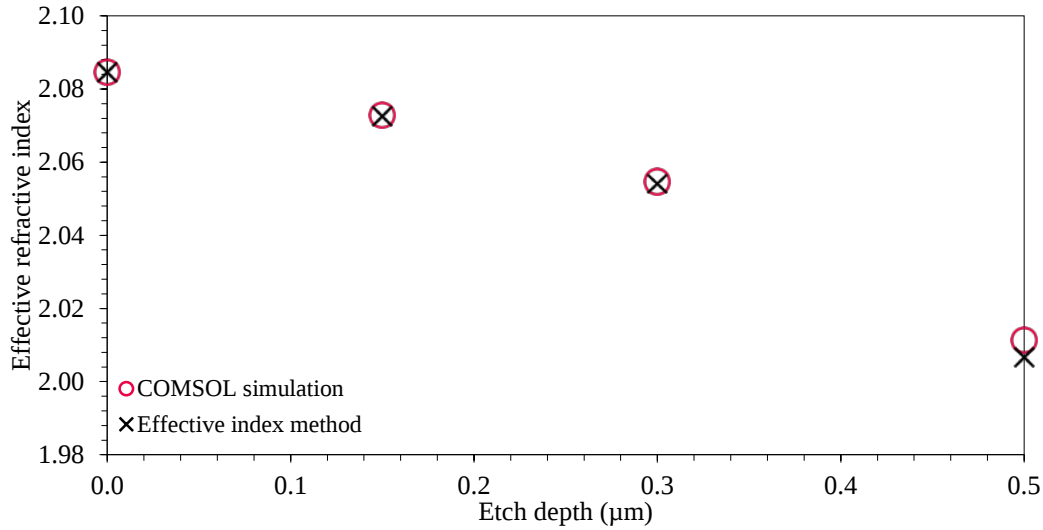


Figure 2.13 Comparison of effective indices for different etch depths from COMSOL simulation and effective index method. Width  $w = 0.3 \mu\text{m}$ .

The FWHM spot size of the mode intensity profiles in the horizontal direction for etch depths of 150 nm, 300 nm and 500 nm (figure 2.14, figure 2.15 and figure 2.16) show that the smallest spot size occurs for structures with a rib width close to  $1 \mu\text{m}$  width this spot size increases as the width of the waveguide increases or decreases from the point of smallest spot size. The spot sizes are shown to reduce in size as etch depth is increased as more of the light is confined within the guiding core. This indicates that to achieve a rib structure with a circular intensity distribution with maximum confinement of light should have an etch depth of 500 nm with a rib width of  $1 \mu\text{m}$  for this initial slab height,  $H$ . Figure 2.17 shows the spot size for a structure with width and etch depth of  $1 \mu\text{m}$ , representing a fully etched waveguide yielding a mode profile is smaller for widths less than  $1 \mu\text{m}$  in contrast to other simulated waveguides.

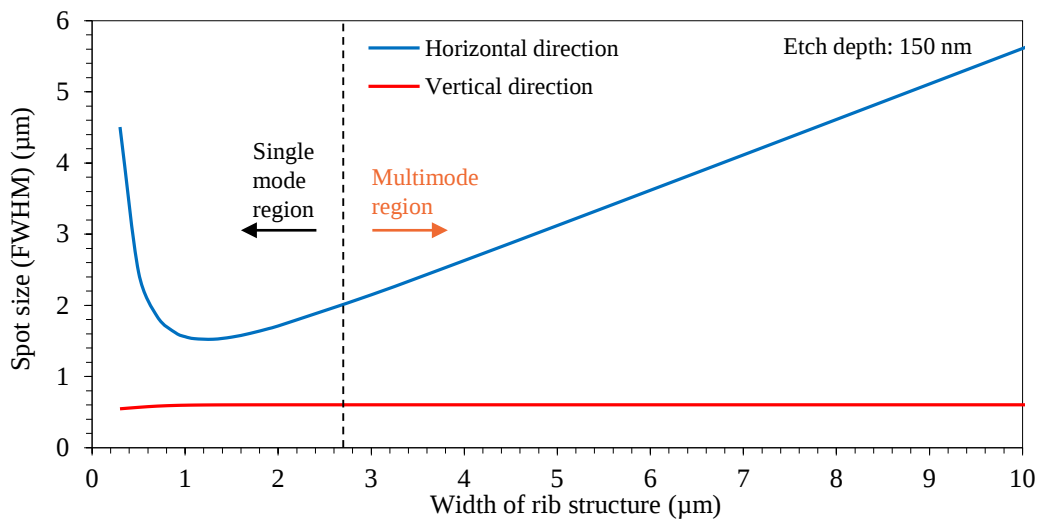


Figure 2.14 FWHM of spot sizes in the horizontal and vertical direction for a rib with 150 nm etch depth.

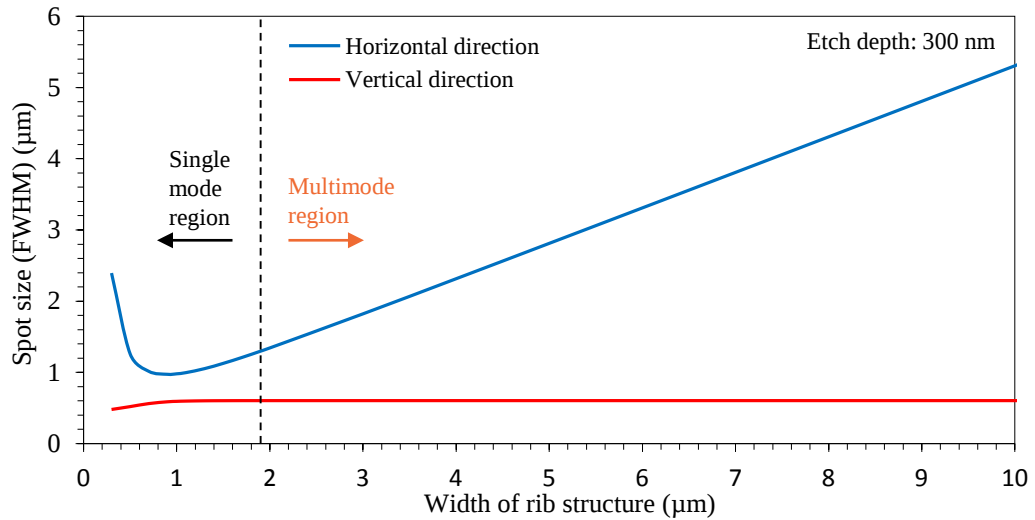


Figure 2.15 FWHM of spot sizes in the horizontal and vertical direction for a rib with 300 nm etch depth.

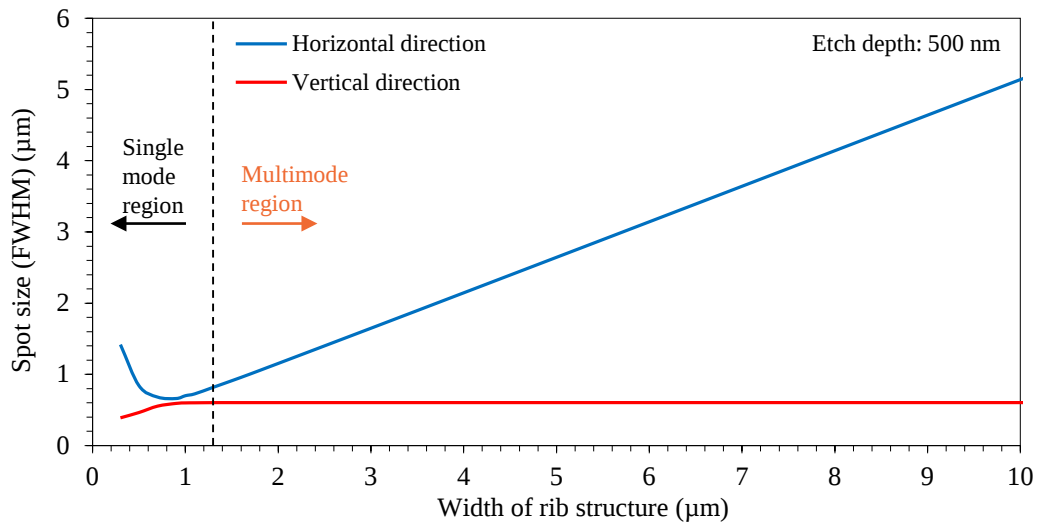
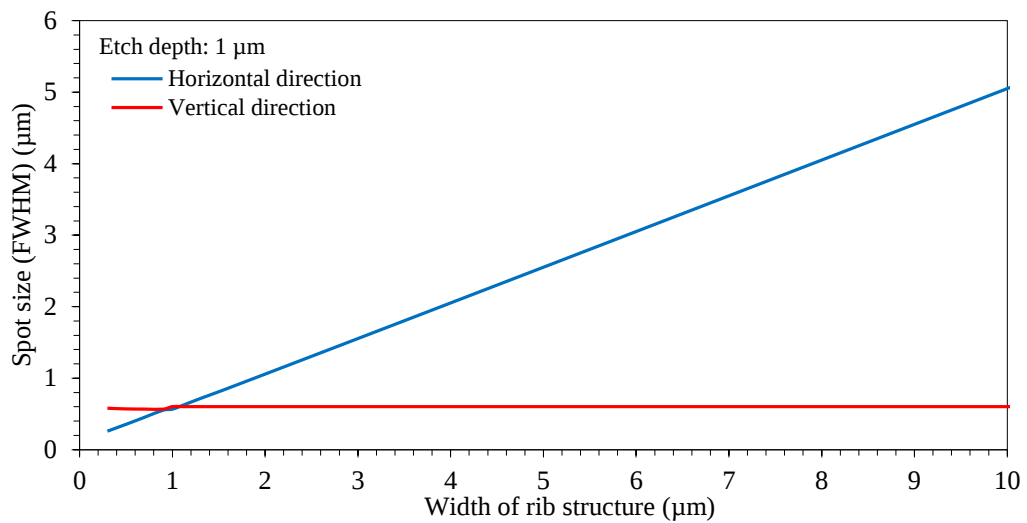


Figure 2.16 FWHM of spot sizes in the horizontal and vertical direction for a rib with 500 nm etch depth.

Figure 2.17 FWHM of spot sizes in the horizontal and vertical direction for a rib with 1  $\mu\text{m}$  etch depth.

The mode intensity profiles investigated using finite element analysis aid in developing a symmetrical rib waveguides where the cross-sectional dimensions can be tailored for compact

confinement of light propagating with desired mode intensity shape. A circular mode intensity profile can be achieved by fabricating a rib with a height of 1  $\mu\text{m}$ , width 1  $\mu\text{m}$ , and etched by 500 nm with this structure also having the smallest spot size which is desirable for waveguide lasers.

## 2.5 Simulations of integrated planar Kerr lens in $\text{Ta}_2\text{O}_5$

In this section the modelling and simulations of integrated planar Kerr lens devices in  $\text{Ta}_2\text{O}_5$  material is presented. The Kerr lens phenomenon is based on the optical Kerr effect, a non-linear effect which causes the refractive index of a material to change in response to an applied electric field, for the case of an optical beam is proportional to the local irradiance of the light.

This non-linear effect is based on the third-order non-linear susceptibilities  $\chi^{(3)}$  which describes that change in refractive index of a material occurs for high intensity waves [7]. This intensity dependant refractive index behaviour is described by

$$n = n_0 + n_2 I \quad (2.37)$$

where  $n_0$  is the linear refractive index of the material,  $n_2$  is the non-linear refractive coefficient and  $I$  is the beam intensity. Passing a beam through a material with a high third-order non-linear susceptibility will cause the propagating wave front to see a higher refractive index in the centre (area of highest intensity) and a lower refractive index at the outer wings (area of lowest intensity), which causes the wave front to curve and exhibit a focusing effect, as illustrated in figure 2.18. This is known as self-focusing and combined with an aperture it can be used within a laser cavity as a passive non-linear modelocking element for the generation of ultrafast lasers [5].

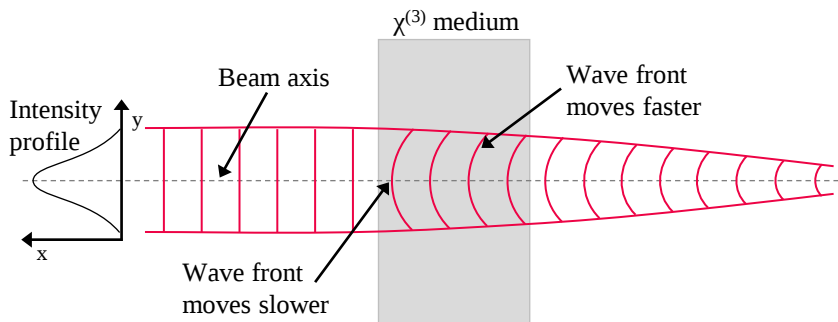


Figure 2.18 Self-focusing mechanism of wave front passing through  $\chi^{(3)}$  medium utilizing the Kerr effect.

The planar Kerr lens element was simulated in COMSOL, building on previous simulations in section 2.4, carried out to investigate the mode intensity profiles of rib waveguides in  $\text{Ta}_2\text{O}_5$ . The aim is to model the Kerr effect in a  $\text{Ta}_2\text{O}_5$  planar structure as the propagating light diffracts in a slab region and investigate what optical intensities and geometric structure and dimensions are needed to take advantage of the Kerr effect, in particular the amount of achievable modulation

depth. The modulation depth is the maximum change in transmission or reflectivity of a modelocking element and is important as it can determine whether the modelocked laser will be stable, able to self-start as well as optimisation of pulse duration. This value is typically within a few percent for fast saturable absorbers such as semiconductor saturable absorber mirror (SESAM) [21].

The design for the planar Kerr element simulation, shown in figure 2.19 is a 2D model comprising of a channel waveguide launching light at a wavelength of  $\lambda = 980$  nm into an open slab region where the light is allowed to diffract. Within this region the light is diffracted for a certain length,  $K_L$  (Kerr element length) before entering into an output waveguide, which also acts as an internal hard aperture. This 2D model is based on silica over- and under-cladded symmetrical rib waveguides simulated in section 2.4 with a core thickness,  $H$  of  $1 \mu\text{m}$ , an etch depth,  $D$  of  $0.15 \mu\text{m}$  and rib width,  $W$  of  $1 \mu\text{m}$  and is designed taking into consideration light propagating along the  $z$  axis and mode intensity profile in the  $y$  axis. The effective index method was used to calculate the effective indices for the inner rib region ( $n_{effa} = 2.0847$ ) and outer slab region ( $n_{effb} = 2.0726$ ) with the Kerr element open slab region having the same effective index of the inner rib region.

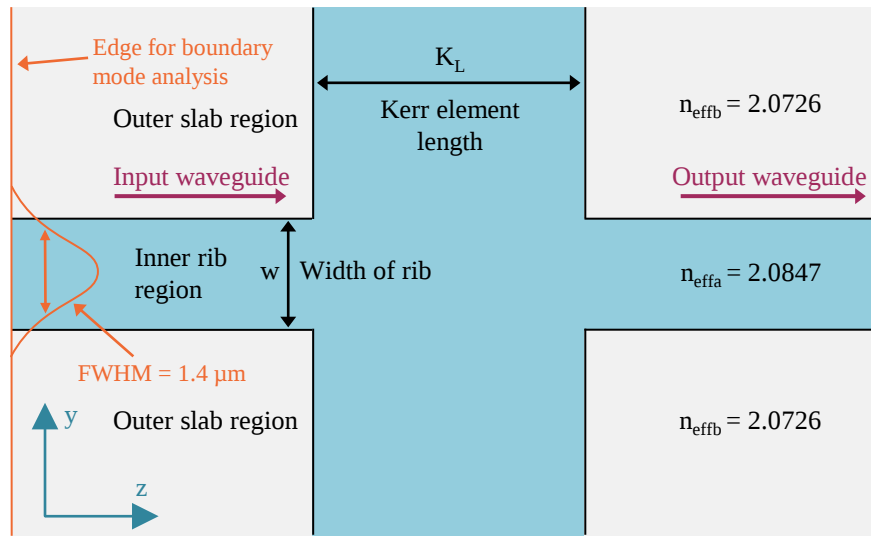


Figure 2.19 2D top down view of planar Kerr lens element in  $\text{Ta}_2\text{O}_5$  enclosed in  $\text{SiO}_2$  over- and under-cladding.

To incorporate the third-order non-linear behaviour into the COMSOL simulation, the material property of the guiding region has both the linear refractive index and intensity dependent third-order non-linear refractive index. Therefore based upon equation (2.37) the material property becomes

$$n = n_{effa} + n_2 I \quad (2.38)$$

where the linear refractive effective index (waveguide core),  $n_{effa}$  is 2.0847,  $I$  is the intensity of the input laser beam in  $\text{W}/\text{m}^2$ , and  $n_2$  is the third-order non-linear refractive index in  $\text{m}^2/\text{W}$ . The third-order non-linear refractive index for  $\text{Ta}_2\text{O}_5$  at a wavelength of 980 nm is  $7.25 \times 10^{-19} \text{ m}^2/\text{W}$

[22]. Table 2.3 shows the dimensional and material properties used within the simulation of the planar Kerr lens simulation. To simulate launching light at a wavelength of 980 nm, a boundary modal analysis was carried out along the edge of the input waveguide to determine and launch the fundamental mode of the waveguide.

Symbol	Property	Units or Numerical Value
$H$	Inner rib core thickness	1 $\mu\text{m}$
$D$	Etch depth	0.15 $\mu\text{m}$
$W$	Width of rib waveguide	1 $\mu\text{m}$
$\lambda$	Wavelength of input beam	980 nm
$n_{effa}$	Inner rib region effective index	2.0847
$n_{effb}$	Outer slab region effective index	2.0726
$I$	Intensity of input laser beam	$\text{W}/\text{m}^2$
$n_2$	Third-order non-linear refractive index	$7.25 \times 10^{-19} \text{ m}^2/\text{W}$
$n$	Combined linear and non-linear refractive indices	$n_{effa} + n_2 I$
$w_L$	Input waveguide length	2 $\mu\text{m}$
$K_L$	Kerr element length	$\mu\text{m}$

Table 2.3 Dimensional and material properties of  $\text{Ta}_2\text{O}_5$  Kerr element used in the simulation of planar Kerr element. The dimensions of the rib waveguide ( $H$ ,  $D$ , &  $W$ ) used to calculate the effective indices of the inner rib region and outer slab region used in the Kerr lens simulations are in blue.

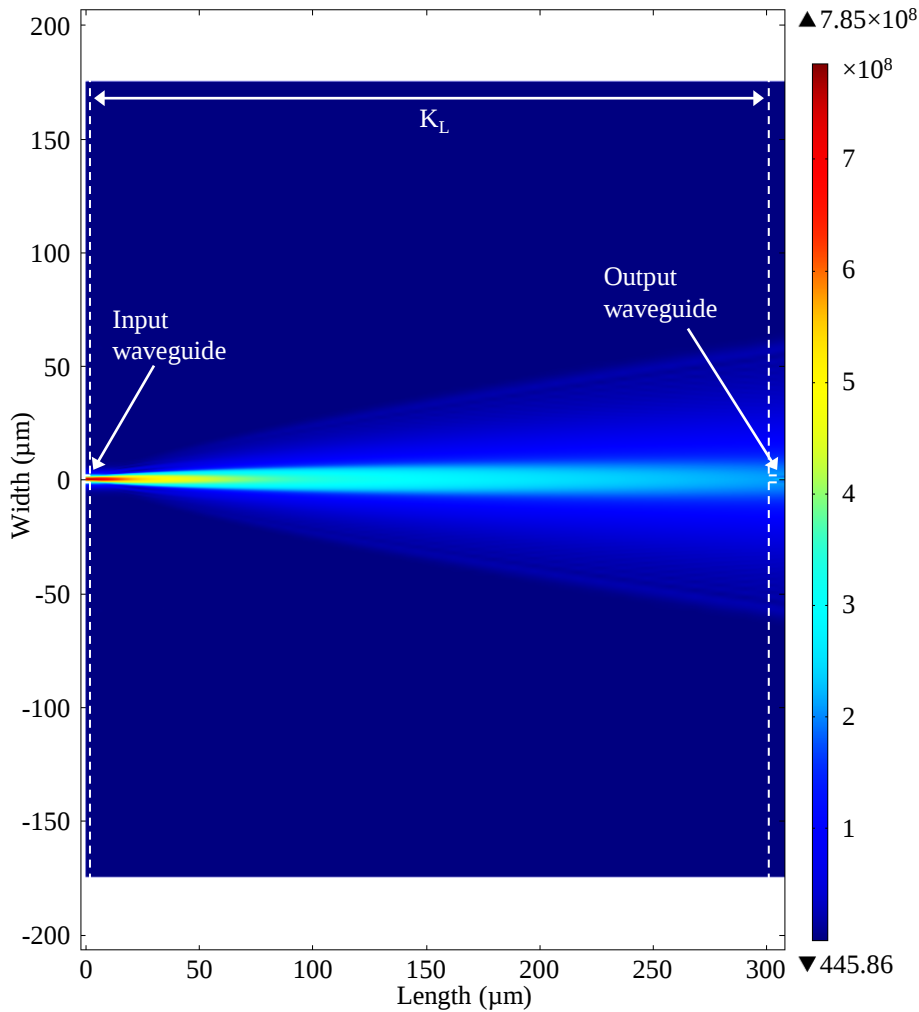


Figure 2.20 COMSOL electric field simulation of planar Kerr element showing the light diffracting within Kerr element. Dimensions of the model: input and output waveguide widths,  $W = 1 \mu\text{m}$  & Kerr element length,  $K_L = 300 \mu\text{m}$ . Input intensity,  $I = 1.5 \text{ GW}/\text{m}^2$ . White dotted lines highlight the boundary between outer slab regions and inner rib and Kerr element.

Figure 2.20 shows the COMSOL model of light propagating through the input waveguide (waveguide length,  $w_L = 2 \mu\text{m}$ ) and diffracting in the Kerr element with a length of  $300 \mu\text{m}$ . To analyse the effect of increasing the input intensity on the diffracting beam profile, a series of data cut lines across the simulation window in the  $y$  direction were made at various points along the direction of propagation ( $z$  axis) and was used to find the FWHM of the beam with respect to length of Kerr element. Figure 2.21 shows the effect increasing the intensity of the input beam has on the amount of diffraction occurring within the Kerr element. For an input intensity of  $1 \text{ W/m}^2$  for a propagating beam traveling along the open slab region, the width of the beam increases in a linear manner from an initial FWHM of  $1.4 \mu\text{m}$  ( $z = 0 \mu\text{m}$ ) to  $23.4 \mu\text{m}$  ( $z = 300 \mu\text{m}$ ) as it diffracts. The simulation showed that the FWHM of the propagating beam does not vary for intensities up to  $1 \text{ GW/m}^2$ , at which point as the input intensity is increased the beam begins to diffract less as the third-order non-linearity influence grows, causing the FWHM of beam's width to reduce. For an input intensity of  $6 \text{ GW/m}^2$  the FWHM of the diffracting beam was reduced by almost  $\approx 13 \mu\text{m}$  to a width of  $10.5 \mu\text{m}$ .

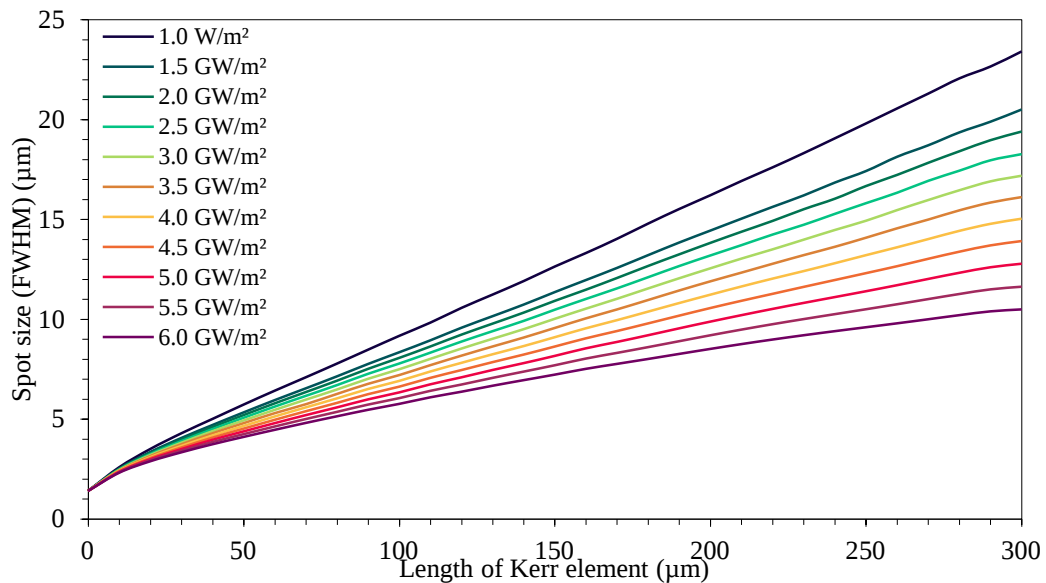


Figure 2.21 FWHM of the spot sizes in the  $y$  direction (horizontal direction of a rib waveguide cross-section) of the propagating along the Kerr element for various input intensities.

Figure 2.22 shows a comparison of the beam propagation along the Kerr element for input intensities of  $1.5 \text{ GW/m}^2$  and  $8 \text{ GW/m}^2$ . Figure 2.22a shows the light diffracting within the open slab region with an input intensity of  $1.5 \text{ GW/m}^2$  while figure 2.22b with an input intensity of  $8 \text{ GW/m}^2$  shows a visual difference as the beam begins to diffract less and focus the light. This can be seen with increase in intensity along the centre of the Kerr element.

A theoretical analysis of the amount of light propagating into the output collection waveguide as the Kerr element length was increase was carried out using a coupling efficiency analysis, introduced in Chapter 3. The theoretical analysis of the coupling efficiency showed an expected trend of the coupling efficiency decreasing as the output waveguide is moved further from the input

waveguide as a result of the length of the Kerr element increasing. This occurs as less of the light is launched into the output waveguide as beam's mode intensity profile is increase due to diffraction in the Kerr element. There is an initial coupling efficiency of 100% when  $K_L = 0$ , where there is no separation between the input and output waveguides, but as the length is increased the coupling efficiency drops in an exponential fashion to  $\approx 46\%$  at a distance of  $K_L = 50 \mu\text{m}$  for input intensity of  $1 \text{ W/m}^2$ . As seen in figure 2.21 increasing the input intensity beyond  $1 \text{ GW/m}^2$  causes the diffracting beam begins to focus, this in turn causes the coupling efficiency to increase to  $\approx 61\%$  at a distance of  $K_L = 50 \mu\text{m}$  for input intensity of  $6 \text{ GW/m}^2$ .

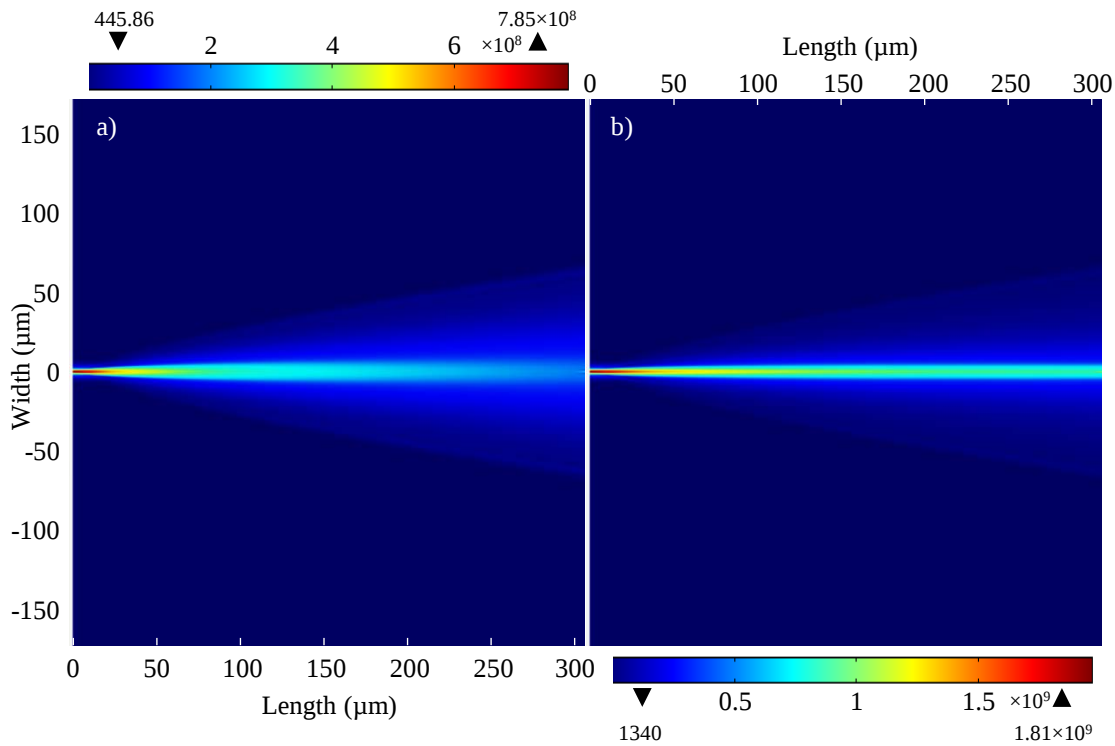


Figure 2.22 COMSOL electric field simulation of planar Kerr element showing self-focusing as input intensity is increased. The beam propagating along the Kerr element is shown for input intensities a)  $I = 1.5 \text{ GW/m}^2$ , & b)  $I = 8 \text{ GW/m}^2$ .

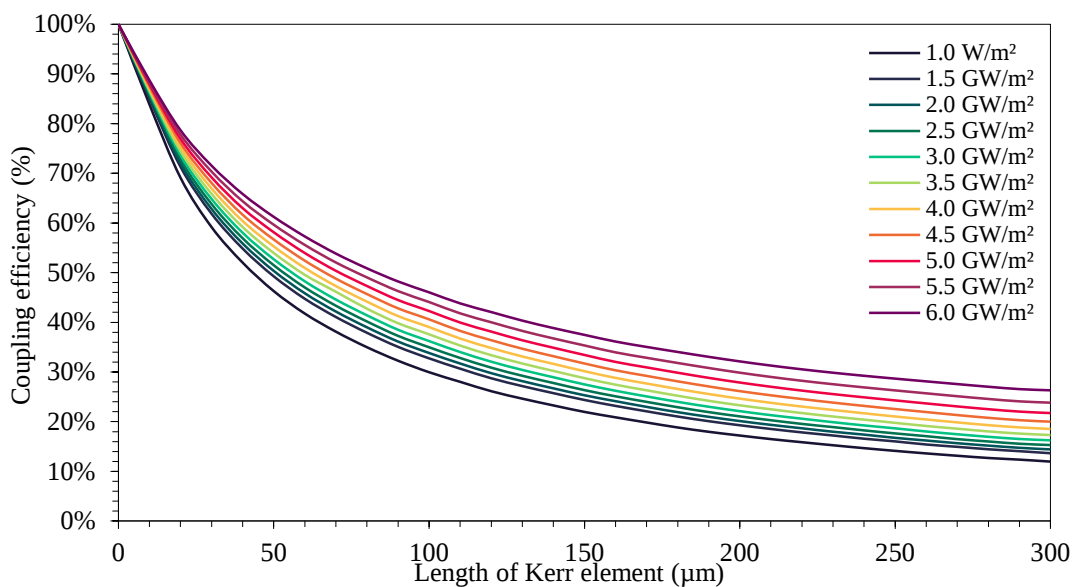


Figure 2.23 Coupling efficiency between input and output waveguides of the Kerr element as length ( $K_L$ ) is increased, for increasing input intensities.

The effect of the increasing the input intensity on the coupling efficiency can be seen more clearly in figure 2.24 when plotted against the input intensity for different slab lengths up to 300  $\mu\text{m}$ , at 20  $\mu\text{m}$  intervals. For longer lengths of the Kerr element, the amount of modulation of the coupling efficiency can be seen to be larger at higher intensity input power at almost  $\approx 11\%$  for input intensity of 6  $\text{GW}/\text{m}^2$  at  $K_L = 300 \mu\text{m}$ , but at the expense of a very low coupling efficiency with the highest reaching  $\approx 23\%$ . For shorter lengths of the Kerr element the modulation of the coupling efficiency is reduced to  $\approx 9\%$  for input intensity of 6  $\text{GW}/\text{m}^2$  at  $K_L = 20 \mu\text{m}$ , with the coupling efficiency reaching as high as  $\approx 79\%$ .

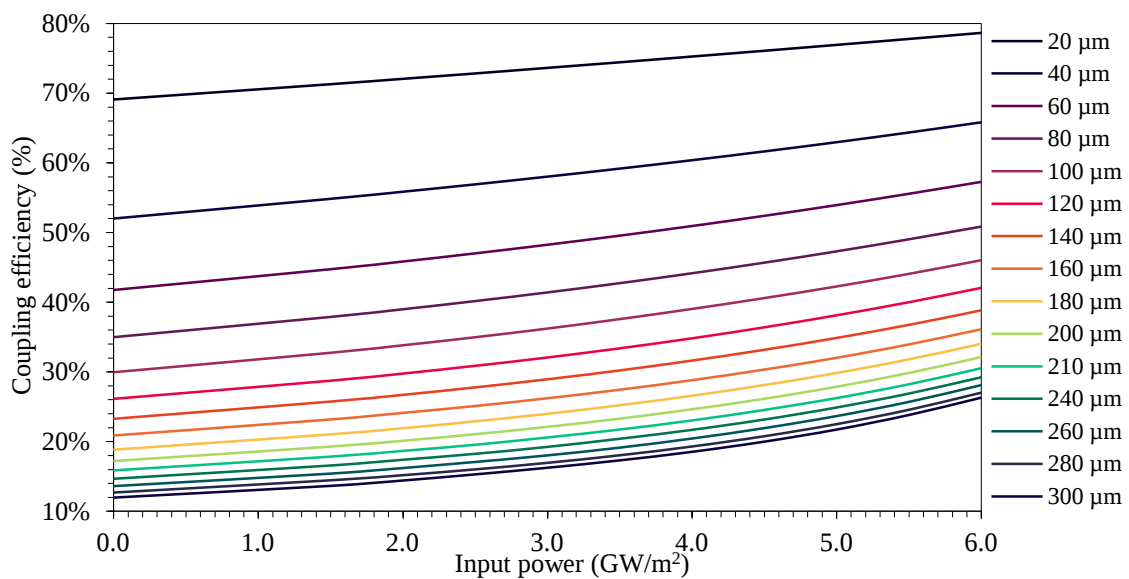


Figure 2.24 Coupling efficiency between input and output waveguides of the Kerr element as input intensity is increased, for different Kerr element lengths ( $K_L$ ).

From this study it is evident that an integrated Kerr lens element could be used in a planar waveguide laser cavity or ring resonator as a non-linear loss element for the generation of pulses. A modulation of  $\approx 9\%$  for the coupling efficiency can be achieved for a Kerr element 20  $\mu\text{m}$  long for powers from 1  $\text{W}/\text{m}^2$  to 6  $\text{GW}/\text{m}^2$  while keeping the non-saturable loss introduced by the element to 30%. As the length of the Kerr element is increased modulation of loss can be seen to increase but with the expense of increasing the loss of the element, potentially causing the suppression of lasing if inserted into a laser cavity. The non-saturable loss does not affect the formation and generation of an ultrashort pulse, while the non-linear element is saturated, but it can reduce significantly the efficiency of mode-locked laser system [21].

## 2.6 Conclusion

In this chapter, the fundamental optical waveguide theory is presented through basics of electromagnetic theory of light that lead to a set of normalised parameters based on a waveguide's

dimensional and material properties. These parameters are the basis of the discussed analysis methods such as effective index method and single mode guidance conditions which can be used as quick tools to predict the modal behaviour of a rib waveguide. For more comprehensive analysis of mode profile behaviour for different rib waveguides designs, simulations were carried out using COMSOL multi-physics finite element analysis software. Symmetrical Ta<sub>2</sub>O<sub>5</sub> rib waveguides with a core thickness of 1 μm and SiO<sub>2</sub> cladding was investigated for mode profiles propagating with a wavelength of  $\lambda = 980$  nm, as it is close to range of the operating wavelength of the laser pump source  $\approx 977$  nm as well as close to the expect wavelength of typical Yb-doped lasers. The simulations were implemented for rib etch depths of 150 nm, 300 nm, 500 nm, and full etch of 1 μm for rib widths from 0.3 μm to 20 μm. From the study it was found that for rib widths smaller than 1 μm the waveguide behaves as a slab waveguide with a thickness of the outer slab region (difference between thin film thickness and etch depth) with large mode intensity profiles in the horizontal directions. It was seen for all etch depths that as the rib width increases the mode intensity profile in the horizontal direction reaches a minimum near 1 μm width and then increases in a linear fashion. As there is an increase in the etch depth of the rib, the confinement of the mode intensity increases with the mode profile in the horizontal direction becoming smaller. From the study, tailoring mode profiles for desired applications within Ta<sub>2</sub>O<sub>5</sub> material can be achieved by selecting the corresponding etch depth and rib width. The feasibility of using a planar Kerr lens element as a passive loss modulator, that can be integrated with a CW waveguide laser to create a passive mode locked laser was also carried out. Kerr lens elements were designed with a rib waveguide with an inner film thickness of 1 μm, etch depth of 850 nm in Ta<sub>2</sub>O<sub>5</sub> material which propagated and launches light into an open slab region. The designed Kerr element was optimised to enhance the Kerr effect for self-focusing, and it was found that for longer Kerr element length ( $K_L$ ), the focusing of the diffracting beam became more apparent while shorter  $K_L$  the effect was less as the input intensity is increased. By tailoring the structure's dimensions and input intensity of the laser beam, the effect of the Kerr lens device can be specifically designed for required modulation depth, typically of a few percent, to cause modelocking.

## 2.7 Bibliography

- [1] E. Snitzer, "Proposed fiber cavities for optical masers," *J. Appl. Phys.*, vol. 32, no. 1, pp. 36–39, 1961.
- [2] E. Snitzer, "Optical maser action of Nd<sup>+3</sup> in a barium crown glass," *Phys. Rev. Lett.*, vol. 7, no. 12, pp. 444–446, 1961.
- [3] E. Lallier, "Rare-earth-doped glass and LiNbO<sub>3</sub> waveguide lasers and optical amplifiers," *Appl. Opt.*, vol. 31, no. 25, pp. 5276–5282, 1992.
- [4] J. I. Mackenzie, "Dielectric solid-state planar waveguide lasers: A review," *IEEE J. Sel. Top. Quantum Electron.*, vol. 13, no. 3, pp. 626–637, 2007.

- 
- [5] U. Keller, "Recent developments in compact ultrafast lasers," *Nature*, vol. 424, no. 6950, pp. 831–838, Aug. 2003.
- [6] A. Ghatak and K. Thyagarajan, *An introduction to fiber optics*. Cambridge University Press, 1998.
- [7] A. M. Weiner, *Ultrafast optics*. Hoboken, NJ, USA: John Wiley & Sons, Inc., 2009.
- [8] H. Kogelnik and V. Ramaswamy, "Scaling rules for thin-film optical waveguides," *Appl. Opt.*, vol. 13, no. 8, pp. 1857–1862, 1974.
- [9] H. Kogelnik, "Theory of dielectric waveguides," in *Integrated Optics*, T. Tamir, Ed. Springer Berlin Heidelberg, 1975, pp. 13–81.
- [10] O. Svelto, *Principles of Lasers*, 5th ed. Springer US, 2010.
- [11] R. A. Soref, J. Schmidtchen, and K. Petermann, "Large single-mode rib waveguides in GeSi-Si and Si-on-SiO<sub>2</sub>," *IEEE J. Quantum Electron.*, vol. 27, no. 8, pp. 1971–1974, 1991.
- [12] T. M. Benson, R. J. Bozeat, and P. C. Kendall, "Rigorous effective index method for semiconductor rib waveguides," *IEE Proceedings J Optoelectronics*, vol. 139, no. 1, p. 67, 1992.
- [13] P. Karasiński, C. Tyszkiewicz, R. Rogoziński, J. Jaglarz, and J. Mazur, "Optical rib waveguides based on sol-gel derived silica-titania films," *Thin Solid Films*, vol. 519, no. 16, pp. 5544–5551, 2011.
- [14] S. P. Chan, C. E. Png, S. T. Lim, G. T. Reed, and V. M. N. Passaro, "Single-mode and polarization-independent silicon-on-insulator waveguides with small cross section," *J. Light. Technol.*, vol. 23, no. 6, pp. 2103–2111, 2005.
- [15] V. Ramaswamy, "Strip-loaded film waveguide," *Bell Syst. Tech. J.*, vol. 53, pp. 697–704, 1974.
- [16] W. P. Risk, "Modeling of longitudinally pumped solid-state lasers exhibiting reabsorption losses," *J. Opt. Soc. Am. B*, vol. 5, no. 7, p. 1412, Jul. 1988.
- [17] W. F. Krupke, "Ytterbium solid-state lasers — the first decade," *IEEE J. Sel. Top. Quantum Electron.*, vol. 6, no. 6, pp. 1287–1296, 2000.
- [18] M. R. Paiam, C. F. Janz, R. I. MacDonald, and J. N. Broughton, "Compact planar 980/1550-nm wavelength multi/demultiplexer based on multimode interference," *IEEE Photonics Technol. Lett.*, vol. 7, no. 10, pp. 1180–1182, Oct. 1995.
- [19] A. Subramanian, "Tantalum pentoxide waveguide amplifier and laser for planar lightwave circuits," Ph.D. Thesis, University of Southampton, U.K., 2011.
- [20] G. Lifante, "Integrated photonics: Fundamentals," in *Integrated Photonics: Fundamentals*, Chichester, UK: John Wiley & Sons, Ltd, 2003, p. 198.
- [21] A. A. Lagatsky, C. G. Leburn, C. T. A. Brown, W. Sibbett, S. A. Zolotovskaya, and E. U. Rafailov, "Ultrashort-pulse lasers passively mode locked by quantum-dot-based saturable absorbers," *Prog. Quantum Electron.*, vol. 34, no. 1, pp. 1–45, Jan. 2010.

- [22] C.-Y. Tai, J. Wilkinson, N. Perney, M. Netti, F. Cattaneo, C. Finlayson, and J. Baumberg, "Determination of nonlinear refractive index in a Ta<sub>2</sub>O<sub>5</sub> rib waveguide using self-phase modulation.," *Opt. Express*, vol. 12, no. 21, pp. 5110–5116, 2004.

## CHAPTER 3

# Yb:Ta<sub>2</sub>O<sub>5</sub> Waveguide Fabrication and Characterisation

### 3.1 Introduction

Waveguide materials and processes that are compatible with silicon are strongly favoured for low-cost mass-manufacture. Silicon waveguides themselves are unsuitable for handling wavelengths below 1.1  $\mu\text{m}$  and exhibit two-photon absorption at wavelengths below 2  $\mu\text{m}$ , limiting their utility for pulsed and high-power applications in this range. This has led to CMOS-compatible dielectric waveguide systems such as silicon nitride [1], aluminium oxide [2] and tantalum pentoxide [3] being explored. Lasing in Er-doped [4] and Yb-doped [5] alumina and Nd-doped [6] and Er-doped [7] tantalum pentoxide have also been demonstrated.

In this chapter the fabrication process for the creation of Yb-doped Ta<sub>2</sub>O<sub>5</sub> waveguides is presented utilizing RF sputtering, photolithography and dry etch processes commonly used in CMOS fabrication [8]. Yb:Ta<sub>2</sub>O<sub>5</sub> films 1  $\mu\text{m}$  thick were deposited by RF magnetron sputter deposition onto a silicon substrate and shallow rib channels with an etch depth of 150 nm were created using a combination of photolithography and ion beam milling. The waveguides were encapsulated in thermally-grown silica under-cladding and RF magnetron sputtered silica over-cladding. In preparation for characterisation, waveguide chips 10.8 mm long were cut with the end-facets optically polished. Characterisation in the form of imaging of the mode intensity profiles were carried out, analysed in addition to propagation loss measurements by transmission measurements and Fabry-Perot propagation loss analysis.

### 3.2 Fabrication of Yb:Ta<sub>2</sub>O<sub>5</sub> rib waveguides

This section describes the multi-step fabrication process used to realise Yb:Ta<sub>2</sub>O<sub>5</sub> rib waveguides, drawing from CMOS-compatible fabrication technologies.

Channel waveguides in Yb-doped tantalum pentoxide were designed so that the pump and signal wavelengths are able to operate in single mode conditions at wavelengths between 970 nm and 1100 nm. The waveguides were designed to be fabricated on oxidised silicon wafers with an SiO<sub>2</sub>

under-cladding and thus have a high index contrast that makes tight turns possible. Also they were designed to have silica over-cladding for a symmetrical mode profile in order to facilitate in- and out-coupling.

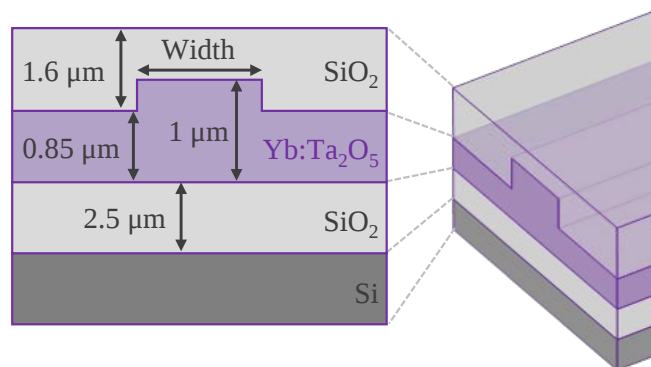


Figure 3.1 Partially etched rib waveguide structure with intended fabrication dimensions.

A partially etched rib waveguide approach, as introduced in Chapter 2 and illustrated by figure 3.1 was adopted to allow single mode operation of channels with widths readily fabricated using conventional photolithography, to maximise pump-signal overlap and to minimise waveguide loss due to sidewall roughness. The rib height was chosen to be 1  $\mu\text{m}$  to ensure good confinement of the modes within the core and the initial design was selected using Soref et al single mode guidance equation [9]. Simulations described in Chapter 2 showed that for rib widths with an etch depth greater than 500 nm, circular mode profile with maximum confinement light can be achieved but a compromise between modal spot size and loss due to sidewall roughness was made and an etch depth of 150 nm was chosen. While the film thickness and etch depth is kept constant as shown in figure 3.1, the width of the rib was varied between 1 to 10  $\mu\text{m}$ , increasing with increments of 0.2  $\mu\text{m}$ . With these constraints, waveguides with widths below  $w \leq 2.7 \mu\text{m}$  were predicted by COMSOL simulations to be single mode at a wavelength of  $\lambda = 980 \text{ nm}$ . The steps of the fabrication processes are listed below and described in more detail in this section.

1. Wafer preparation
2. Deposition of Yb:Ta<sub>2</sub>O<sub>5</sub> core layer
3. Annealing of substrate and core layer
4. Photolithography
5. Ion beam milling
6. Annealing of substrate and core layer
7. Potassium hydroxide treatment
8. Deposition of SiO<sub>2</sub> over cladding
9. Annealing of substrate with core and over clad layer
10. Dicing/Cleaving of wafer
11. Optical polishing of end-facets

### 3.2.1 Inspection and cleaning of substrate (Wafer preparation)

To ensure that the substrate is clean and pristine from unwanted artefacts before the fabrication process commences, a four inch wafer is inspected for any scratches or defects and is then cleaned to ensure a suitable surface for deposition.

A pre-clean process is initially carried out by washing the wafer in an ultrasonic bath with acetone for 20 minutes at room temperature. It is then immediately placed into another ultrasonic bath with Isopropyl alcohol (IPA) for a further 20 minutes at room temperature. After it is then thoroughly rinsed with de-ionized water and dried with compressed nitrogen.

The substrate is then cleaned using a piranha solution of three parts sulphuric acid and one part hydrogen peroxide to remove any organic contaminants [10]. The wafer is immersed in the piranha solution at room temperature for 20 minutes. The solution is mixed in parts to prevent too violent a reaction to begin with due to the high temperatures by the highly exothermic reaction. It is then thoroughly rinsed with de-ionized water and dried with compressed nitrogen.

To complete the preparation process the wafer is placed into an oven and it is baked at 120 °C to thoroughly dry the wafer ready for the first fabrication stage, the deposition of the core layer.

### 3.2.2 Yb:Ta<sub>2</sub>O<sub>5</sub> core layer

This section of the chapter details the fabrication of Yb:Ta<sub>2</sub>O<sub>5</sub> rib waveguides, beginning with the deposition of a Yb:Ta<sub>2</sub>O<sub>5</sub> thin film, and then leads onto how the rib structure is produced in the film layer.

#### 3.2.2.1 *Deposition of Yb:Ta<sub>2</sub>O<sub>5</sub> thin film*

Sputtering is a common deposition process used in the semiconductor industry to deposit thin film layers of material onto a desired substrate. It involves displacing material from a solid “target” that contains the required material through bombardment of atoms or ions which causes the ejected atoms to deposit onto the substrate. A typical RF sputtering chamber is illustrated in figure 3.2.

A 1 μm thick Yb:Ta<sub>2</sub>O<sub>5</sub> film was deposited by RF magnetron sputter deposition from a powder-pressed Yb:Ta<sub>2</sub>O<sub>5</sub> target doped with 2.5 wt.% of ytterbium oxide ( $\approx 6.2 \times 10^{20}$  Yb atoms/cm<sup>3</sup>) onto a four inch silicon substrate with a 2.5 μm thick thermally-grown silica layer. This ytterbium concentration was selected as an initial starting point based upon Yb<sup>3+</sup>:Al<sub>2</sub>O<sub>3</sub> channel waveguide by Bernhardt et al. [5] which showed single mode operation with a slope efficiency of 67%, emitting at 1021.2 nm while optically pumped at 976 nm. The deposition was performed in a vacuum chamber which had been pumped to a base pressure of 10<sup>-8</sup> Torr and then backfilled with a mixture of argon and oxygen. The sputtering system used was an Oxford Instruments Plasma Technology

(OPT) Plasmalab 400+. To deposit the desired film layer thickness, a series of test runs were carried out to establish a deposition rate by sputtering Ta<sub>2</sub>O<sub>5</sub> onto a sacrificial substrate.

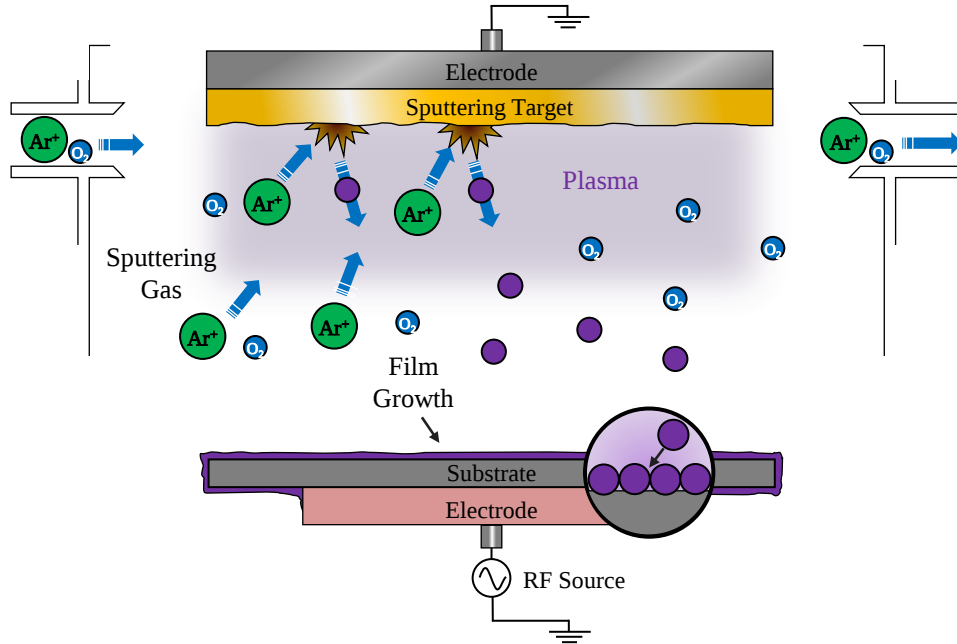


Figure 3.2 RF sputtering process for thin film material deposition

The sacrificial substrate had regions where the deposited film was not sputtered onto and using KLA Tencor P-16 stylus profiler the film thickness was measured with respect to the unsputtered regions. The estimated deposition rate for Yb:Ta<sub>2</sub>O<sub>5</sub> was based upon conditions previously found for Er:Ta<sub>2</sub>O<sub>5</sub> shown in table 1 [11]. The study was carried out to optimise optical losses of Er:Ta<sub>2</sub>O<sub>5</sub> thin film with an acceptable deposition rate by investigating the propagation losses at 633 nm by varying the sputtering temperature, argon and oxygen flow rate, and magnetron power. The deposition rate for Yb:Ta<sub>2</sub>O<sub>5</sub> was calculated from a series of test runs to be  $1.8 \pm 0.1$  nm/minute therefore for the desired thickness Yb:Ta<sub>2</sub>O<sub>5</sub> of 1  $\mu\text{m}$  the sputtering process ran for 9 hours and 50 minutes.

Setting	Units
Argon (Ar)	20 sccm
Oxygen (O <sub>2</sub> )	5 sccm
Power	300 W
Deposition pressure	10 m $\tau$
Static direct coupled plasma (DCP) temperature	200 $^{\circ}\text{C}$

Table 3.1 Sputtering chamber conditions for Yb:Ta<sub>2</sub>O<sub>5</sub> deposition.

### 3.2.2.2 Annealing

After the deposition of Yb:Ta<sub>2</sub>O<sub>5</sub> thin film, the wafer was then placed into a Severn (STS) 1200  $^{\circ}\text{C}$  tube furnace for the annealing process. Annealing is a procedure developed to relieve any residual stresses caused during the cooling of the glass after the layer had been formed. These stresses in the glass can cause a substantial decrease in the strength of the Yb:Ta<sub>2</sub>O<sub>5</sub> layer. As well as reducing the stress presented in the layer it also serves to reduce oxygen deficiency introduced during the

sputtering and etching processes [12]. This is important as the deficiency of oxygen can lead to significant losses through absorption. The process composes of heating the glass sample to its corresponding annealing point, then letting to cool slowly enough so that the outer and inner sections of the sample cool at the same rate therefore reducing the stresses of throughout the layered glass. The annealing process is described below

1. Load sample into furnace at room temperature (21 °C)
2. Increase the temperature of the furnace to 600 °C at a rate of 3 °C/minutes
3. The sample then dwells in the furnace for 2 hours
4. Cool the temperature of the furnace back room temperature at a rate of 2 °C/minutes

### *3.2.2.3 Photolithography*

A common micro-fabrication technique used to generate the waveguide designs on the Yb:Ta<sub>2</sub>O<sub>5</sub> layer is photolithography. Photolithography is a process of imprinting geometric shapes onto a light sensitive material called photoresist, which is layered on the film to be patterned. These geometric shapes are transferred by means of ultraviolet (UV) light from a photomask onto the photoresist to allow for further processing of the substrate [13].

The photoresist used is the MICROPOSIT S1813<sup>TM</sup> G2, a positive photoresist which becomes soluble to photoresist developer in the regions exposed by UV light. The procedure used for preparing and implementing photolithography is shown in figure 3.3 with full process described below:

1. The wafer has a thin layer of photoresist spin coated at 5000 rpm on top of the Yb:Ta<sub>2</sub>O<sub>5</sub> layer giving an approximate uniform thickness of  $\approx 1.3 \mu\text{m}$ .
2. The wafer is soft baked to get remove excess solvent within the photoresist in an oven at 96 °C for 30 minutes.
3. Next the mask is aligned with the target wafer and pressed into contact against it.
4. Once the alignment is complete the photoresist is exposed to UV light radiation.
5. The photoresist is then placed into a development solution (MICROPOSIT<sup>TM</sup> MF-319 developer) for a duration lasting between 45 to 50 seconds. Once the photoresist is taken out of the developer solution it is rinsed with de-ionized water and dried with compressed nitrogen.
6. The remaining photoresist left after developed is then hard baked for 30 minutes at 120 °C to solidify the layer.

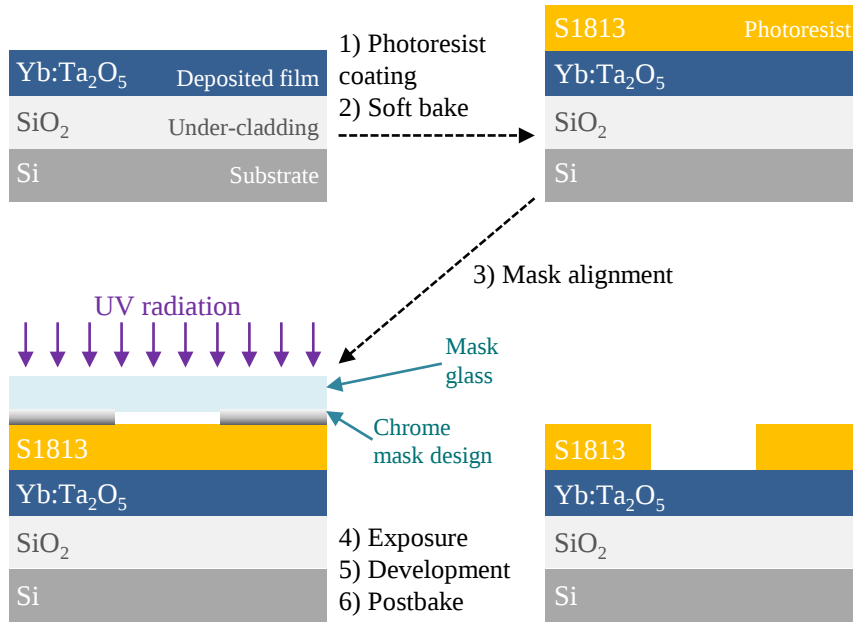


Figure 3.3 2D cross sectional presentation of photolithography process.

#### 3.2.2.4 Etching process

Rib waveguides in Yb:Ta<sub>2</sub>O<sub>5</sub> were realized by dry etching of unprotected thin films. Argon ion beam milling process, an anisotropic dry etching technique was used in the removal of thin films. An Oxford Instruments Plasma Technology (OPT) Ionfab 300 plus ion beam etch and deposition system was used to realise the Yb:Ta<sub>2</sub>O<sub>5</sub> rib waveguides with an etch depth of 150 nm.

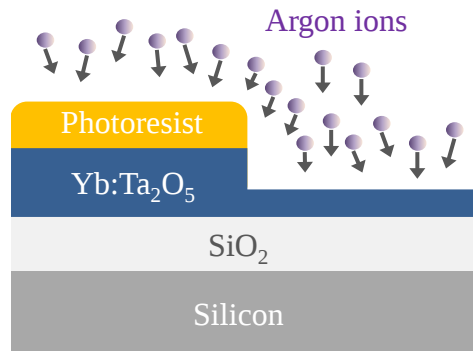


Figure 3.4 Argon ions attacking the unprotected areas of Yb:Ta<sub>2</sub>O<sub>5</sub>.

The wafer was placed into the Ionfab 300+ and was etched for 5 minutes as an initial test for calculating the etching rate of the system. After 5 minutes of etching, a comparison was made of the heights of an etched section of Yb:Ta<sub>2</sub>O<sub>5</sub> and an unetched section of Yb:Ta<sub>2</sub>O<sub>5</sub>. Using the KLA Tencor P-16 stylus profiler it was determined that  $95 \pm 2$  nm of Yb:Ta<sub>2</sub>O<sub>5</sub> was etched within the 5 minute period giving an etch rate of  $0.32 \pm 0.02$  nm s<sup>-1</sup>. For the remaining 55 nm of required etching (in total 150 nm required), it was calculated that the ion beam miller would need to etch for a further 2 minutes and 54 seconds. The total etching time was 7 minutes and 54 seconds.

After the etching process was complete the excess photoresist was removed as described below:

1. The wafer was placed in Acetone for 20 minute then taken out and rinsed with Acetone, IPA and de-ionized water, then dried with compressed nitrogen.
2. Further resist was taken off by using the OPT Plasmalab 80+ reactive ion etcher to perform plasma ashing, a semiconductor manufacturing method for removal of undesired photoresist. The duration of the plasma ashing process was two minutes, in an oxygen environment within the reactive ion etcher chamber.
3. To further clean any small left over pieces of photoresist the wafer was finally cleaned in an ultrasonic bath of Acetone.

Once the photoresist was removed the wafer was treated with an aqueous potassium hydroxide (KOH) solution to reduce any surface roughness. The wafer was placed in a 30% KOH solution at a temperature of 55 °C for 20 minutes [14].

### 3.2.3 Silica over clad layer

A 1.6  $\mu\text{m}$  over-cladding layer is deposited on top of the Yb:Ta<sub>2</sub>O<sub>5</sub> layer to encapsulate the waveguide structures. The deposition process used the same sputtering system as that used for the deposition of the Yb:Ta<sub>2</sub>O<sub>5</sub> layer.

#### 3.2.3.1 Deposition of SiO<sub>2</sub> thin film

The over-cladding was deposited for 12 hours 29 minutes with a deposition rate of  $2.14 \pm 0.05$  nm/min to provide the 1.6  $\mu\text{m}$  thin film layer. The conditions used during the deposition of SiO<sub>2</sub> are shown in table 3.2.

Setting	Units
Argon (Ar)	20 sccm
Oxygen (O <sub>2</sub> )	5 sccm
Power	300 W
Deposition pressure	10 m $\tau$
Static direct coupled plasma (DCP) temperature	20 °C

Table 3.2 Sputtering chamber conditions for SiO<sub>2</sub> deposition.

The wafer was annealed further after the final sputtering stage using the same process described in section 3.2.2.2.

### 3.2.4 Dicing and optical polishing of end-facets

Using a BUEHLER IsoMET5000 linear precision dicing saw, the four inch wafer was cut into single rectangular pieces for each individual group of waveguides. After the wafer was diced the end surfaces of the individual devices were polished, to reduce insertion scattering losses that could affect the overall function of the waveguides. The end surfaces were polished using a Logitech LP50 lapping and polishing station.

The process for polishing the end surfaces was split into three stages and is described below

1. Lapping stage 1: Waveguide end-facet is swept across a cast iron lapping plate doused with 9  $\mu\text{m}$  aluminium oxide ( $\text{Al}_2\text{O}_3$ ) slurry. This stage is for rapid removal of  $\text{Yb:Ta}_2\text{O}_5$  aimed to reduce the rough and chipped end-facet caused from dicing.
2. Lapping stage 2: Waveguide end-facet is then swept across the same cast iron lapping plate but is now doused with 3  $\mu\text{m}$  aluminium oxide ( $\text{Al}_2\text{O}_3$ ) slurry. This stage is for the further reduction of surface scratches and chips caused from the 9  $\mu\text{m}$   $\text{Al}_2\text{O}_3$  slurry lapping phase.
3. Polishing stage: Waveguide end-facet was finally swept across a polyurethane polishing plate doused with alkaline colloidal silica (Logitech Syton SF1 polishing slurry) which is used to create smooth polished quality.

### 3.2.5 Fabrication results

The end polished facet of the fabricated devices was imaged using a scanning electron microscope (SEM) to examine the cross-sectional shape of the rib-waveguide. To image an object in a SEM it must be electrically conductive and electrically grounded to prevent the accumulation of electrostatic charge at the surface. Due to the non-conductive nature of the waveguide sample a SEM sample preparation is required, firstly by mounting the sample onto a conductive stub, then a 10 nm layer of gold is sputter coated to create an electrically conductive surface grounded through the stub. Figure 3.5 shows the SEM cross-section image of a fabricated  $\approx 5 \mu\text{m}$  wide waveguide.

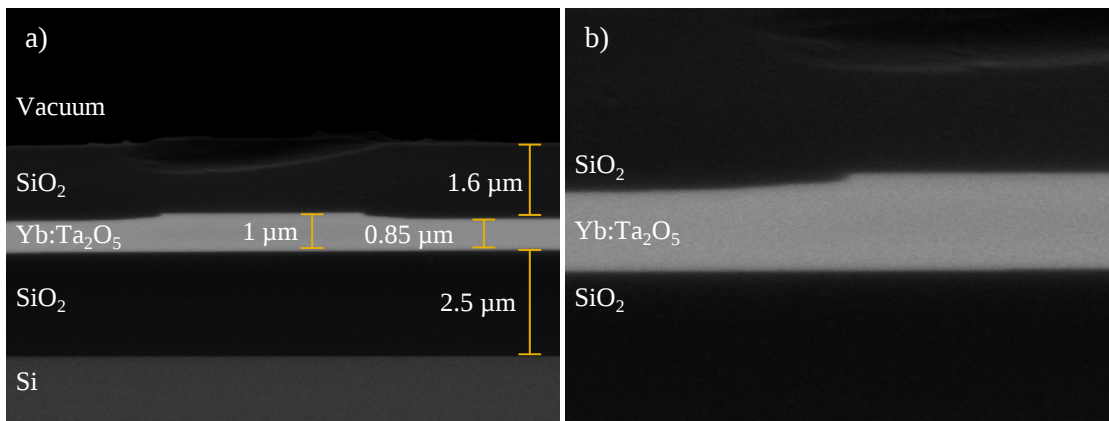


Figure 3.5 Enhanced SEM cross-section image of fabricated  $\approx 5 \mu\text{m}$  wide waveguide, a) showing the different layers of thin film material, b) zoomed in section highlighting the double sloped side wall.

From the SEM images of the cross-section of the rib waveguide, four different regions of material are evident: the silicon substrate, the silica over-cladding and under layer, and the Yb-doped tantalum pentoxide layer. The thickness of the deposited  $\text{Yb:Ta}_2\text{O}_5$  layer was  $1 \pm 0.03 \mu\text{m}$ , measured from the inner rib waveguide height and the outer slab region produced by etching was  $0.85 \pm 0.03 \mu\text{m}$ . The  $\text{SiO}_2$  buffer layer has a thickness of  $2.5 \pm 0.08 \mu\text{m}$  and the deposited over-cladding had a thickness of  $1.6 \pm 0.05 \mu\text{m}$ . The rib waveguide structure can be seen but inner rib region side walls are not completely vertical with a double slope effect apparent, seen in figure 3.5b. The initial slope has a pitch of approximately  $53^\circ$  with the next connecting slope levelling out with the waveguide's outer slab region with an angle of  $5^\circ$ . The sloped side wall etching

phenomena is known as faceting and occurs as a consequence of curved corners of the photoresist after development, causing an increased etch rate at the corners of the photoresist mask compared to the rest of the mask. This increase in the etch rate at the corners of the mask causing faceting arises because the etch rate for targeted material is a function of angle of the etchant beam perpendicular the surface [15]. The sloped masked edges then lead to the etching of the thin films with sloped edges. The measurements of the different layers from the SEM imaging verify that deposition of thin film layers are achieved close to the intended thicknesses and that the fabrication process is able to deposit and etch the desired heights. The widths of the waveguides were measured using a calibrated Nikon LV100D optical microscope and confirmed using the SEM. For widths of 1  $\mu\text{m}$  there was a 14% variation of the measured waveguide to the intended size while for wider rib widths the variation was 1%. This large variation seen for 1  $\mu\text{m}$  can be as a result of under-exposure of UV light during photolithography which affects small width waveguides more than wider widths.

### 3.3 Mode profile simulation of sloped edge rib waveguides

The effect on the fundamental mode intensity profile of the mode propagating within a sloped side wall waveguide was investigated through simulations using COMSOL, and compared against straight wall rib waveguides simulations. The cross-sections of these waveguides are illustrated in figure 3.6. Established during the SEM inspection of the waveguides end-facet side walls with an initial slope of 53°, followed by a slope of 5° was built into the previous COMSOL model and simulated with the same conditions describe in section 2.4. The resulting mode intensity profiles were analysed to give spot sizes at FWHM for various rib widths, while the angle of the slopes were kept constant. The electric field distribution for the fundamental mode of a rib waveguide with width of 1  $\mu\text{m}$ , a thickness of 1  $\mu\text{m}$  and an outer slab region of 850 nm thickness for both the sloped and straight side wall designs are shown in figure 3.7a and figure 3.7c, respectively. The mode intensity distributions through the position of peak intensity in the horizontal and vertical directions are also shown in figure 3.7b and figure 3.7d, respectively.

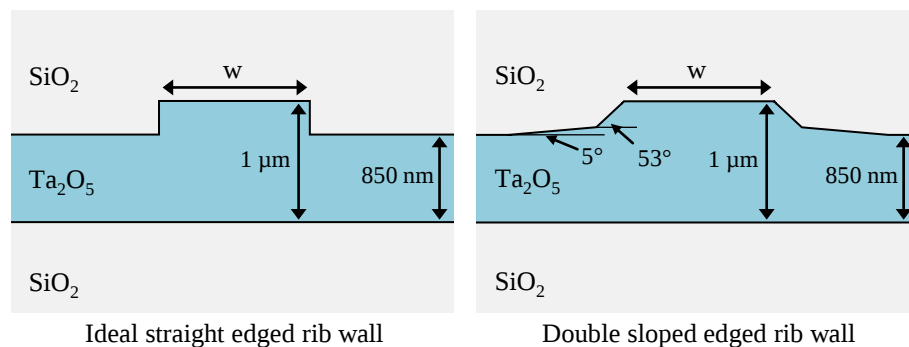


Figure 3.6 Cross-section of the ideal straight edged rib waveguide and the sloped fabricated rib waveguide.

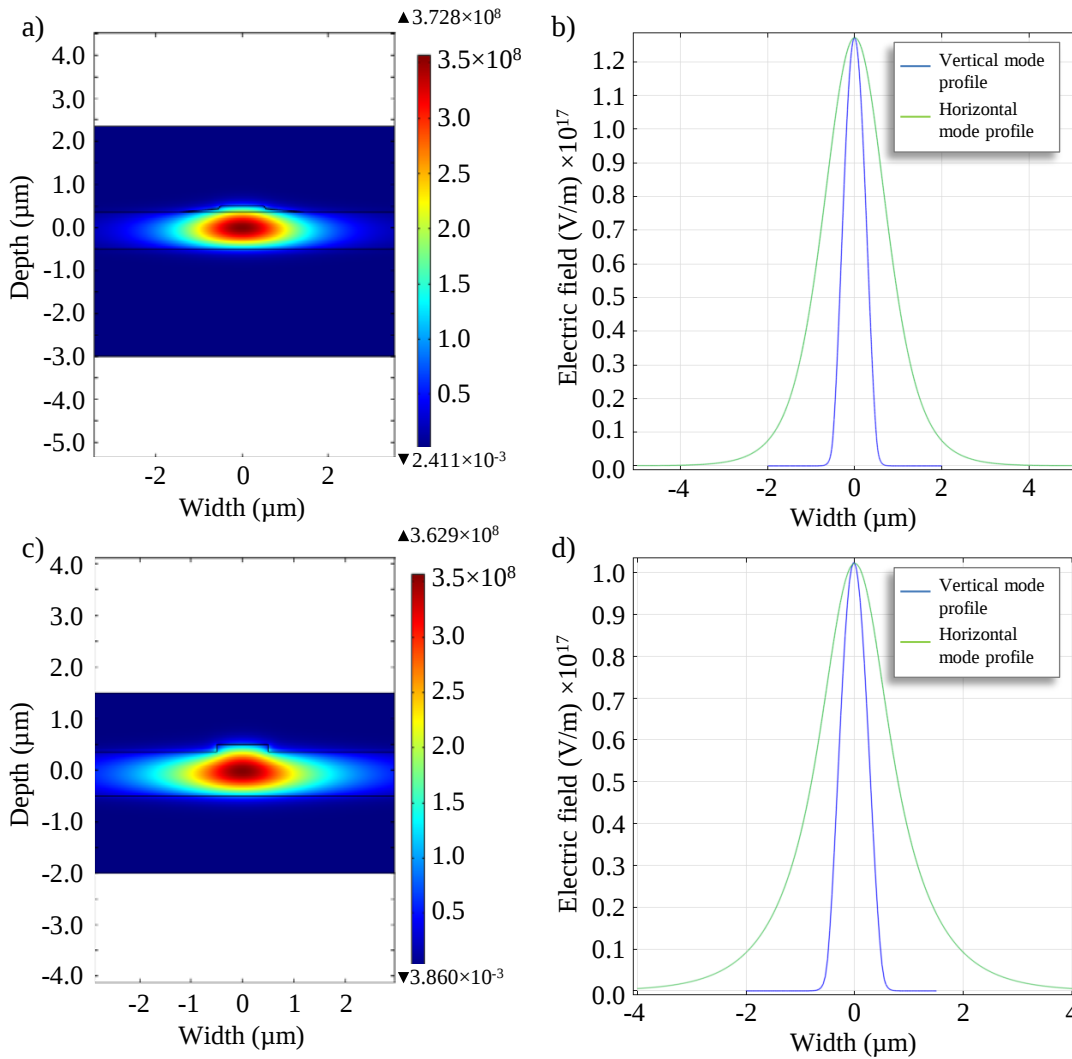


Figure 3.7 COMSOL simulation of the electric field of the fundamental mode of a rib waveguide with an etch depth of 150 nm for a rib width of 1  $\mu\text{m}$ : a) sloped edge rib waveguide; c) straight edge rib waveguide & COMSOL simulation of the mode intensity profiles for the fundamental mode in the horizontal and vertical directions for a rib waveguide with an etch depth of 150 nm for a rib width of 1  $\mu\text{m}$ : b) sloped edged rib waveguide; d) straight edge rib waveguide.

The FWHM of spot sizes of the fundamental for rib widths between 0.3 – 10  $\mu\text{m}$  for straight and sloped edged walls is shown in figure 3.8. In the horizontal direction for rib widths below 0.7  $\mu\text{m}$  the straight rib is unable to support modes as the waveguide has an effective index close to the outer slab region, with confinement occurring only in the vertical dimension. The introduction of sloped edges changes the dimensional cross-section which increases effective index of the waveguide leading to confinement in both the horizontal and vertical dimension. As the width of the rib increases beyond 1  $\mu\text{m}$  the sloped edged walls in the horizontal direction increases linearly, but exhibits a larger spot size compared to straight edge waveguides counterpart. This increase of the sloped wall spot sizes varies depending on the width of the waveguide with percentage increase from 7% to 12% for widths 1  $\mu\text{m}$  to 2  $\mu\text{m}$ . Widths greater than 2  $\mu\text{m}$  the percentage difference gradually decreases to a 4% increase for a width of 10  $\mu\text{m}$ . This is due to mode intensity profile being confined in a larger rib area caused by increase in dimension by the sloped sides. In the vertical direction the spot sizes are the same for different rib widths as expected as the height of the

core does not change and in comparison with the straight edge there is an increase in the spot size of less than 0.5%.

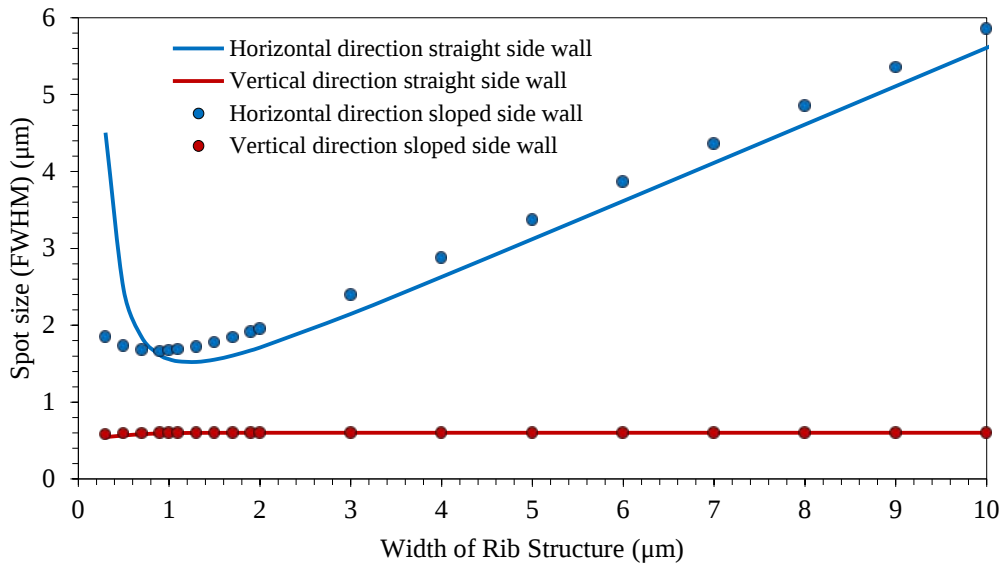


Figure 3.8 Comparison between straight and sloped side walls simulated FWHM mode intensity profiles at 980 nm.

Comparison between the effective indices for the ideal case and for simulations of the waveguide with sloped walls as fabricated is shown in figure 3.9. For rib widths up to 1  $\mu\text{m}$  a difference of 0.002 is seen for effective indices but as the rib width increases this difference is reduced and both effective indices tend to the slab waveguide effective index 2.8045 as expected.

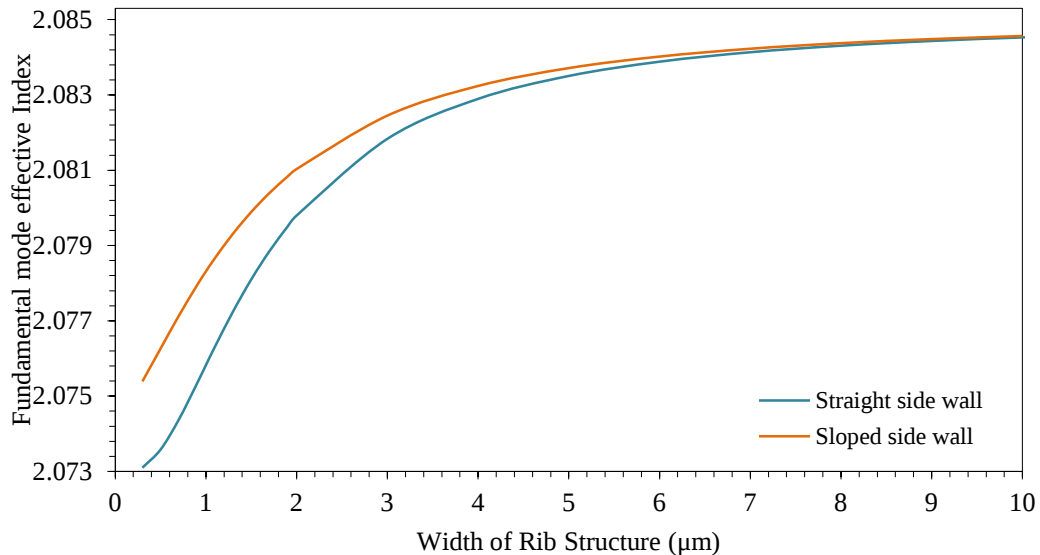


Figure 3.9 Comparison between straight and sloped side walls simulated effective indices at 980 nm.

### 3.4 Characterisation and analysis of mode intensity profiles

This section presents the experimental procedure used to characterise the modal intensity profiles of  $\text{Yb:Ta}_2\text{O}_5$  rib waveguides and plots the experimentally acquired mode intensity profiles so that the FWHM of the spot sizes could be quantified.

A schematic diagram of the experimental approach to characterize the mode intensity profiles of the rib waveguide structures is shown in figure 3.10. The input radiation was supplied by a 977 nm fibre Bragg grating stabilised pump laser, which was focused and coupled into a waveguide through one of the end-facets using a 40x objective lens in free space. The modal intensity profile of the waveguide mode was then imaged with Hamamatsu C2741-03 CCD using a 40x objective lens to expand the output image onto a larger area of the CCD sensor.

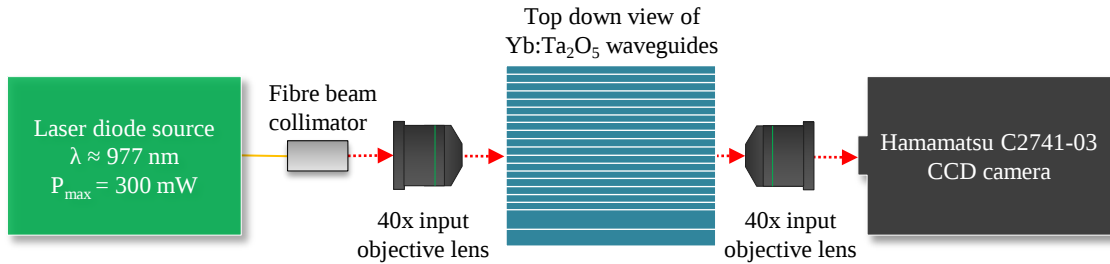


Figure 3.10 Free space set-up of Yb:Ta<sub>2</sub>O<sub>5</sub> waveguide modal profile characterization.

An example of a mode intensity profile of a 1  $\mu\text{m}$  wide rib waveguide captured by the CCD camera is shown in figure 3.11. The waveguides were imaged for ribs widths up to 7  $\mu\text{m}$  as it was evident from the images and mode intensity profiles that the rib waveguides were multi-mode for widths greater than 4  $\mu\text{m}$ . The mode profiles captured by the CCD camera for various rib widths were then analysed in Matlab to find the FWHM height and width of the modal field. To ascertain the correct data points for plotting the modal profile intensities, the pixel corresponding to the highest intensity peak was selected. The column and row of data that intersected this pixel were then plotted as shown in figure 3.12. These data were then used to calculate the FWHM spot size of the mode intensity profile.

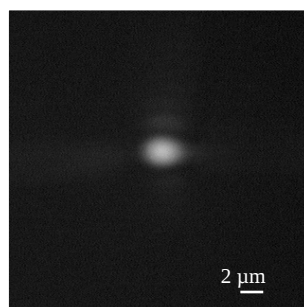


Figure 3.11 Mode intensity profile of rib waveguide with a width of 1  $\mu\text{m}$ , captured with camera.

The FWHM spot size determined from the mode profiles were converted from pixels to physical length by calculating the spatial scale of the imaging system. This was achieved by translating a mode intensity profile across the camera by moving the output objective lens by a set distance. Then by comparing the peaks of mode intensity profiles seen by the camera before and after the translation of the lens the number pixels covered in that distance was recovered. A spatial scale of 86.2 nm per pixel along both the horizontal and vertical was determined.

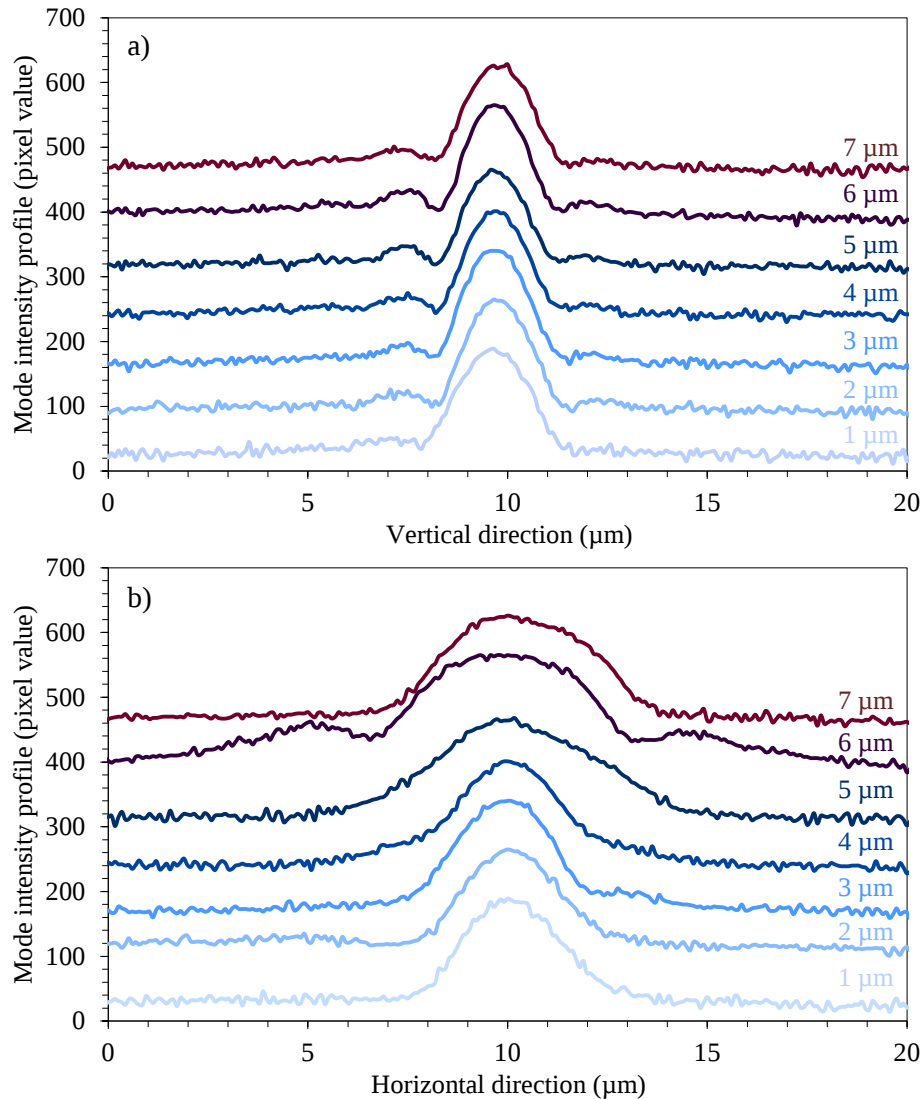


Figure 3.12 Mode intensity profiles in a) vertical and b) horizontal directions for various rib widths.

The mode intensity profiles in the vertical direction for the fabricated rib structure can be seen in figure 3.12a, where each line is offset by 75 pixels for clarity. It can be seen that the vertical profiles are very similar in shape and size, which is expected because the inner core height is not varied for each waveguide. The FWHM of the spot sizes in the vertical direction are larger than simulated fundamental modes, with the measured FWHM of  $2.1 \pm 0.3 \mu\text{m}$ . From the horizontal mode intensity profiles shown in figure 3.12b, for rib widths between  $1 \mu\text{m}$  and  $4 \mu\text{m}$  the mode profiles are very similar in size and show the fundamental modes in these waveguides which were found to be single mode. The FWHM of the spot sizes for these waveguides in the horizontal direction are  $3.15 \pm 0.1 \mu\text{m}$ . As the size of the rib increases to width of  $5 \mu\text{m}$ ,  $6 \mu\text{m}$  and  $7 \mu\text{m}$ , the profiles move away from a near-Gaussian profile to a profile, which shows characteristics found in multimode propagation, which is indicated by the shapes of mode profiles in figure 3.12b.

The images of the light at the output of the fabricated rib waveguides were acquired experimentally to estimate the FWHM of the spot sizes via a comparison made with the simulated mode intensity

profiles, but the image profiling method has been shown to include a method with a large measurement error. The experimentally extrapolated mode profiles in the vertical direction agrees partly with the simulation results as the profile does not change with increase in channel width but shows a larger spot size than the simulation results by  $1.5 \mu\text{m}$  for each mode intensity profile. A possible root of the error stems from the increase in FWHM due to the image of the mode profile appearing larger because of the spreading of the actual mode profiles in both the vertical and horizontal directions. This occurrence is known as the point spread function (PSF) [16] and involves the convolution of the imaged real object with the PSF. Therefore simulation results are used for calculations within this work which require the mode intensity profile of the rib waveguide.

### 3.5 Optical loss measurements

In this section the methods used to characterise optical losses of the fabricated  $\text{Yb:Ta}_2\text{O}_5$  rib waveguides are described. Two non-destructive methods were used for the determination of the propagation losses; firstly by measuring the transmission of radiation propagating within the channel at a wavelength of  $1064 \text{ nm}$ , where ytterbium ion absorption is relatively weak; and secondly using the Fabry-Perot (FP) propagation loss analysis.

#### 3.5.1 Transmission measurements at $1064 \text{ nm}$

The transmission measurements were carried out using a  $1064 \text{ nm}$  LD source with a polarisation maintaining pig-tailed fibre (PM980-HP), with the experimental set-up shown in figure 3.13. To emulate the launch conditions of the set-ups used for spectroscopic characterisation of the  $\text{Yb:Ta}_2\text{O}_5$  rib waveguides, an identical SM fibre (HI1060) used by  $977 \text{ nm}$  LD source was spliced onto the PM fibre. TM polarized light was launched into end-facet of the waveguide through butt-coupling using the SM fibre. The light coupled out of the waveguide's end-facet was collected using a multi-mode fibre and fed into a germanium photo-detector (Newport 918-IR).

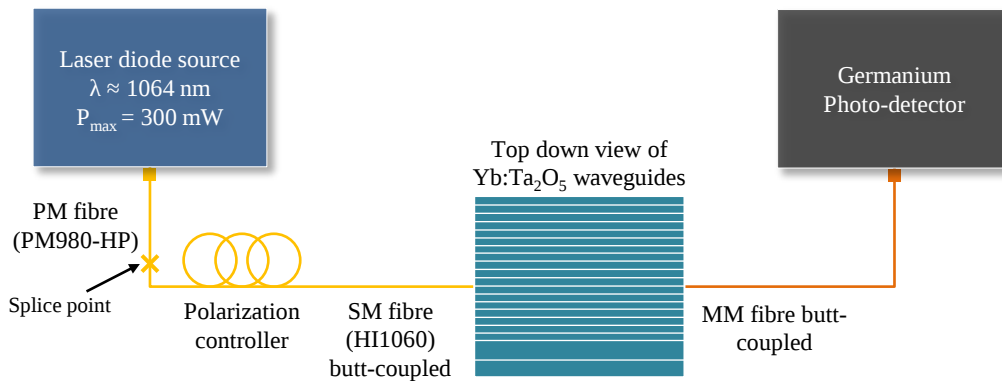


Figure 3.13 Experimental set-up for transmission loss measurement at  $1064 \text{ nm}$ .

### 3.5.1.1 Coupling efficiency theory

In this section the theory for the coupling efficiency calculation used within this work to estimate the amount of light coupled into the end-facet of the waveguide is introduced and used to calculate the amount of 1064 nm wavelength light launched into different width rib channel waveguides.

The coupling between the laser diode pig-tailed fibre and the waveguide is calculated from the electromagnetic fields, where the dimensions are known through the simulations of the mode intensity profiles of the rib waveguide and the FWHM mode field diameter of the fibre. The principles behind calculating the amount of light launched into the waveguide begins with a Gaussian beam approximation to describe the fields of the laser beam and waveguide's fundamental mode by considering two independent waist parameters for the laser and waveguide.

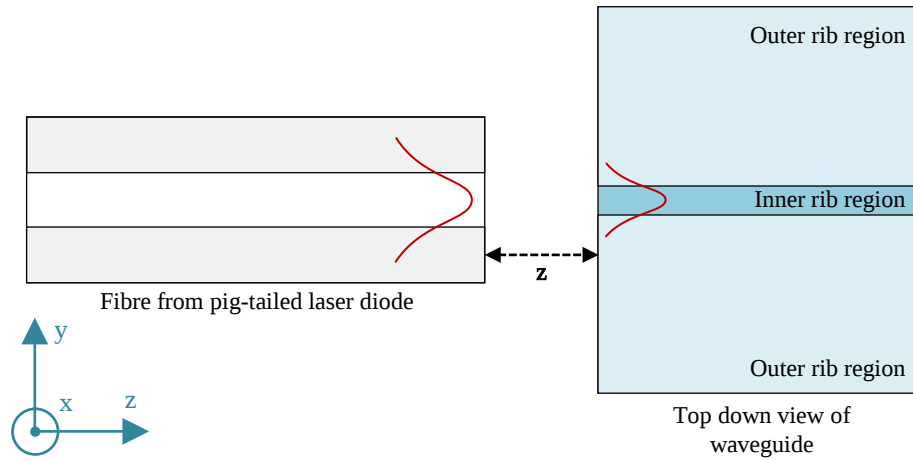


Figure 3.14 Illustration of top down view of laser diode pig-tailed fibre launching laser light into a Yb:Ta<sub>2</sub>O<sub>5</sub> rib waveguide.

An integration of the electric fields of the laser field and waveguide fundamental mode leads to a coupling efficiency,  $\eta$  is described by [17]

$$\eta = \frac{\eta_x}{\sqrt{1 + \gamma_x}} \frac{\eta_y}{\sqrt{1 + \gamma_y}} \quad (3.1)$$

where  $\eta_x$ ,  $\eta_y$ ,  $\gamma_x$ , and  $\gamma_y$  are expressed as

$$\eta_x = \frac{2w_x w_{Gx}}{w_x^2 + w_{Gx}^2} \quad (3.2)$$

$$\gamma_x = \left[ \frac{k}{4R_x} w_x w_{Gx} \eta_x \right]^2 \quad (3.3)$$

$$\eta_y = \frac{2w_y w_{Gy}}{w_y^2 + w_{Gy}^2} \quad (3.4)$$

$$\gamma_y = \left[ \frac{k}{4R_y} w_y w_{Gy} \eta_y \right]^2 \quad (3.5)$$

Here  $w_{Gx}$  and  $w_{Gy}$  are the electric field's FWHM of the waists of the waveguide's fundamental mode in the x and y direction, and  $w_{lx}$  and  $w_{ly}$  are the electric field's FWHM of the waists of the pump beam in the x and y direction. The pump beam waist is described below by equations defining the radius of curvature and beam diameter of a Gaussian beam propagating with a wavelength,  $\lambda$  in free space along the z direction. This theoretical coupling efficiency does not take into consideration the Fresnel reflections of the end-facets of the waveguide.

$$w_x(z) = w_{lx} \sqrt{1 + \left( \frac{\lambda z}{\pi w_{lx}^2} \right)^2} \quad (3.6)$$

$$w_y(z) = w_{ly} \sqrt{1 + \left( \frac{\lambda z}{\pi w_{ly}^2} \right)^2} \quad (3.7)$$

$$R_x(z) = z \left[ 1 + \left( \frac{\pi w_{lx}^2}{\lambda z} \right)^2 \right] \quad (3.8)$$

$$R_y(z) = z \left[ 1 + \left( \frac{\pi w_{ly}^2}{\lambda z} \right)^2 \right] \quad (3.9)$$

The fabricated rib waveguides were designed to support SM light propagation at a wavelength of 980 nm, but because the transmission measurements are being carried out at 1064 nm an investigation was performed into how the wavelength of the light propagating at 1064 nm affects shape of mode profile. How much the shape of the mode intensity profile differs between the two wavelengths can affect coupling efficiency and as a result affect the estimation of the waveguide propagation losses. COMSOL simulations of the mode profiles for 1064 nm radiation propagating within the rib structure were carried out. The model was identical to the one described in Chapter 2 for a rib 1  $\mu\text{m}$  thick with an etch depth of 150 nm, other than a wavelength of 1064 nm was used. Figure 3.15 shows the comparison of the FWHM of spot sizes for mode intensity profiles of light propagation in the rib waveguide structure at wavelengths of 980 nm and 1064 nm. From figure 3.15 it can be seen that the spot sizes in the horizontal and vertical directions for the two simulated wavelengths exhibit the same trend as the width of the rib increases. The difference in spot size in the horizontal direction starts at 4% for rib widths less than 1  $\mu\text{m}$  but reduces to less than 1% for rib width greater than 3  $\mu\text{m}$ , and in the vertical direction a  $\approx 1.5\%$  difference was seen for the spot size for all rib widths. This indicates that selecting the wavelength of 1064 nm allows for

transmission measurements with similar coupling efficiencies with the launch fibre as that with light propagating at a wavelength of 980 nm, without the high absorption of the Yb ions.

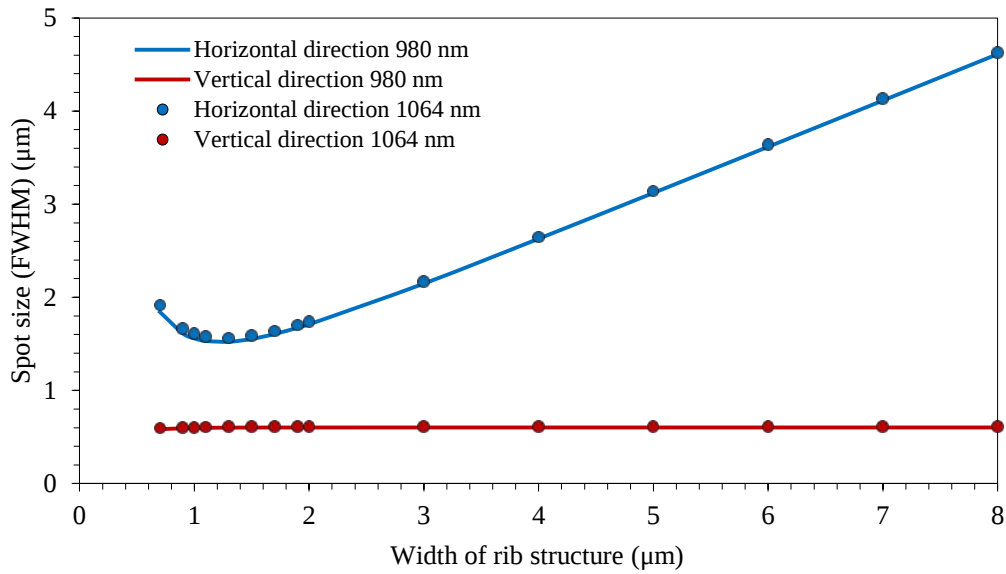


Figure 3.15 COMSOL simulation comparison of FWHM of the fundamental mode intensity profiles in the horizontal and vertical directions between laser pump (980 nm) and transmission measurement wavelength (1064 nm).

The coupling efficiency with respect to the separation gap between the fibre and waveguide end-facet was plotted for various rib widths, as shown in figure 3.16. The theoretical model, using equations (3.1)-(3.9) calculated the coupling efficiency of a fibre with a FWHM mode field diameter of  $5.2 \mu\text{m}$  launched into the waveguide at the end-facet.

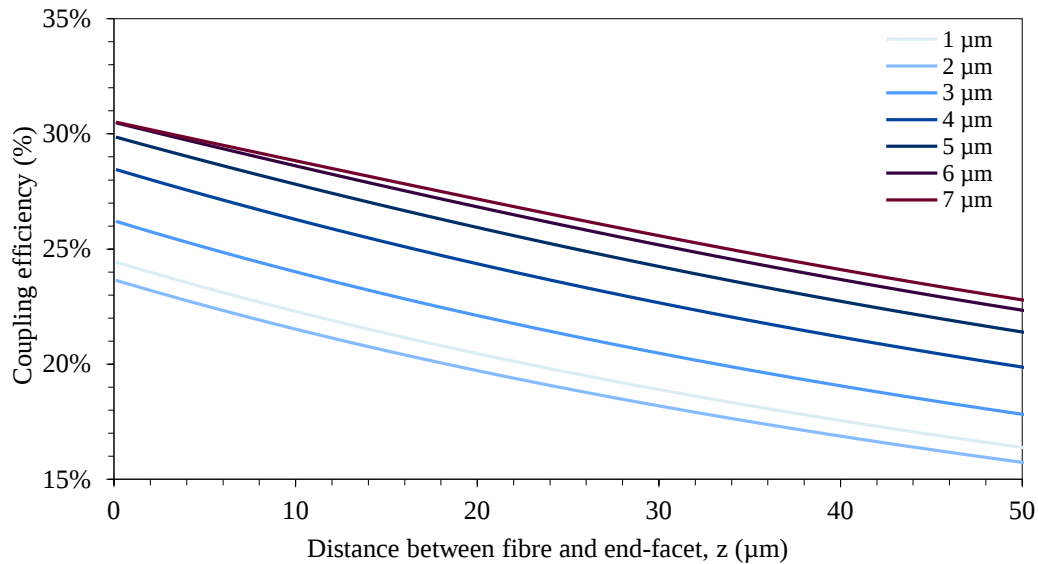


Figure 3.16 Theoretical model of coupling efficiency between 1064 nm input laser beam (FWHM MFD,  $w_0 = 5.2 \mu\text{m}$ ) and electric field profiles of rib waveguide found with COMSOL simulations.

As expected the coupling efficiency decreased as the launch fibre was moved away from the end-facet of the waveguide. Figure 3.17 shows the increase in rib widths from  $0.7 \mu\text{m}$  to  $1.1 \mu\text{m}$  the coupling efficiency decreases from  $\approx 27\%$  to a minimum of  $\approx 23\%$  and then increases to  $\approx 31\%$  for

rib width of 7  $\mu\text{m}$ . For the 1  $\mu\text{m}$  waveguide an exact numerical overlap for coupling efficiency calculation was carried out and yielded 23% which is close to 24% estimated shown in figure 3.17, therefore an acceptable approximation to estimate losses and other parameters.

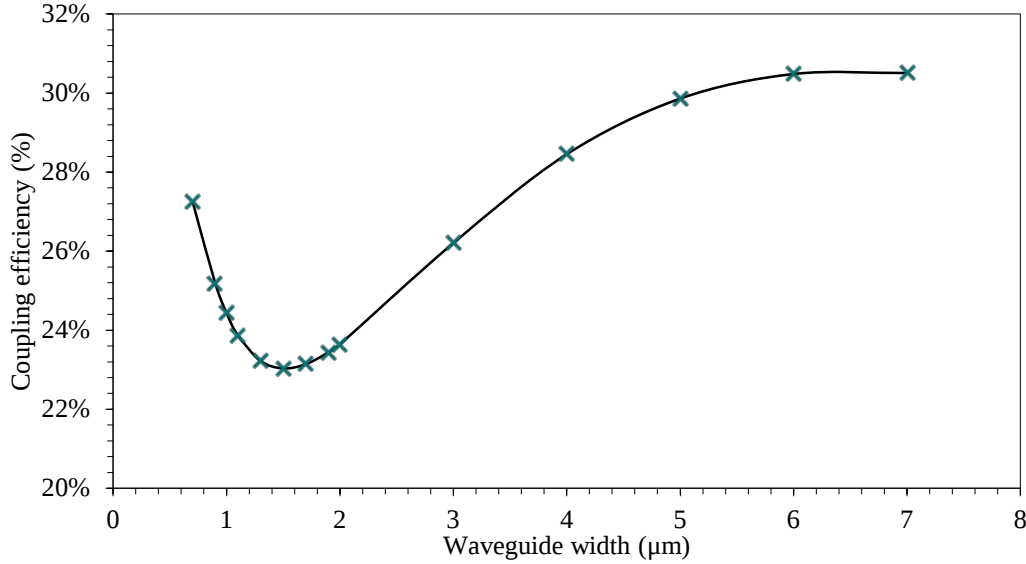


Figure 3.17 Coupling efficiencies for different rib widths when minimum beam waist of the 1064 nm laser output fibre is at position  $z \approx 0$  from the waveguide end-facet, assuming perfect alignment ( $x, y$ ).

### 3.5.1.2 Transmission measurements results

Transmission loss measurements were carried out on 5.4  $\mu\text{m}$  wide rib waveguide which was also used in creating a waveguide laser with a cavity formed using mirrors and bare end-facets. The calculated coupling efficiency for the 5.4  $\mu\text{m}$  wide waveguide, with the theoretical values plotted in figure 3.17, was estimated to be  $30 \pm 2\%$ . The transmission measurement for the 5.4  $\mu\text{m}$  wide waveguide is given in table 3.3, leading to an estimate propagation loss of  $4.7 \pm 0.2$  at 1064 nm.

Laser diode input power (mW)	Launched input power with $30 \pm 2\%$ coupling efficiency (mW)	Power measured by photo-detector (mW)	Estimated loss (dB/cm)
48.2	14.5	4.9	$4.7 \pm 0.2$

Table 3.3 Transmission loss measurement data.

### 3.5.2 Fabry-Perot propagation loss analysis

A complementary non-destructive method which determines the total cavity loss including the end-facets loss of a rib waveguide is the Fabry-Perot method. This technique is based on measuring the contrast of Fabry-Perot resonances formed by parallel, optically polished end-facets perpendicular at the ends of the waveguide. For the case of a Yb:Ta<sub>2</sub>O<sub>5</sub>/air interface there is a Fresnel reflectivity of approximately 12% at each end-facet. By varying the wavelength of the propagating light within the waveguide cavity, constructive and destructive interference take place causing peaks and trough of the output transmission with respect to wavelength. The measurements of the contrast of the resonances can be used to calculate a loss reflection ratio, and as a deduction an upper limit of the attenuation coefficient. The contrast ( $\gamma$ ) of this transmission spectrum is defined by [18]–[20]

$$\gamma = \frac{I_{max} - I_{min}}{I_{max} + I_{min}} \quad (3.10)$$

where  $I_{max}$  and  $I_{min}$  are the linear maximum and minimum output intensities. Assuming the waveguides have a perpendicular end facet to the direction of propagation, the propagation loss ( $\Lambda$ ) in dB can be calculated using the expression

$$\Lambda = 4.34 \left[ \ln R - \ln \frac{1 - \sqrt{1 - \gamma^2}}{\gamma} \right] \quad (3.11)$$

where  $R$  is the end facet Fresnel reflection coefficient between the air and effective index of the waveguide mode given by

$$R = \frac{(n_{eff} - 1)^2}{(n_{eff} + 1)^2} \quad (3.12)$$

The propagation loss described by equation (3.11) includes the losses due to Fresnel reflections with the first term in the square brackets and the total waveguide loss (dB) as the second term.

A factor affecting the accuracy of the losses measured is the quality of the polished end-facets to obtain good reflections. It is difficult to ascertain how good the end facet is, hence there is always an error associated with the Fresnel coefficient when calculating the waveguide losses and as result the estimated propagation loss by the FP method is an upper limit.

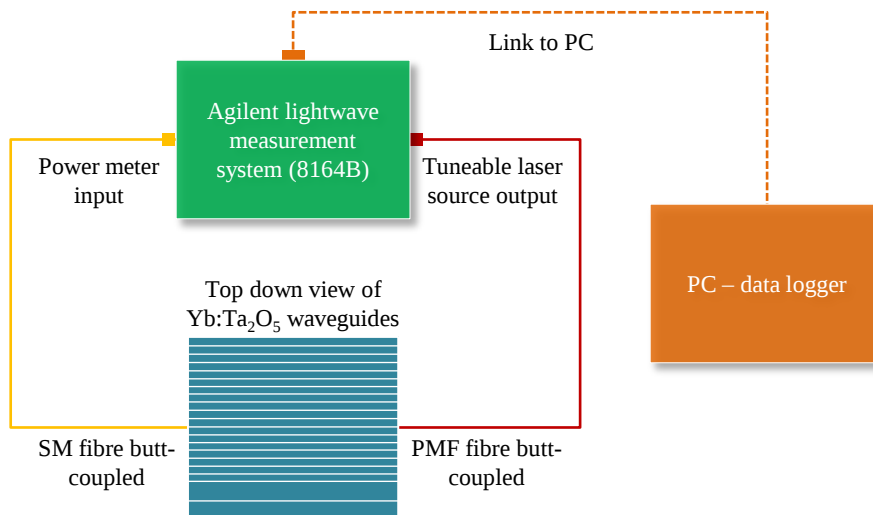


Figure 3.18 FP loss measurement experimental set-up.

To evaluate the propagation losses of the waveguide using the FP method, a tuneable laser source (TLS) was required to sweep a range of wavelengths around the region of 1550 nm, far from the absorption band of the Yb-doped material. An Agilent lightwave measurement system was used to

provide both the TLS (Agilent 81635A) and photo-detector (InGaAs detector Agilent 81600B), which was connected to a PC for data collection.

Connected to the TLS is a polarization maintaining fibre (PMF) butt-coupled to the end facet of the waveguides, launching TE polarized light. The resulting output light was collected with a SMF-28 fibre butt-coupled at the outlet of the waveguide and fed into the power detector module.

### 3.5.2.1 *Fabry-Perot propagation loss results*

The tuneable laser source swept wavelengths between 1540 nm and 1560 nm with a resolution of 1 pm for waveguides with rib widths of 6  $\mu\text{m}$ , 7  $\mu\text{m}$ , 8  $\mu\text{m}$ , 9  $\mu\text{m}$ , and 10  $\mu\text{m}$ . Figure 3.1 shows the normalised transmission obtained for a 6  $\mu\text{m}$  and 9  $\mu\text{m}$  wide waveguide and shows the contrast pattern which is used to calculate propagation loss of the waveguide. The free spectral range (FSR) for the 6  $\mu\text{m}$  and 9  $\mu\text{m}$  are 0.058 nm and 0.055 nm, which yield the effective index of the mode to be 1.9 and 2.0 respectively.

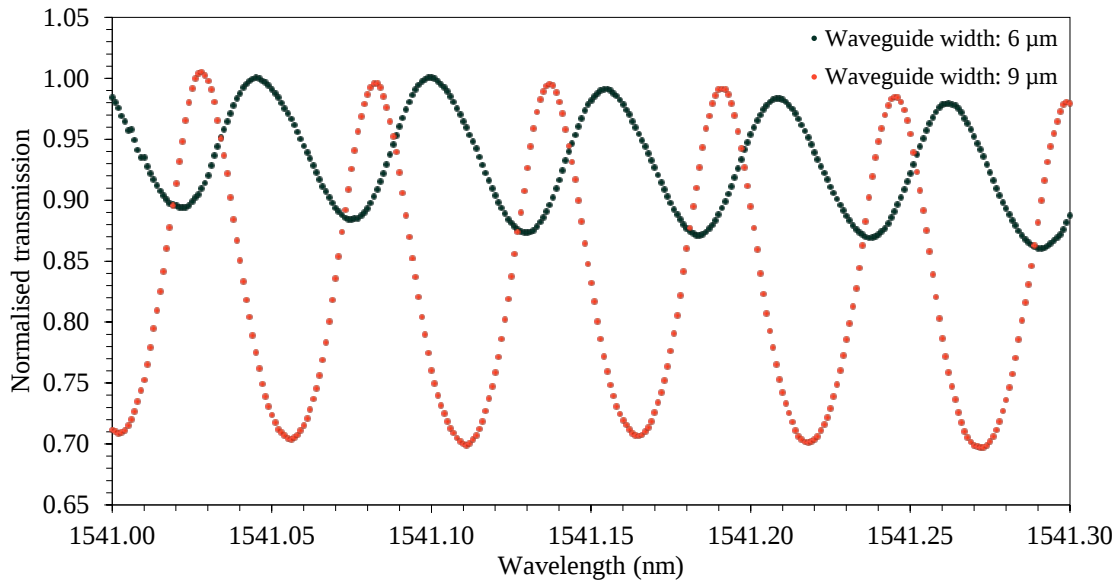


Figure 3.19 Propagation loss measurement in Yb:Ta<sub>2</sub>O<sub>5</sub> rib waveguide using the FP method. Data plotted for waveguides with widths of 6  $\mu\text{m}$  and 9  $\mu\text{m}$ .

The contrast of the pattern for 6  $\mu\text{m}$  wide waveguide is small compared to that seen for the 9  $\mu\text{m}$  wide waveguide implying the loss in the 6  $\mu\text{m}$  wide waveguide is higher than the 9  $\mu\text{m}$ . The losses calculated from the contrast pattern for various rib widths is shown in table 3.4 for two different centre wavelengths.

From the propagation loss calculations based on the FP loss method it can be seen that there is no systematic change of the loss with respect to the waveguide width and that the propagation losses vary significantly between waveguides. Comparing the calculated propagation losses using the FP method for two different centre wavelengths at each waveguide shows a variation of propagation losses that is due to a variation in the contrast. This variation of the contrast can be seen in figure

3.20, showing the data for each waveguide measured for wavelengths between 1541 nm and 1559 nm.

Waveguide width	Centre wavelength (nm)	
	1541	1548
	Propagation loss (dB/cm)	
6 $\mu\text{m}$	5.6	7.6
7 $\mu\text{m}$	6.0	2.4
8 $\mu\text{m}$	4.4	5.7
9 $\mu\text{m}$	1.3	1.4
10 $\mu\text{m}$	12.7	11.1

Table 3.4 Waveguides and their corresponding propagation losses calculated using the FP method at different centre wavelengths.

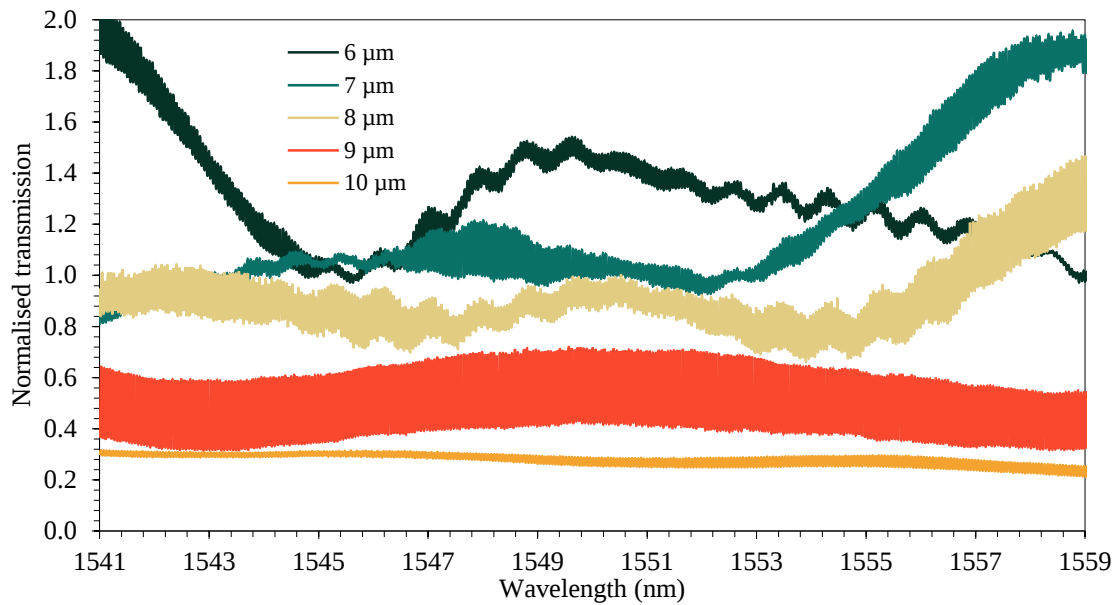


Figure 3.20 Propagation loss measurement in Yb:Ta<sub>2</sub>O<sub>5</sub> rib waveguide using the FP method for all waveguides measured, showing the variation in the measurements taken.

While the origin of this variability of the measured losses is unknown, possible explanations are that other Fabry-Perot effects might be influencing the FP loss measurements, which could have been introduced from cavities created between waveguide end-face and input fibre, within the input and collection fibres, in addition to possible modal beating due to higher order modes, material imperfections or channel defects. Another reason for this large variation in propagation losses for FP method might stem from the dependency of this method on the quality of the optically polished end-facets and accuracy of the end-facets and waveguide perpendicularity. Therefore for waveguide propagation losses the transmission measurement result of 4.7 dB/cm will be used, while total cavity losses should use the round-trip loss deduced from the FP measurement.

### 3.6 Conclusion

In this chapter the fabrication process for the creation of Yb-doped Ta<sub>2</sub>O<sub>5</sub> waveguides is presented utilizing RF sputtering, photolithography and dry etch processes commonly used in CMOS

fabrication. Yb:Ta<sub>2</sub>O<sub>5</sub> films 1 μm thick were deposited by RF magnetron sputter deposition onto a silicon substrate and shallow rib channels with an etch depth of 150 nm were created using a combination of photolithography and ion beam milling. The waveguides were encapsulated in thermally-grown silica under-cladding and RF magnetron sputtered silica over-cladding. In preparation for characterisation waveguide chips 10.8 mm long were cut and optically polished. The fabricated rib waveguide structure was found not to have vertical inner rib side walls but instead to have a double slope with an initial slope pitch of approximately 53° with the next connecting slope levelling out with the waveguide's outer slab region with an angle of 5°. COMSOL simulations were carried out to investigate the effect the double sloped side wall would have on the size of mode intensity profile compared to straight vertical edged side wall. From the simulation and comparison it was found that the FWHM of the spot size for the sloped side wall in the vertical direction increased by ≈ 0.5% and in the horizontal direction increased by ≈ 12% for a rib 2 μm wide, with this increase reducing to 4% for larger rib widths of 10 μm.

Characterisation in the form of imaging of the mode intensity profiles were carried out and analysed and showed partial agreement with simulations results for straight edged side wall waveguide with effects of PSF and sloped side walls causing increase in FWHM of the spot size. Within this chapter a theoretical technique used to estimate the coupling efficiency of light launched into a waveguide was introduced and used throughout this work. Propagation loss measurements were carried out through transmission measurements combined with the estimation of the launch efficiency of 1064 nm light into the waveguide. As discussed within this chapter the mode intensity profiles of fabricated rib waveguides did not closely follow the simulated mode intensity profiles, therefore the approximation of the launch efficiency will introduce an error as the calculation of coupling efficiency used the simulated mode intensity profiles. FP loss measurements were also presented. The loss measurements resulted in a large variation of the estimated propagation losses for the FP method, as losses ranged between 1.3 dB/cm to 12.7 dB/cm with the origin of this variability unknown.

### 3.7 Bibliography

- [1] J. S. Levy, A. Gondarenko, M. A. Foster, A. C. Turner-Foster, A. L. Gaeta, and M. Lipson, "CMOS-compatible multiple-wavelength oscillator for on-chip optical interconnects," *Nat. Photonics*, vol. 4, no. 1, pp. 37–40, Jan. 2010.
- [2] G. N. van den Hoven, R. J. I. M. Koper, A. Polman, C. van Dam, J. W. M. van Uffelen, and M. K. Smit, "Net optical gain at 1.53 μm in Er-doped Al<sub>2</sub>O<sub>3</sub> waveguides on silicon," *Appl. Phys. Lett.*, vol. 68, no. 14, p. 1886, 1996.
- [3] C.-Y. Tai, J. Wilkinson, N. Perney, M. Netti, F. Cattaneo, C. Finlayson, and J. Baumberg, "Determination of nonlinear refractive index in a Ta<sub>2</sub>O<sub>5</sub> rib waveguide using self-phase modulation.," *Opt. Express*, vol. 12, no. 21, pp. 5110–5116, 2004.

- 
- [4] J. D. Bradley, R. Stoffer, L. Agazzi, F. Ay, K. Wörhoff, and M. Pollnau, "Integrated Al<sub>2</sub>O<sub>3</sub>:Er<sup>3+</sup> ring lasers on silicon with wide wavelength selectivity," *Opt. Lett.*, vol. 35, no. 1, p. 73, Jan. 2010.
- [5] E. H. Bernhardt, H. A. G. M. van Wolferen, K. Wörhoff, R. M. de Ridder, and M. Pollnau, "Highly efficient, low-threshold monolithic distributed-Bragg-reflector channel waveguide laser in Al<sub>2</sub>O<sub>3</sub>:Yb<sup>3+</sup>," *Opt. Lett.*, vol. 36, no. 5, pp. 603–605, 2011.
- [6] B. Unal, M. C. Netti, M. A. Hassan, P. J. Ayliffe, M. D. B. Charlton, F. Lahoz, N. M. B. Perney, D. P. Shepherd, Chao-Yi Tai, J. S. Wilkinson, and G. J. Parker, "Neodymium-doped tantalum pentoxide waveguide lasers," *IEEE J. Quantum Electron.*, vol. 41, no. 12, pp. 1565–1573, Dec. 2005.
- [7] A. Z. Subramani, C. J. Oton, D. P. Shepherd, and J. S. Wilkinson, "Erbium-doped waveguide laser in tantalum pentoxide," *IEEE Photonics Technol. Lett.*, vol. 22, no. 21, pp. 1571–1573, Nov. 2010.
- [8] O. Brand and G. K. Fedder, *CMOS-MEMS: advanced micro and nanosystems (Volume 2)*. Wiley, 2005.
- [9] R. A. Soref, J. Schmidtchen, and K. Petermann, "Large single-mode rib waveguides in GeSi-Si and Si-on-SiO<sub>2</sub>," *IEEE J. Quantum Electron.*, vol. 27, no. 8, pp. 1971–1974, 1991.
- [10] K. Reinhardt and W. Kern, *Handbook of silicon wafer cleaning technology*, Second edi. William Andrew, 2008.
- [11] A. Z. Subramanian, C. J. Oton, J. S. Wilkinson, and R. Greef, "Waveguiding and photoluminescence in Er<sup>3+</sup>-doped Ta<sub>2</sub>O<sub>5</sub> planar waveguides," *J. Lumin.*, vol. 129, no. 8, pp. 812–816, Aug. 2009.
- [12] W. D. Callister and D. G. Rethwisch, *Fundamentals of materials science and engineering: An integrated approach*, 4th edit. New York, USA: Wiley, 2011.
- [13] R. G. Driggers and C. Hoffman, *Encyclopedia of Optical Engineering*, 1 st edit. Florida, USA: CRC Press, 2003.
- [14] A. Subramanian, "Tantalum pentoxide waveguide amplifier and laser for planar lightwave circuits," Ph.D. Thesis, University of Southampton, U.K., 2011.
- [15] M. J. Madou, "Faceting due to angle-dependent sputter rate," in *Fundamentals of Microfabrication and Nanotechnology Vol II*, 3rd edit., CRC Press, 2011, pp. 175–177.
- [16] K. Rossmann, "Point Spread-Function, Line Spread-Function, and Modulation Transfer Function," *Radiology*, vol. 93, no. 2, pp. 257–272, Aug. 1969.
- [17] O. G. Hellesø, P. Benech, and R. Rimet, "Diode laser butt coupling to K<sup>+</sup> diffused waveguides in glass," *IEEE Photonics Technol. Lett.*, vol. 4, no. 8, pp. 900–902, 1992.
- [18] G. Tittelbach, B. Richter, and W. Karthe, "Comparison of three transmission methods for integrated optical waveguide propagation loss measurement," *Pure Appl. Opt. J. Eur. Opt. Soc. Part A*, vol. 2, no. 6, pp. 683–700, 1999.

- [19] T. Feuchter and C. Thirstrup, "High precision planar waveguide propagation loss measurement technique using a Fabry-Perot cavity," *IEEE Photonics Technol. Lett.*, vol. 6, no. 10, pp. 1244–1247, Oct. 1994.
  
- [20] D. Castaldini, P. Bassi, S. Tascu, G. Sauder, P. Aschieri, M. De Micheli, P. Baldi, K. Thyagarajan, and M. R. Shenoy, "All-in-one measurement setup for fast and accurate linear characterization of guided-wave optical devices," *Opt. Eng.*, vol. 46, no. 12, p. 124601, Dec. 2007.

# CHAPTER 4

## Spectroscopy of Yb:Ta<sub>2</sub>O<sub>5</sub> Waveguides

### 4.1 Introduction

Designing a waveguide laser not only needs to take into consideration the geometric shape and refractive indices of the waveguide for tailoring the mode intensity profile of propagating pump and signal but also host material properties. Material properties such as the absorption cross-section,  $\sigma_{abs}$  must be known to design laser system so that the correct pump source is chosen to excite the gain ions. The emission cross-section,  $\sigma_{em}$  is another spectroscopic parameter for a laser material, and is directly connected to the gain of the material. It describes the probability of photon emission from an upper laser level and is inversely proportional to the lasing threshold value as shown in equation (5.21). The excited-state lifetime,  $\tau$  is the lifetime of the population of the upper laser level. This is also an important parameter as the length of the lifetime determines the amount of population inversion that can be maintained and is also inversely proportional to the lasing threshold. In this chapter spectroscopic parameters for Yb:Ta<sub>2</sub>O<sub>5</sub> are determined for the first time, using the fabricated rib waveguides described in Chapter 3. The absorption spectrum is first determined, in section 4.2 to establish the absorption cross-section and pumping wavelengths. The fluorescence spectrum was measured and is presented in section 4.3 showing the regions of emission occurring, and finally measurements of excited-state lifetime are presented in section 4.4. From the absorption and emission spectra the transition cross-sections are determined. These measurements were performed taking into account the effects of the waveguide configuration such as waveguide loss, the material/mode overlap factor and the potential for significant amplified spontaneous emission (ASE), the process where spontaneously emitted radiation is amplified.

#### 4.1.1 Ytterbium rare-earth ion

Ytterbium is trivalent rare-earth dopant that has been found to be versatile for many silica-based lasers and can be used to dope Ta<sub>2</sub>O<sub>5</sub> to create Yb:Ta<sub>2</sub>O<sub>5</sub>, but no Yb:Ta<sub>2</sub>O<sub>5</sub> laser has yet been presented. Ytterbium can operate as a quasi-three-level system with its main energy transition levels between the upper manifold <sup>2</sup>F<sub>5/2</sub> and the lower manifold <sup>2</sup>F<sub>7/2</sub> shown in figure 4.1, with the other energy levels in the ultra-violet wavelength region. The result of having a simple two-manifold energy structure is that undesired phenomena such as up-conversion, excited-state

absorption and cross-relaxation processes are halted, allowing for high power lasers [1], [2]. It has the advantage that it can be pumped by a wide selection of solid-state lasers such as InGaAs laser diodes (typical spectral range between 900 - 1000 nm) due to its broad absorption band, ranging from 850 nm to above 1070 nm [3].

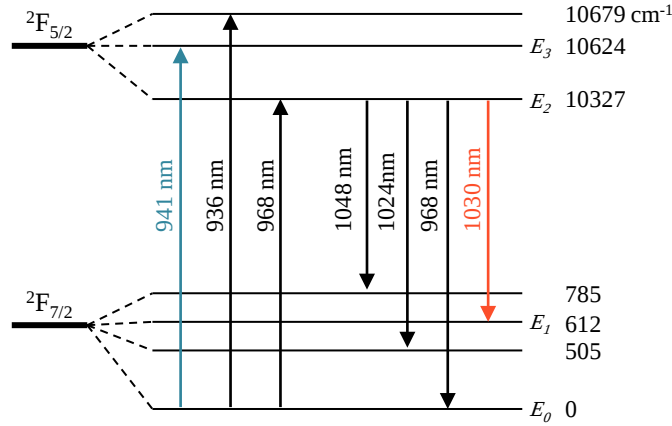


Figure 4.1 Energy level diagram for Yb:YAG laser

The energy structure of the ytterbium ion consists of four Stark levels in the lower manifold and three Stark levels in higher excited manifold. Although ytterbium doped lasers can be modelled as a quasi-three level laser systems, for input pump wavelengths ranging between 1  $\mu\text{m}$  – 1.2  $\mu\text{m}$  they behave like four level laser systems and, depending on the host, the upper laser manifold life-time has been shown to vary between 500  $\mu\text{s}$  to 1.4 ms [2].

## 4.2 Absorption spectrum and cross-section

Absorption spectroscopy of the  $\text{Yb}:\text{Ta}_2\text{O}_5$  waveguide was performed to determine the wavelengths of peak absorption and absorption bandwidths, with the information gained from these measurements used to highlight the relevant wavelengths required to excite the ytterbium ions for laser pumping. As a result the absorption cross-section of the  $\text{Yb}:\text{Ta}_2\text{O}_5$  could also be established, a parameter used to quantify the prospect of optical absorption occurring.

A waveguide insertion loss spectrum was obtained to determine the absorption of the Yb ion in  $\text{Ta}_2\text{O}_5$  with respect to wavelength. This was achieved using white light from a single-mode (SM) fibre-coupled broadband tungsten-halogen lamp. Light was coupled directly into the waveguide from the SM fibre through butt-coupling at the end-facet. The light coupled out of the waveguide's end-facet was collected using a multi-mode fibre and fed into an optical spectrum analyser (OSA), able to measure a wide range of wavelengths spanning between 700-1200 nm. A baseline reference measurement was made prior to investigation of the waveguide sample by capturing the white light from the single-mode fibre by butting it directly to the multimode fibre, without the waveguide sample in place. The experimental set-up is shown in figure 4.2.

Initially a 10.8 mm long sample was used for the absorption spectroscopy but it was evident from the initial data acquisition the experimental setup was not able to fully measure the ytterbium absorption spectrum because the nadir of the transmission could not be realised. This was due to a combination of low brightness white light source input (averaging -63.9 dBm/nm), low coupling efficiency from the standard single mode fibre to channel waveguides with very small spot size, and limitation of the lowest intensity measurable by the OSA (-100 dBm/nm) which all contributed towards a low signal-to-noise ratio.

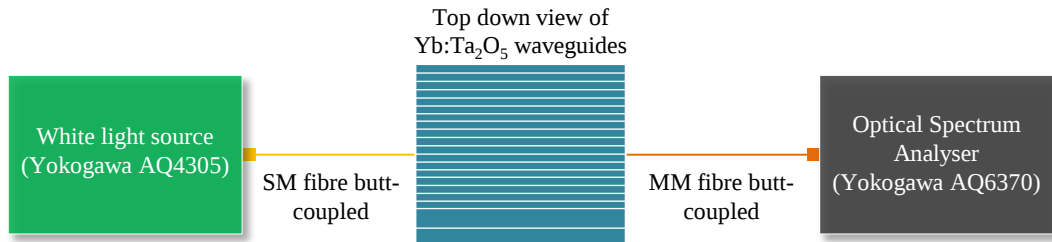


Figure 4.2 Set-up of Yb:Ta<sub>2</sub>O<sub>5</sub> waveguide absorption spectrum analysis.

To increase the signal-to-noise ratio of the measured absorption spectra, a waveguide with a shorter length of 3 mm was prepared to reduce the absorption at the wavelength of peak absorption. The waveguide with the widest width ( $\approx 37 \mu\text{m}$ ) was selected to ensure that maximum power travelled in the guiding core material so that the absorption measurement was a precise reflection of the Yb:Ta<sub>2</sub>O<sub>5</sub> material. To obtain the attenuation spectrum shown in figure 4.3, the spectrum of the baseline was subtracted from the spectrum of the Yb:Ta<sub>2</sub>O<sub>5</sub> waveguide.

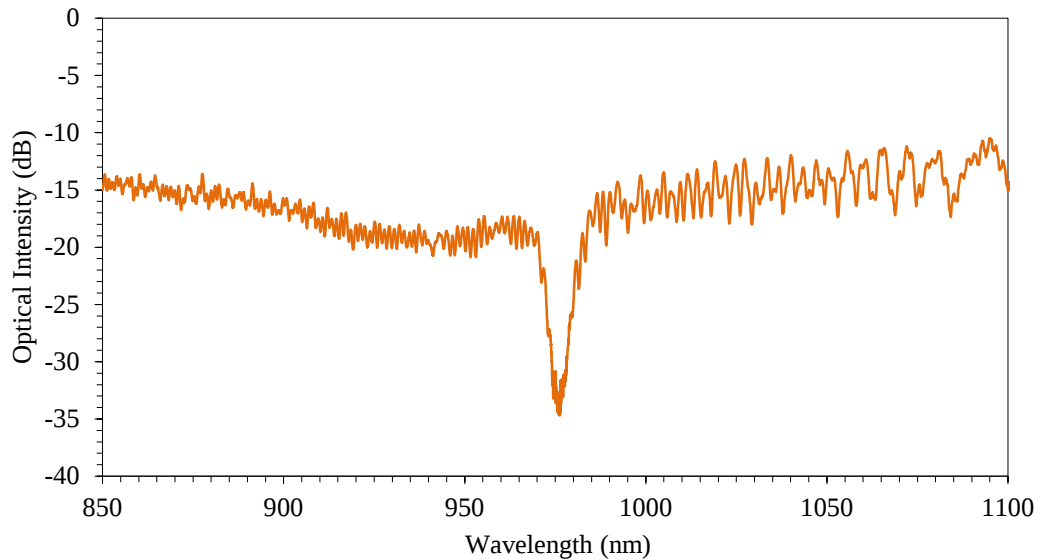


Figure 4.3 Yb:Ta<sub>2</sub>O<sub>5</sub> attenuation spectrum of a 3 mm long sample.

This captured attenuation spectrum includes loss contributions from fibre-waveguide coupling, propagation losses, and the Yb ions absorption. From figure 4.3 it can be seen that there are locations of peak and sub-peak absorption at wavelengths of 975 nm and 935 nm, corresponding to sub-levels in the  $^2F_{7/2} \rightarrow ^2F_{5/2}$  transition, where Yb-doped lasers are typically pumped. While the

insertion loss measurement is noisy due to low power spectral density, it is sufficient to determine the peak absorption cross-section with acceptable accuracy.

To obtain the absorption cross-section from the acquired absorption spectrum the Beer-Lambert law [4] was used, which describes the linear relationship between the absorbance and concentration of the absorbing ions. A plot of the absorption cross-section is shown in figure 4.4 and was determined by the Beer-Lambert law expressed by

$$I(\lambda) = I_0(\lambda)e^{\sigma_{abs}(\lambda)NL} \quad (4.1)$$

where  $I$  and  $I_0$  are the measured output intensity with and without a sample,  $L$  is the path length (cm),  $N$  is the concentration of ytterbium ions (molecule/cm<sup>3</sup>), and  $\sigma_{abs}$  is the absorption cross-section (molecule/cm<sup>3</sup>). For the 3 mm long Yb:Ta<sub>2</sub>O<sub>5</sub> sample measured, that had an estimated concentration of  $6.2 \times 10^{20}$  cm<sup>-3</sup> Yb ions, an estimated peak absorption cross-section of  $2.75 \pm 0.2 \times 10^{-20}$  cm<sup>2</sup> at 975 nm was determined from the absorption cross-section spectrum shown in figure 4.4.

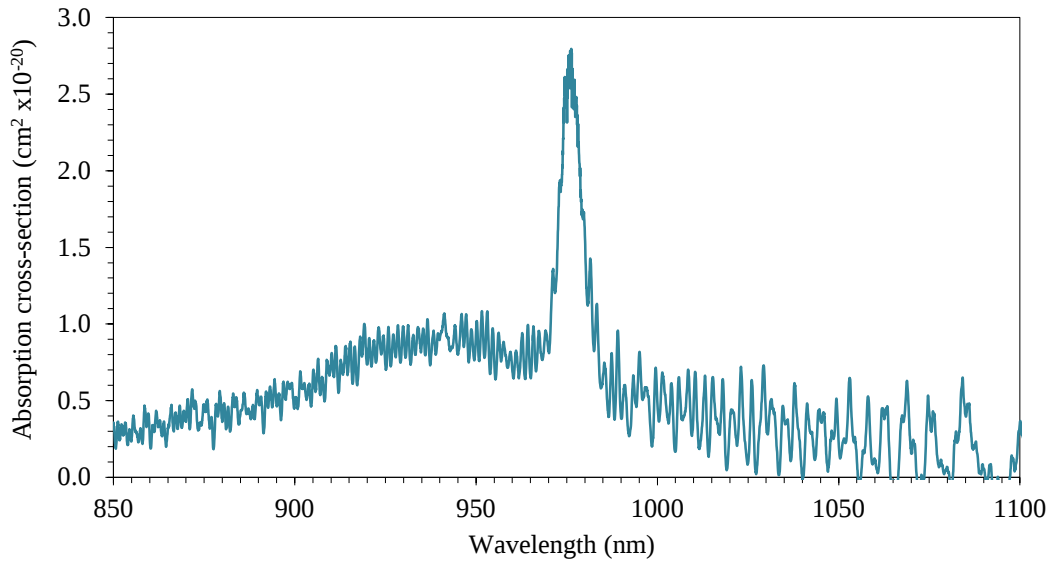


Figure 4.4 Yb:Ta<sub>2</sub>O<sub>5</sub> absorption cross-section.

### 4.3 Emission spectrum and cross-section

The fluorescence spectrum of a Yb:Ta<sub>2</sub>O<sub>5</sub> waveguide was measured to determine the emission cross-section, emission bandwidth and wavelength of peak emission, produced through the spontaneous emission process.

Figure 4.5 shows the experimental apparatus used to acquire fluorescence spectra, consisting of a 971 nm fibre Bragg grating stabilized laser source butt-coupled via a single-mode fibre into an end-facet of a waveguide. The fluorescence was collected using a multimode fibre positioned vertically above the waveguide close to the input inlet, and fed directly into an OSA. With this measurement

there is a risk that if pumped with a large power, spontaneously emitted radiation is amplified, distorting the fluorescence spectrum. The effect of this amplified spontaneous emission was minimised by acquiring emission spectra at different pump powers to establish the maximum input power for this measurement, with no spectral narrowing by ASE.

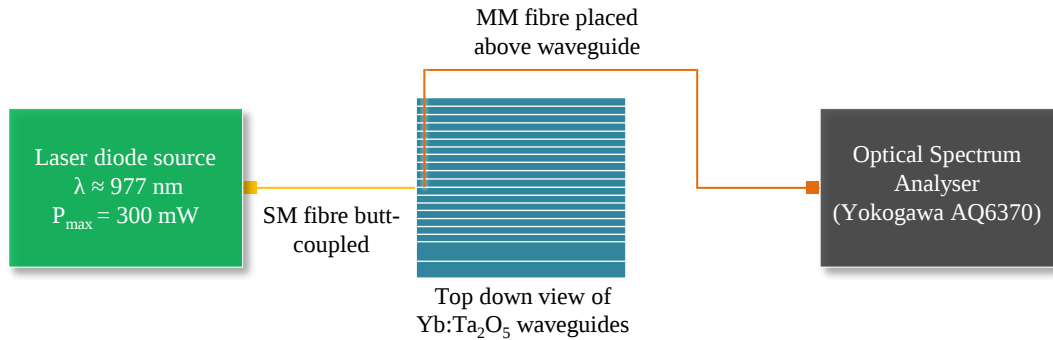


Figure 4.5 Set-up of Yb:Ta<sub>2</sub>O<sub>5</sub> waveguide fluorescence spectrum analysis.

The fluorescence spectrum acquired for the Yb:Ta<sub>2</sub>O<sub>5</sub> waveguide is shown in figure 4.6a. From the collected spectrum it is evident that there are three important regions shown in more detail in figure 4.6b and figure 4.6c. The first region figure 4.6a shows a broad fluorescence band between 930 nm and 1100 nm. The second region highlighted in figure 4.6c shows a fluorescence peak at a wavelength of 975 nm, and a nearby sharp peak at 971 nm due to scattered pump radiation. A further region, shown in figure 4.6b, peaks at a wavelength of 744 nm and is the most unexpected of the three regions. This is because the wavelength 744 nm corresponding to a wavenumber of 13440.86 cm<sup>-1</sup> is not evident in the Yb<sup>3+</sup> energy level diagram figure 4.1. Similar emission of wavelength was also shown by Paschotta et al. [5], who proposed that this may be caused by Ge-O defects leading to weak broadband fluorescence around 744 nm.

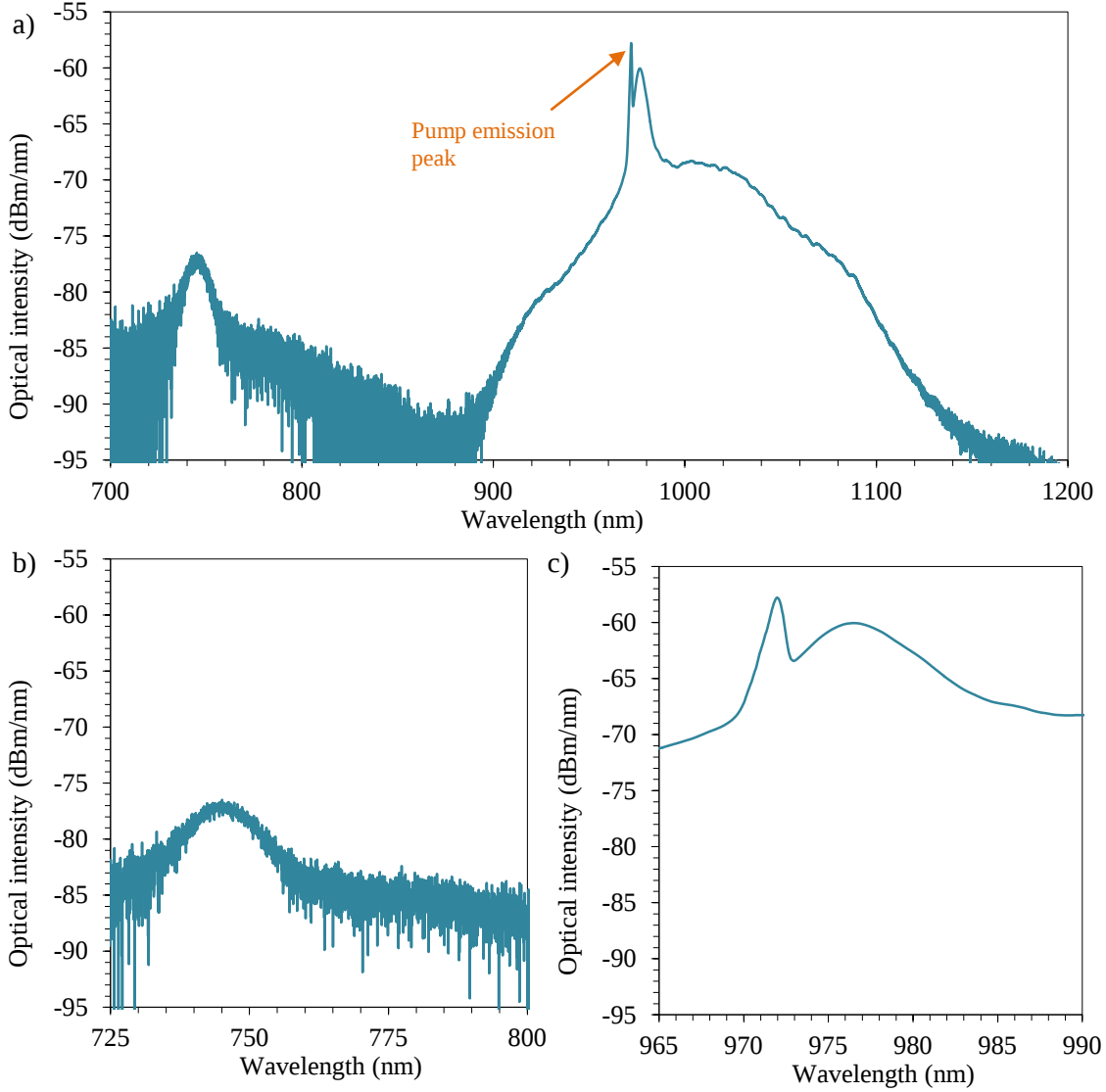


Figure 4.6 Fluorescence Spectrum of  $\text{Yb}:\text{Ta}_2\text{O}_5$  waveguide.

The McCumber or reciprocity method [6] was used to estimate the emission cross-section from the absorption cross-section shown in figure 4.4. The McCumber method scales the emission cross section and the absorption cross section to one another by the energy difference between the lowest Stark components of the upper and lower level manifolds and is described by

$$\sigma_{em}(\lambda) = \sigma_{abs}(\lambda) e^{\left[ \frac{hc}{k_B T} \left( \frac{1}{\lambda_{ZL}} - \frac{1}{\lambda} \right) \right]} \quad (4.2)$$

where  $\sigma_{abs}$  and  $\sigma_{em}$  are the absorption and emission cross-sections at the respective wavelength  $\lambda$ ,  $h$  is Planck's constant,  $c$  is the speed of light in vacuum,  $T$  is the temperature in Kelvin (294.15 K),  $k_B$  is the Boltzmann constant, and  $\lambda_{ZL}$  is the zero-phonon line (975 nm) [7]–[9].

The accuracy of the deduced cross-section shown in figure 4.7 is poor at longer wavelengths due to the noise in the absorption spectrum and the nature of the McCumber transform and was not plotted for wavelengths above 990 nm, but is acceptable close to 977 nm, where the emission cross-section

( $\sigma_{em}$ ) was estimated to be  $2.9 \pm 0.7 \times 10^{-20} \text{ cm}^2$ . Due to the noisiness of the McCumber emission spectrum the peak value was used as a scaling factor to plot the emission cross-section spectrum from the fluorescence spectrum as shown in figure 4.8.

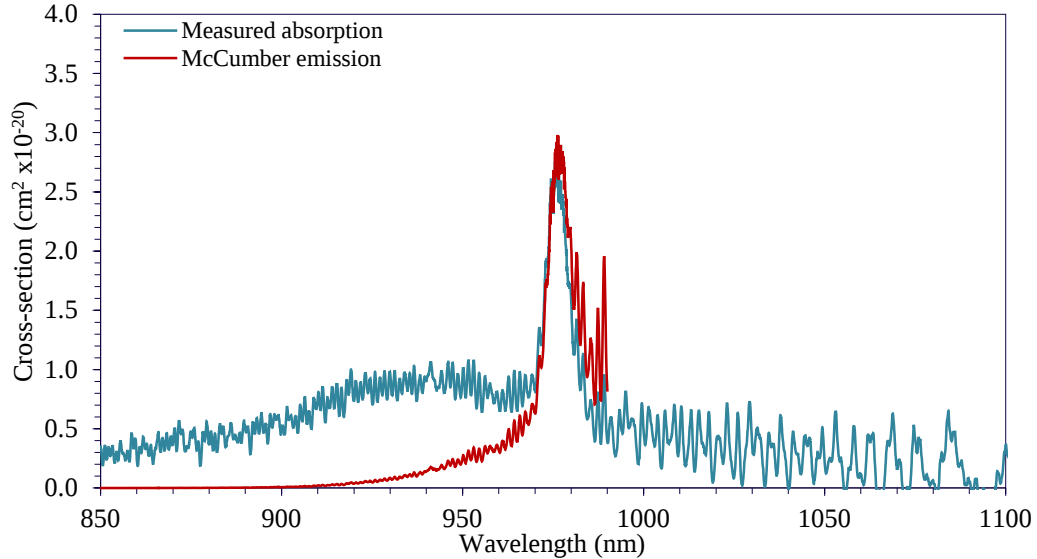


Figure 4.7 Absorption and emission cross-sections of ytterbium ions in Ta<sub>2</sub>O<sub>5</sub> waveguide. The emission cross-section was calculated from the absorption cross-section using McCumber theory.

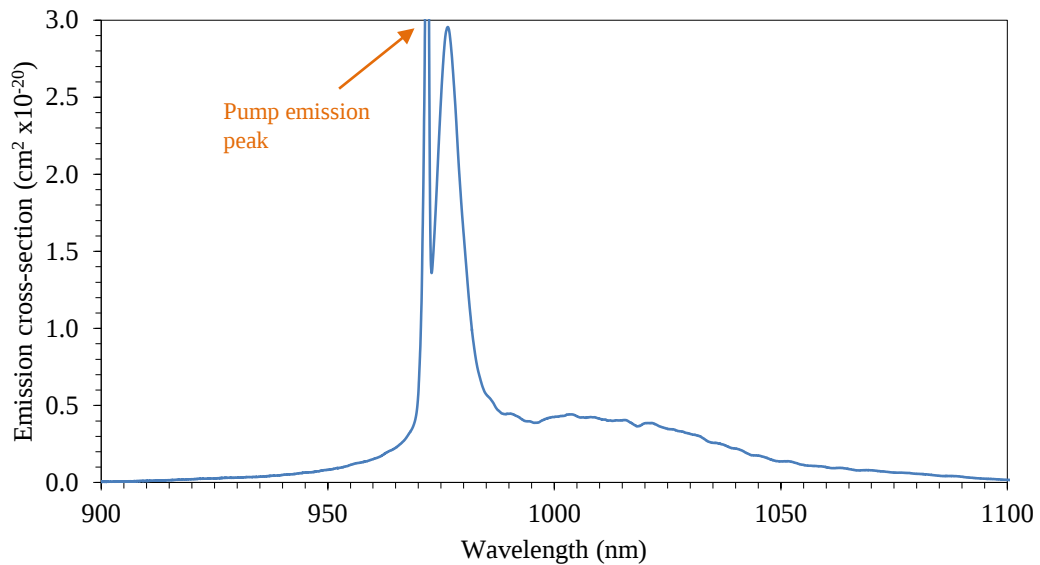


Figure 4.8 Emission cross-section spectrum scaled in accordance with to McCumber analysis applied to the absorption cross-section.

The emission cross-section spectrum, when pumped at a wavelength of 971 nm, comprises a broad emission band from 990 nm to 1090 nm with a separate strong peak at 977 nm similar to that reported in [10]. The broad emission bandwidth also shows similar a magnitude to other Yb-doped glasses [5], [11], [12] which are a much larger than those seen typically with Yb-doped crystals [3], [13], [14], although some crystals have shown to have a large gain bandwidth such Yb:YVO<sub>4</sub> ( $\Delta\lambda \approx 32 \text{ nm}$ ) [15].

#### 4.4 Excited-state lifetime

A fluorescence lifetime measurement was performed on a 10.8 mm long  $\text{Yb}:\text{Ta}_2\text{O}_5$  waveguide sample from the same wafer as that used for the absorption and fluorescence characterization. Figure 4.9 shows the experimental system used to measure the excited-state life time. 971 nm pump light from the fibre Bragg grating stabilized laser source was chopped at a frequency of 200 Hz using a mechanical chopper and focused into an end-facet of an  $\text{Yb}:\text{Ta}_2\text{O}_5$  waveguide, with the pump power kept minimal to avoid significant ASE. The light from the output of waveguide was collected with a microscope objective lens and passed through a set of long pass filters with a cut-off wavelength of 1  $\mu\text{m}$  to eliminate the residual pump wavelength.

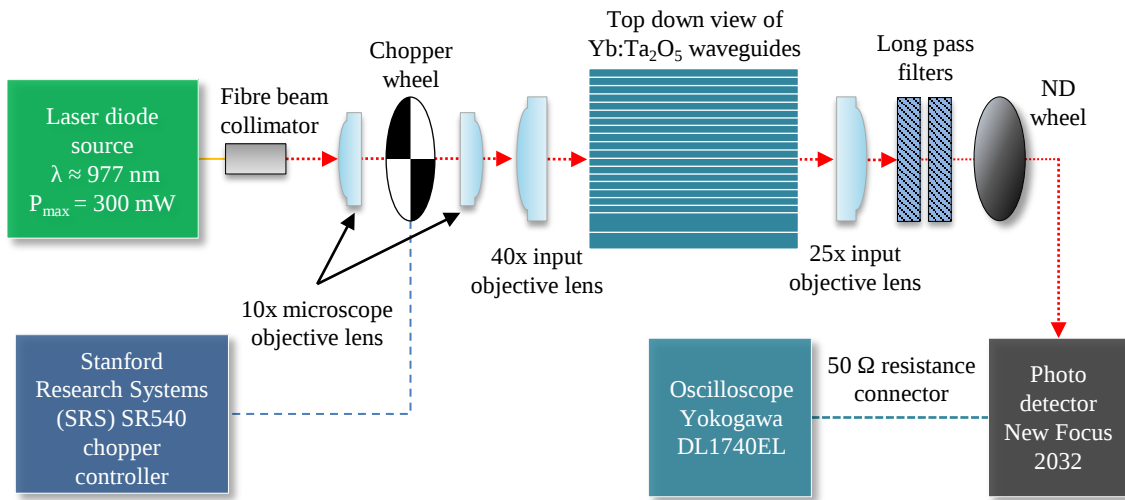


Figure 4.9 Experimental set-up for the analysis of excited-state lifetime for ytterbium ions in  $\text{Ta}_2\text{O}_5$  waveguides.

The resulting fluorescence power was then detected using a silicon photo-detector and amplifier (New Focus 2032) connected to an oscilloscope. A time resolution for the lifetime measurement system of  $\approx 20 \mu\text{s}$  was estimated by detecting the chopped excitation pump light without the sample in place and calculating the fall time of the chopped signal.

The decay of fluorescence power of the Yb ions in  $\text{Ta}_2\text{O}_5$  after excitation is shown in figure 4.10. The plot of the decay shows that there are multiple decay components contributing to the fall time of the fluorescence power. A model to describe the multi-exponential, based on assumption the decay is the sum of the single-exponential decays given by [16]

$$I(t) = \sum_{i=1}^{n_{decay}} \alpha_i e^{-\frac{t}{\tau_i}} \quad (4.3)$$

where  $\tau_i$  are the decay times,  $\alpha_i$  are the amplitudes of the components at  $t = 0$ , and  $n_{decay}$  is the number of decays occurring.

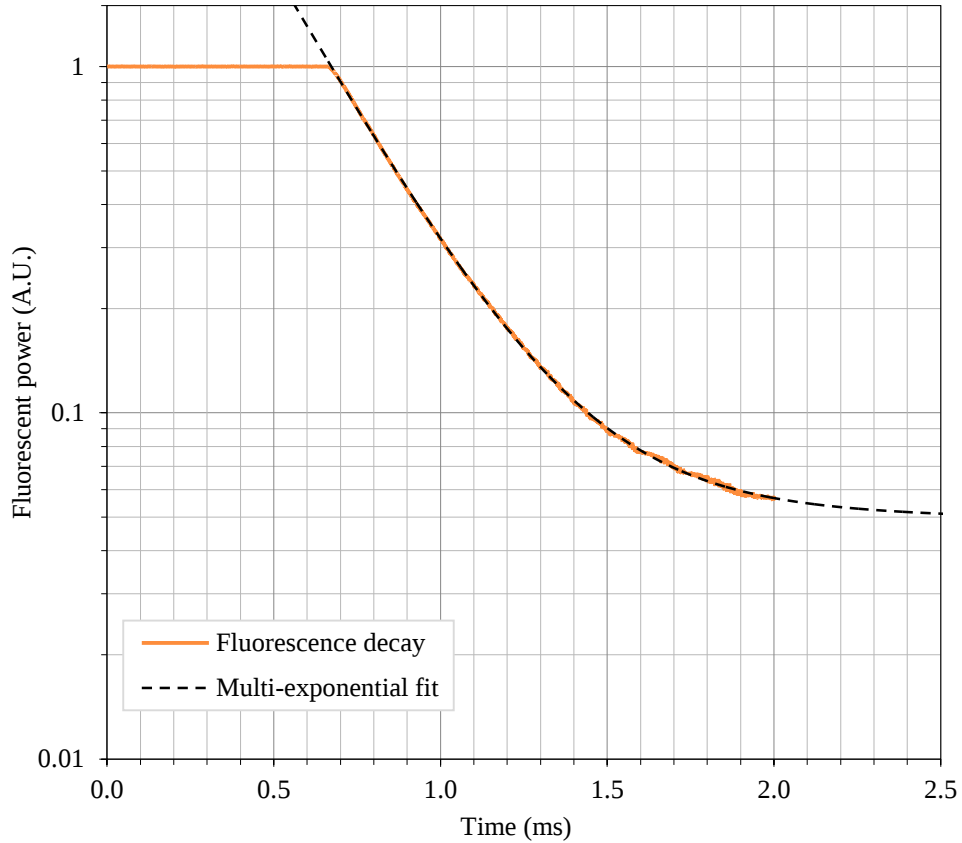


Figure 4.10 Radiative decay curve with multi-exponential fit.

The fit on the data in figure 4.10 gave a multi-exponential fit with two exponential terms giving an expression [17]

$$I(t) = 13.48e^{-3.95t} + 0.07e^{-0.15t} \quad (4.4)$$

The first exponential gives a fall time of  $\approx 0.25 \pm 0.03$  ms while the second gives a much larger fall time of  $6.7 \pm 0.03$  ms. The fall time from the second exponential is larger than excited-state lifetime typically seen for Yb-doped lasers [10]–[14], as shown in table 4.1, leading to the conclusion that this is a non-radiative process. The excited-state lifetime of Yb-doped Ta<sub>2</sub>O<sub>5</sub> is therefore assumed to be  $\tau \approx 0.25 \pm 0.03$  ms. The measured excited-state lifetime is small compared to those obtained by silicate, phosphate and ZBLAN glasses but more comparable to host materials with high refractive index such as KY(WO<sub>4</sub>) crystal and Bi<sub>2</sub>O<sub>3</sub>-based glasses, as shown in table 4.1.

## 4.5 Discussion

The absorption and emission cross-sections, fluorescence emission bandwidth and excited-state lifetime are key properties for Yb-doped lasing materials. Table 4.1 compares the spectroscopic properties of Yb:Ta<sub>2</sub>O<sub>5</sub> determined here with published data for other Yb-doped materials.

Host	Ta <sub>2</sub> O <sub>5</sub>	Bi <sub>2</sub> O <sub>3</sub> -based glass [10]	Silicate Q-246 [11]	Phosphate QX [11]	ZBLAN [12]	Tellurite 35PTY3Y [13]	KY(WO <sub>4</sub> ) [14]
Ytterbium ion density, N, ( $\times 10^{20} \text{cm}^{-3}$ )	≈ 6.2	1.6	≈ 17	≈ 20	2 wt.% Yb	3.41	3
Pump wavelength, $\lambda_p$ , (nm)	971	975	970	970	911	974.9	981.2
Emission bandwidth, $\Delta\lambda$ , (nm)	≈ 100	≈ 100	77	62	≈ 70	-	16
Peak emission cross-section, $\sigma_{em}$ , ( $\times 10^{-20} \text{cm}^2$ )	2.9 @977 nm	-	0.11 @970 nm	0.07 @970 nm	1.1* @975 nm	2.09 @975 nm	16* @980 nm
Peak absorption cross-section, $\sigma_{abs}$ , ( $\times 10^{-20} \text{cm}^2$ )	2.76 @975 nm	2.1 @977 nm	0.19 @970 nm	0.25 @970 nm	1.1* @975 nm	1.55 @975 nm	13.3 @981.2 nm
Excited-state lifetime, $\tau$ , (ms)	0.25	0.55	1.1	1.3	1.7	0.96	0.6
Refractive index	2.124	2.03	1.56	1.535	1.5	1.513 to 2.036 [18]	2.033

Table 4.1 Comparison of the spectroscopic properties of the Yb:Ta<sub>2</sub>O<sub>5</sub> studied in this work (red) with other Yb-doped glass (blue) and crystal (green) material systems. \*These cross-sections have been extracted from diagrams in the literature as accurately as possible

In comparison with other amorphous Yb-doped materials Yb:Ta<sub>2</sub>O<sub>5</sub> has a broad emission bandwidth and large absorption and emission cross-section and has the added advantage of compatibility with CMOS processing.

As a figure of merit, the theoretical maximum gain of Yb:Ta<sub>2</sub>O<sub>5</sub>, with the dopant density used here, was calculated at the measured wavelength of peak emission using the measured cross-section and assuming full inversion of Yb<sup>3+</sup> ions, which may be approached when pumping at the short wavelength absorption sub-peak [19], using

$$g_{mat} = 4.34N_{inv}\sigma_{em} \quad (4.5)$$

Where  $g_{mat}$  is the material gain (dB/cm),  $\sigma_{em}$  is the peak emission cross-section,  $2.9 \times 10^{-20} \text{cm}^2$  at 977 nm and  $N_{inv}$  is the inversion density. For full inversion,  $N_{inv} = N_T = 6.2 \times 10^{20} \text{cm}^{-3}$  (total concentration of ytterbium ions in Ta<sub>2</sub>O<sub>5</sub>), yielding a maximum potential gain of 78 dBcm<sup>-1</sup>. The combination of high potential gain with the broad bandwidth of Yb:Ta<sub>2</sub>O<sub>5</sub> shows promise for modelocked laser applications.

## 4.6 Conclusion

Yb-doped Ta<sub>2</sub>O<sub>5</sub> material was for the first time investigated as a possible laser host, with spectroscopic properties such as absorption and emission cross-sections, gain bandwidth and excited-state lifetime presented. An absorption spectroscopy was carried out on a 3 mm long Yb:Ta<sub>2</sub>O<sub>5</sub> waveguide by measuring the attenuation spectrum from white-light coupled directly into the waveguide from a SM fibre through butt-coupling at the end-facet. The light coupled out of the waveguide's end-facet was collected using a MMF and fed into an OSA. The resulting absorption

spectrum showed a peak and sub-peak absorption at wavelengths of 975 nm and 935 nm, with the corresponding absorption cross-section giving a peak cross-section of  $2.75 \pm 0.2 \times 10^{-20} \text{ cm}^2$  at 975 nm. A fluorescence spectrum was measured using a 977 nm laser source butt-coupled against the end-facet of the waveguide, with the fluorescence capture using a MMF positioned vertically above the waveguide's input inlet. This showed a broadband emission band from 990 nm to 1090 nm with a separate strong peak at 975 nm while being pumped at 971 nm. Using the McCumber analysis the emission cross-section was estimate to be  $2.90 \pm 0.7 \times 10^{-20} \text{ cm}^2$  at 975 nm. The excited-state life time was measured to be  $0.25 \pm 0.03 \text{ ms}$ . The material properties established from this study demonstrates that lasing is possible in Yb:Ta<sub>2</sub>O<sub>5</sub> and can be used in the development on-chip planar waveguide lasers and mode-locked laser, as result of the combination of high material gain and large broad bandwidth.

## 4.7 Bibliography

- [1] C. Cascales, M. D. Serrano, F. Esteban-Betegón, C. Zaldo, R. Peters, K. Petermann, G. Huber, L. Ackermann, D. Rytz, C. Dupré, M. Rico, J. Liu, U. Griebner, and V. Petrov, "Structural, spectroscopic, and tunable laser properties of Yb<sup>3+</sup>-doped NaGd(WO<sub>4</sub>)<sub>2</sub>," *Phys. Rev. B*, vol. 74, no. 17, p. 174114, Nov. 2006.
- [2] M. J. Digonnet, *Rare-earth-doped fiber lasers and amplifiers, revised and expanded*, 2nd edit. CRC Press, 2001.
- [3] W. F. Krupke, "Ytterbium solid-state lasers — the first decade," *IEEE J. Sel. Top. Quantum Electron.*, vol. 6, no. 6, pp. 1287–1296, 2000.
- [4] J. W. Robinson, *Atomic Spectroscopy*, 2nd Ed. CRC Press, 1996.
- [5] R. Paschotta, J. Nilsson, P. R. Barber, J. E. Caplen, A. C. Tropper, and D. C. Hanna, "Lifetime quenching in Yb-doped fibres," *Optics Communications*, vol. 136, no. 5–6, pp. 375–378, 1997.
- [6] D. E. McCumber, "Einstein relations connecting broadband emission and absorption spectra," *Phys. Rev.*, vol. 136, no. 4A, 1964.
- [7] W. J. Miniscalco and R. S. Quimby, "General procedure for the analysis of Er<sup>3+</sup> cross sections," *Opt. Lett.*, vol. 16, no. 4, p. 258, Feb. 1991.
- [8] M. J. F. Digonnet, E. Murphy-Chutorian, and D. G. Falquier, "Fundamental limitations of the McCumber relation applied to Er-doped silica and other amorphous-host lasers," *IEEE J. Quantum Electron.*, vol. 38, no. 12, pp. 1629–1637, Dec. 2002.
- [9] R. M. Martin and R. S. Quimby, "Experimental evidence of the validity of the McCumber theory relating emission and absorption for rare-earth glasses," *J. Opt. Soc. Am. B*, vol. 23, no. 9, p. 1770, 2006.
- [10] S. Ohara and Y. Kuroiwa, "Highly ytterbium-doped bismuth-oxide-based fiber," *Opt. Express*, vol. 17, no. 16, pp. 14104–14108, 2009.

- 
- [11] C. Hönninger, R. Paschotta, M. Graf, F. Morier-Genoud, G. Zhang, M. Moser, S. Biswal, J. Nees, A. Braun, G. A. Mourou, I. Johannsen, A. Giesen, W. Seeber, and U. Keller, “Ultrafast ytterbium-doped bulk lasers and laser amplifiers,” *Appl. Phys. B Lasers Opt.*, vol. 69, no. 1, pp. 3–17, 1999.
- [12] J. Y. Allain, M. Monerie, and H. Poignant, “Ytterbium-doped fluoride fibre laser operating at 1.02  $\mu\text{m}$ ,” *Electron. Lett.*, vol. 28, no. 11, pp. 988 – 989, 1992.
- [13] P. Nandi and G. Jose, “Ytterbium-doped P<sub>2</sub>O<sub>5</sub> -TeO<sub>5</sub> glass for laser applications,” *IEEE J. Quantum Electron.*, vol. 13, no. 2, pp. 101–103, 2006.
- [14] N. V. Kuleshov, A. A. Lagatsky, A. V. Podlipensky, V. P. Mikhailov, and G. Huber, “Pulsed laser operation of Yb-doped KY(WO<sub>4</sub>)<sub>2</sub> and KGd(WO<sub>4</sub>)<sub>2</sub>,” *Optics Letters*, vol. 22, no. 17, p. 1317, 1997.
- [15] V. E. Kisel, A. E. Troshin, V. G. Shcherbitsky, N. V. Kuleshov, V. N. Matrosov, T. A. Matrosova, M. I. Kupchenko, F. Brunner, R. Paschotta, F. Morier-Genoud, and U. Keller, “Femtosecond pulse generation with a diode-pumped Yb<sup>3+</sup>:YVO<sub>4</sub> laser,” *Opt. Lett.*, vol. 30, no. 10, p. 1150, May 2005.
- [16] J. R. Lakowicz, *Principles of fluorescence spectroscopy*, 3rd Edit. Springer US, 2011.
- [17] C.-C. Lee, *The current trends of optics and photonics*. Springer Netherlands, 2014.
- [18] Z. Duan, H. T. Tong, M. Liao, T. Cheng, M. Erwan, T. Suzuki, and Y. Ohishi, “New phospho-tellurite glasses with optimization of transition temperature and refractive index for hybrid microstructured optical fibers,” *Opt. Mater. (Amst.)*, vol. 35, no. 12, pp. 2473–2479, Oct. 2013.
- [19] D. Geskus, S. Aravazhi, E. Bernhardt, C. Grivas, S. Harkema, K. Hametner, D. Günther, K. Wörhoff, and M. Pollnau, “Low-threshold, highly efficient Gd<sup>3+</sup>, Lu<sup>3+</sup> co-doped KY(WO<sub>4</sub>)<sub>2</sub>:Yb<sup>3+</sup> planar waveguide lasers,” *Laser Phys. Lett.*, vol. 6, no. 11, pp. 800–805, 2009.

# CHAPTER 5

## CW Yb:Ta<sub>2</sub>O<sub>5</sub> Waveguide Lasers

### 5.1 Introduction

Lasers doped with ytterbium (Yb) ions exhibit long excited-state life-time yielding high gain efficiency and low pump power thresholds, low quantum defect providing good power-handling ability and low-cost optical pumping using semiconductor sources due to broad absorption at wavelengths near 980 nm. For the realisation of Yb-doped waveguide lasers and amplifiers, amorphous host materials such as silicate [1], phosphate [2], [3], bismuthate glasses [4] and Al<sub>2</sub>O<sub>3</sub> [5] have been studied. Further, crystalline materials such as YAG [6], [7], LiNbO<sub>3</sub> [8], [9], KGd(WO<sub>4</sub>)<sub>2</sub> [10]–[12] and LiYF<sub>4</sub> [13] have been similarly researched. Tantalum pentoxide (Ta<sub>2</sub>O<sub>5</sub>) is a promising alternative amorphous host material for Yb<sup>3+</sup> ions [14] that has been demonstrated as a laser host for neodymium [15] and erbium [16] trivalent rare-earth ions. Ta<sub>2</sub>O<sub>5</sub> can be used with CMOS fabrication technologies [17], leading to the potential of multi-functional, mass-producible, integrated optical circuits on silicon. The material also shows a large third-order non-linearity ( $n_2 \approx 7.25 \times 10^{-19} \text{ m}^2/\text{W}$  at  $\lambda \approx 980 \text{ nm}$ ) [18] with potential for all-optical processing, and a high-refractive index ( $n \approx 2.124$  at  $\lambda \approx 980 \text{ nm}$ ) [19] enabling compact photonic circuits with low bend loss.

Building upon the waveguide designs described in Chapter 2, the fabrication process described in Chapter 3 and the spectroscopic characterisation of Yb:Ta<sub>2</sub>O<sub>5</sub> material in Chapter 4, work carried out to characterise the lasing behaviour of Yb:Ta<sub>2</sub>O<sub>5</sub> rib waveguides is presented in this chapter. To characterize the lasing behaviour an evaluation of the pump efficiency is required with the necessary step detailed to estimate the pump efficiency in this chapter. These steps include knife-edge experiments to measuring the launched pump's beam waist and overlap integrals of pump beam waist and simulated mode intensity profiles found in Chapter 2. The waveguide lasing threshold and slope efficiencies are established for the first time in this chapter, from measurements of the output power with respect to the absorbed pump power. The waveguide laser was pumped through the end-facet into a cavity created using high-reflector mirrors, output couplers and bare end-facet combinations. Furthermore the lasing spectra were captured to determine the wavelength regions lasing occur within.

## 5.2 Basic principles of operation for Yb-doped lasers

### 5.2.1 Basic principles of laser operation

The word laser is an acronym derived from “light amplification by stimulated emission of radiation”, a process in which a device produces an intense beam of highly directional, coherent, monochromatic light. The fundamental physical phenomena a laser system exploits when an electromagnetic wave interacts with a material. The interactions cause three important processes that govern the transition of electrons between energy levels in a material: absorption, spontaneous emission and stimulated emission as illustrated with a simple two-level model in figure 5.1 [20].

Absorption is the process when an electron makes a transition from the lowest energy level (ground state,  $E_1$ ) to the highest energy level (excited state,  $E_2$ ) by absorbing electromagnetic radiation. For the electrons to make the transition, the amount of energy required from the electromagnetic radiation must be equal to the difference between the energy states,  $E = E_2 - E_1$ . The energy of electromagnetic wave (or photon) is described by the expression

$$E = h\nu = \frac{h}{\lambda} \quad (5.1)$$

Where  $E$  is the photon energy;  $h$  is Planck’s constant;  $\nu$  is the frequency of the photon and  $\lambda$  is the wavelength [20]. A parameter representing the probability that a photon is absorbed is defined by  $B_{12}$ , one of Einstein’s B coefficients and is directly proportional to the absorption cross-section ( $\sigma_{abs}$ ) giving by the expression [21]

$$\sigma_{abs} = \frac{h\nu B_{12} g(\nu)}{c} \quad (5.2)$$

where  $c$  is the speed of light in vacuum,  $h$  is Planck’s constant,  $\nu$  is frequency, and  $g(\nu)$  is the line shape function.

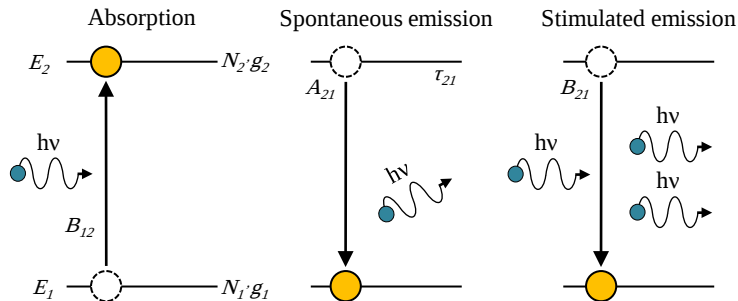


Figure 5.1 Light absorption and emission for two-level model

Once the electron is in the excited level,  $E_2$  it moves to a lower energy state by losing energy through emitting a photon with a frequency,  $\nu$ . The energy of the photon released is equal to the

difference between the two transitioned energy levels. The transition to a lower energy state occurs due to either stimulated or spontaneous emission process.

Spontaneous emission is a random process where photons emit from the excited state spontaneously after a certain period of time has passed since excitation occurred. The emitted photon emits in any direction and exhibits low coherence. The probability of the occurrence of spontaneous photon emission to occur per unit time is given by  $A_{21}$ , Einstein's A coefficient and is the reciprocal of the spontaneous radiative lifetime,  $\tau_{21}$ .

Stimulated emission occurs when an electron in the excited state is irradiated by a photon with a frequency of  $\nu$ , stimulating the release of a photon of the same phase, frequency and of the same direction of the photon which released it [20], [22]. If the population of electrons in the excited state is greater than that of the electrons in lower energy states then the medium is in a state of population inversion, which is required for a laser medium to produce gain for light amplification. With the rate of stimulated absorption described from energy state 1 to state 2 by  $B_{12}$ , the rate of the stimulated emission from energy state 2 to state 1 can also be describe using another B coefficient,  $B_{21}$ , where  $B_{12} = (g_2 B_{21}/g_1)$  and  $g_1$  and  $g_2$  are the degeneracy factors of levels 1 and 2. The stimulated emission cross-section ( $\sigma_{ems}$ ) can be described in terms of the  $B_{21}$  [23]

$$\sigma_{ems} = A_{21} \frac{\lambda^2}{8\pi n^2 \nu^2} g(\nu) \quad (5.3)$$

where  $n$  is the refractive index and  $A_{21}$  is given by

$$A_{21} = 2 \left( \frac{h\nu^3}{c^2} \right) B_{21} \quad (5.4)$$

A typical laser schematic, as illustrated in figure 5.2 consists of three key components that combine to create a laser system which are a pump source, a gain medium and optical resonator.

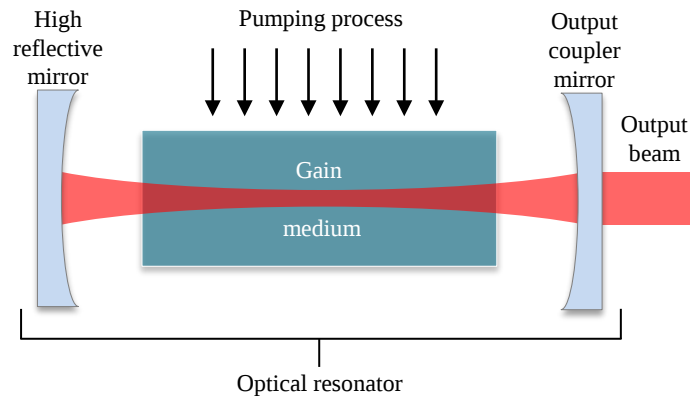


Figure 5.2 Schematic of a typical laser system, showing the three most important components; pump source, gain medium, & optical cavity.

The pump source is the mechanism which provides energy to the laser system to excite the electrons into the higher energy states. The pump injects photons into a laser gain medium where the process of light application occurs, therefore the type of pump source is directly related to the gain medium. The laser gain medium adds energy into the optical cavity and is required to compensate for the losses of the cavity. For oscillation to occur an optical resonator is needed to feedback the laser photons back into the gain medium to stimulate the emission of an identical photon.

Longitudinal laser cavity modes are the resonant modes produced as a result boundary conditions created because of the cavity mirrors developing standing waves, as shown in figure 5.3.

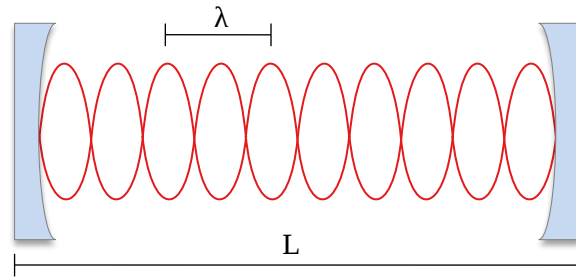


Figure 5.3 Longitudinal modes of an optical cavity formed by two mirrors.

Then number of longitudinal modes present depends on length of the laser cavity, where the laser resonant modes occur at wavelengths  $\lambda$  which satisfy [22]

$$m\lambda = 2L \quad (5.5)$$

where the  $L$  is the length of the cavity,  $\lambda$  is the wavelength of the laser source and  $m$  is an integer value of the number of modes. The frequency spacing,  $\Delta\nu$  between adjacent longitudinal modes can also be expressed by

$$\Delta\nu = \frac{c}{2L} \quad (5.6)$$

### 5.2.2 Theory of quasi-three-level lasers

In this section the numerical modelling of the performance of a longitudinally pumped laser using a generalized quasi-three-level system, figure 5.4 is presented. This model takes into consideration the reabsorption losses associated with quasi-three-level lasers due to thermal population at the lower laser levels [24], and presents an analysis for laser characteristics such as the laser threshold and slope efficiency. The pump and laser beams are modelled as non-symmetrical Gaussian beams with an elliptical spot size that does not diffract significantly within the laser medium. Effects of spatial hole burning is neglected in this analysis, and it is also assumed that unabsorbed light is not reflected back into the laser gain medium, meaning the pump light makes only a single pass through the laser medium [25]. The upper laser level population density  $N_2$  can be expressed using

$f_2$  as fraction of the total population of the upper laser manifold population density giving  $N_2 = f_2 N_U$ , where  $N_U$  is the total population of the upper laser manifold. Similarly the lower laser level population density  $N_1$  can be expressed using  $f_1$  as fraction of the total population of the lower laser manifold population density giving  $N_1 = f_1 N_L$  where  $N_L$  is the total population of the lower laser manifold [25], [26].

The modelling of quasi-three-level laser behaviour will start with the rate equations for the population inversion and the photon density in the laser cavity in the steady state.

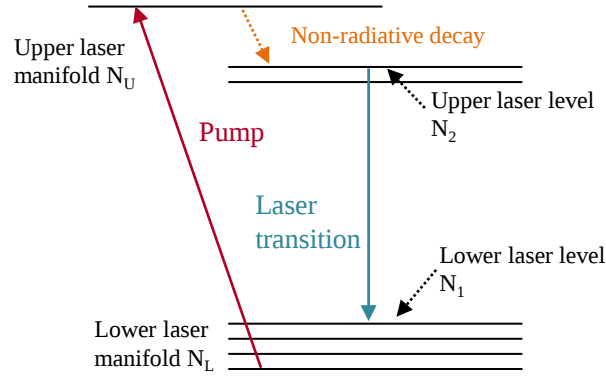


Figure 5.4 Energy level diagram of a typical quasi-three-level laser.

The laser rate equations for the population density in the upper and lower manifold can be described, if the depletion of the population of the ground state is neglected by [27]

$$\frac{dN_2(x, y, z)}{dt} = f_2 R r_p(x, y, z) - \frac{N_2(x, y, z) - N_2^0}{\tau} - \frac{f_2 c \sigma [N_2(x, y, z) - N_1(x, y, z)]}{n} \Phi \Phi_0(x, y, z) = 0 \quad (5.7)$$

$$\frac{dN_1(x, y, z)}{dt} = -f_1 R r_p(x, y, z) - \frac{N_1(x, y, z) - N_1^0}{\tau} + \frac{f_1 c \sigma [N_2(x, y, z) - N_1(x, y, z)]}{n} \Phi \Phi_0(x, y, z) = 0 \quad (5.8)$$

Therefore the rate equation describing the change in population inversion density with time in the steady state,  $\Delta N = N_2 - N_1$  can be determined by combining equations (5.8) and (5.7), giving

$$\frac{d\Delta N(x, y, z)}{dt} = (f_1 + f_2) R r_p(x, y, z) - \frac{\Delta N(x, y, z) - \Delta N^0}{\tau} - \frac{(f_1 + f_2) c \sigma \Delta N(x, y, z)}{n} \Phi \Phi_0(x, y, z) = 0 \quad (5.9)$$

where  $c$  is the speed of light in a vacuum,  $\tau$  is the life-time of the upper manifold,  $\sigma$  is the gain cross-section of the laser,  $\Delta N^0 = N_2^0 - N_1^0$  is the unpumped population inversion density and  $n$  is the refractive index of the laser material. The spatial distribution of the pump energy and laser energy is given by  $r_p(x, y, z)$  and  $\Phi_0(x, y, z)$  respectively, which is normalised such that

$$\iiint r_p(x, y, z) dV = \iiint \Phi_0(x, y, z) dV = 1 \quad (5.10)$$

$R$  is the rate at which the ions are excited into the upper laser manifold by the pumping process and is given by

$$R = \frac{P_p \eta_a}{h\nu_p} \quad (5.11)$$

where  $P_p$  is the incident pump power,  $\nu_p$  is the frequency of the pump,  $h$  is Planck's constant,  $\eta_a = (1 - e^{-\alpha_p l})$  is the fraction of incident pump power absorbed by the laser material with a length  $l$  and absorption coefficient  $\alpha_p$  at the pump frequency. The pump process is assumed to have unity quantum efficiency. In the cavity, the total number of laser photons,  $\Phi$  is given by

$$\Phi = \frac{2nlP_L}{ch\nu_L} \quad (5.12)$$

where  $P_L$  is the laser power travelling in one direction inside the cavity, and  $\nu_L$  is the laser frequency.

At thermal equilibrium  $N_1^0 \gg N_2^0$ , the population inversion can be found by rearranging equation (5.9) and replacing  $\Delta N^0$  by  $-N_1^0$ , giving

$$\Delta N(x, y, z) = \frac{\tau f R r_p(x, y, z) - N_1^0}{1 + \frac{c\sigma\tau}{n} f \Phi \phi_0(x, y, z)} \quad (5.13)$$

where  $f = f_1 + f_2$  has been used for notational compactness.

The increase in the one-way intensity  $I(x, y, z)$  of the laser beam as it propagates through the gain medium is given by

$$\frac{dI(x, y, z)}{dz} = G(x, y, z)I(x, y, z) \quad (5.14)$$

where  $I(x, y, z) = (ch\nu_L/2n)\Phi\phi_0(x, y, z)$  and  $G(x, y, z)$  is the gain of laser and is obtained by multiplying the gain cross-section,  $\sigma$  with equation (5.14), giving  $G(x, y, z) = \Delta N(x, y, z)\sigma$ .

If the losses in the cavity are small, the condition that the round-trip loss equals round-trip gain in the cavity can be written as

$$\int_{\text{roundtrip}} dP_L(z) = 2 \int_0^l \frac{dP_L(z)}{dz} dz = P_L(\delta_i) \quad (5.15)$$

where  $\delta_i$  is the round-trip loss of the laser cavity excluding any mirror losses, described by equations (5.23)-(5.26).  $P_L(z)$  is the single-pass intra-cavity power at a distance  $z$  and is found by integration

$$P_L(z) = \int_{-\infty}^{\infty} \int_{-\infty}^{\infty} I(x, y, z) dx dy \quad (5.16)$$

while differentiation of equation (5.16) with respect to  $z$  leads to

$$\frac{dP_L(z)}{dz} = \int_{-\infty}^{\infty} \int_{-\infty}^{\infty} \frac{dI(x, y, z)}{dz} dx dy \quad (5.17)$$

Combining equations (5.14), (5.15) and (5.17)

$$2 \int_0^l \int_{-\infty}^{\infty} \int_{-\infty}^{\infty} G(x, y, z) I(x, y, z) dx dy dz = P_L(\delta_i) \quad (5.18)$$

The normalised laser and pump distributions for spot sizes of the propagating laser and pump beams are expressed as

$$r_p(x, y, z) = \frac{2\alpha_p}{\eta_a \pi w_{Px} w_{Py}} e^{\left(\frac{-2x^2}{w_{Px}^2}\right)} e^{\left(\frac{-2y^2}{w_{Py}^2}\right)} e^{(-\alpha_p z)} \quad (5.19)$$

$$\phi_0(x, y, z) = \frac{2}{\pi w_{Lx} w_{Ly} l} e^{\left(\frac{-2x^2}{w_{Lx}^2}\right)} e^{\left(\frac{-2y^2}{w_{Ly}^2}\right)} \quad (5.20)$$

where,  $w_{L(x,y)}$  are the  $1/e^2$  spot sizes of the laser beam in the vertical ( $x$ ) and horizontal ( $y$ ) directions respectively and,  $w_{P(x,y)}$  are the  $1/e^2$  spot sizes of the pump beam in the vertical ( $x$ ) and horizontal ( $y$ ) directions. The threshold power,  $P_{th}$  is the minimum pump power required to achieve lasing and is evaluated by setting the output power to ( $P_L =$ ) 0 and the pump power, to ( $P_p =$ )  $P_{th}$ . By rewriting (5.18) using  $\Delta N(x, y, z)$  from equation (5.13) and with the expressions for the gain,  $G(x, y, z)$  and intensity  $I(x, y, z)$  in terms of the pump and laser beam waists,  $P_{th}$  can be expressed as [25]

$$P_{th} = \frac{\pi h \nu_p}{4 \sigma f \tau \eta_a} (\delta_i + 2 \sigma N_1^0 l) \sqrt{w_{Lx}^2 + w_{Px}^2} \sqrt{w_{Ly}^2 + w_{Py}^2} \quad (5.21)$$

It can be seen that a low threshold power,  $P_{th}$  can be achieved by increasing the gain cross-section ( $\sigma$ ) and life-time ( $\tau$ ), which is fixed for a particular gain material. The laser threshold can also be lowered by reducing the propagation loss of the gain medium which will reduce the overall round-trip cavity loss and by reducing mode sizes of the pump and lasers beams. Careful design consideration of the geometric shape of a channel waveguide can reduce the size of the propagating modes for the pump and laser beam propagating in the waveguide. The spectroscopic properties of Yb:Ta<sub>2</sub>O<sub>5</sub> waveguide established in Chapter 4 was used to plot the theoretical laser threshold power vs. length of the cavity using equation (5.21). For this laser system with following spectroscopic

properties, waveguide dimensions and cavity configuration; a pump wavelength of 977 nm, emission cross-sections of  $\sigma_{em} = 2.90 \pm 0.7 \times 10^{-20} \text{ cm}^2$ , excited-state lifetime  $\tau = 0.25 \pm 0.03 \text{ ms}$ , an absorption coefficient  $\alpha_p = N_T \sigma_{abs}$  where the total Yb ion concentration  $N_T = 6.2 \times 10^{20} \text{ cm}^{-3}$  and  $\sigma_{abs} = 2.75 \pm 0.2 \times 10^{-20} \text{ cm}^2$ , the population fraction in the lower and upper laser manifold population is  $f = f_1 + f_2 = 1$ , spot sizes of the pump and laser beam in the horizontal direction  $w_{Lx} = w_{Px} = 1.77 \text{ }\mu\text{m}$  and vertical direction  $w_{Ly} = w_{Py} = 0.51 \text{ }\mu\text{m}$  for a 5.4  $\mu\text{m}$  wide waveguide and cavity formed from a HR mirror and 10% OC, the laser threshold is shown in figure 5.5.

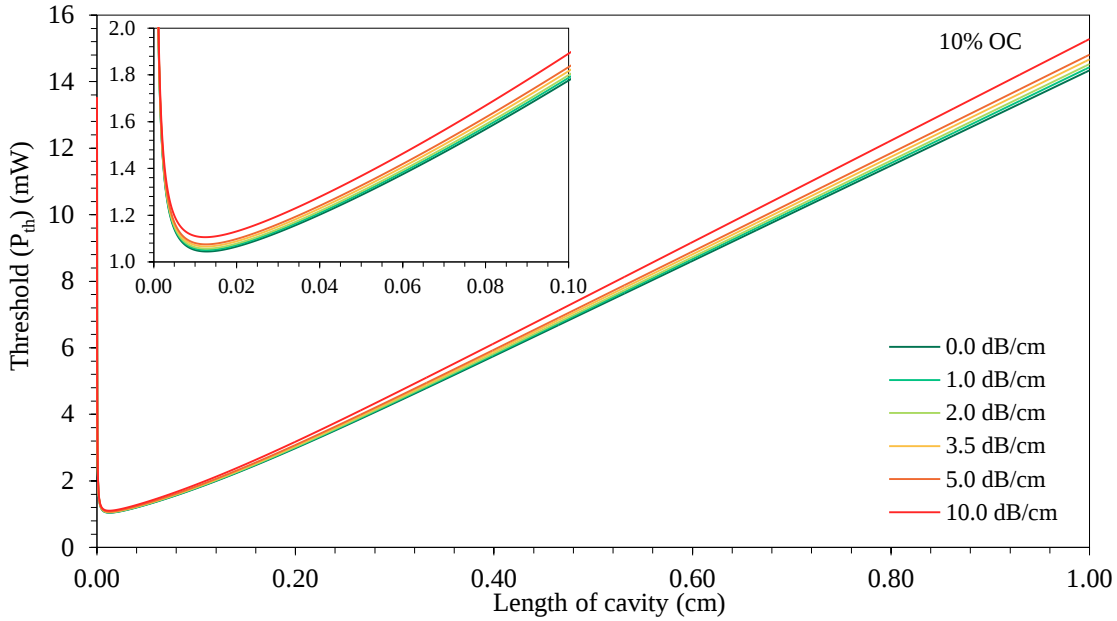


Figure 5.5 Theoretical laser threshold vs. cavity length for cavity with a HR mirror and 10% OC, with zoomed in insert.

From the theoretical laser threshold plot, the lowest threshold power that can be obtained for a this laser system is with cavity with a length of  $\approx 0.15 \text{ mm}$ . As expected an increase in the propagation loss of the waveguide increases the power required for lasing to occur, but this increase in laser threshold is shown to be small with an increase of  $\approx 0.06 \text{ mW}$  at minimum threshold. For longer waveguides, the threshold increases in approximately linear fashion as the propagation loss increases and the reabsorption loss ( $2\sigma N_1^0 l$ ) begins to influence the total cavity loss more.

Another important parameter used to measure the performance of a laser is the slope efficiency ( $\eta_{sl}$ ) which describes how efficiently the pump power is converted to laser power after threshold has been reached. The slope efficiency is the gradient of a plot of the laser output power with respect to input pump power, hence can be evaluated experimentally. The slope efficiency can also be evaluated numerically and used to calculate the theoretical single end slope efficiency of a laser system, described by [28]

$$\eta_{sl} = \eta_p \frac{\gamma_1 \nu_l}{\delta_i \nu_p} \quad (5.22)$$

where  $\nu_l$  and  $\nu_p$  are the lasing and pump frequencies,  $\eta_p$  is the fractional pump power contained in the active region (considered unity in this case), and  $\delta_i$  is the round-trip loss of the laser cavity described by

$$\delta_i = \gamma_i + \gamma_1 + \gamma_2 \quad (5.23)$$

This round-trip loss is the sum of the logarithmic internal round-trip cavity loss,  $\gamma_i$  and logarithmic losses of the two cavity mirrors,  $\gamma_1$  and  $\gamma_2$  given by

$$\gamma_i = -2[\ln(1 - a) + \ln(1 - L_i)] \quad (5.24)$$

$$\gamma_1 = -\ln(1 - T_1) \quad (5.25)$$

$$\gamma_2 = -\ln(1 - T_2) \quad (5.26)$$

where  $T_1$  is the transmission of the output mirror,  $T_2$  is the transmission of the input mirror,  $L_i$  is the linear loss of cavity, and  $a$  is the fractional mirror loss which is assumed negligible. For a waveguide laser with a pump wavelength of 977 nm and centre laser emission at 1025 nm, the theoretical slope efficiency with respect to the output coupler transmission is shown by figure 5.6 for different propagation loss, assuming a high reflective (99.99%) input mirror and 100% pump power contained in the active medium. The slope efficiency is seen to increase with output coupler transmission, with higher propagation loss causing the overall sloped to reduce.

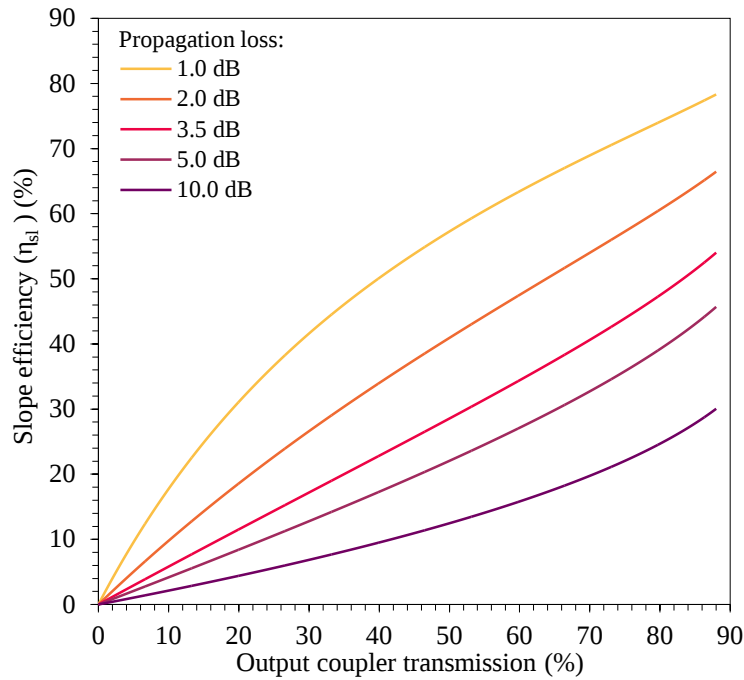


Figure 5.6 Theoretical laser slope efficiency vs. output coupler transmission for various propagation losses.

### 5.3 Experimental set-up for waveguide laser performance characterisation

Lasing was demonstrated by launching a free space collimated laser beam at 977 nm from a Bragg grating stabilized laser source into an end-facet of a waveguide using an aspheric lens (NA = 0.68). The light emerging from the output end was collected using another aspheric lens (NA = 0.68) and passed through a set of long pass filters with a cut-off wavelength of 1000 nm to remove the residual pump radiation. For calculation of the lasing threshold and slope efficiency, a germanium photo-detector (Newport 918-IR) was used to acquire the output power with respect to the pump power, with and without the long pass filters so that the absorbed pump can be extracted.

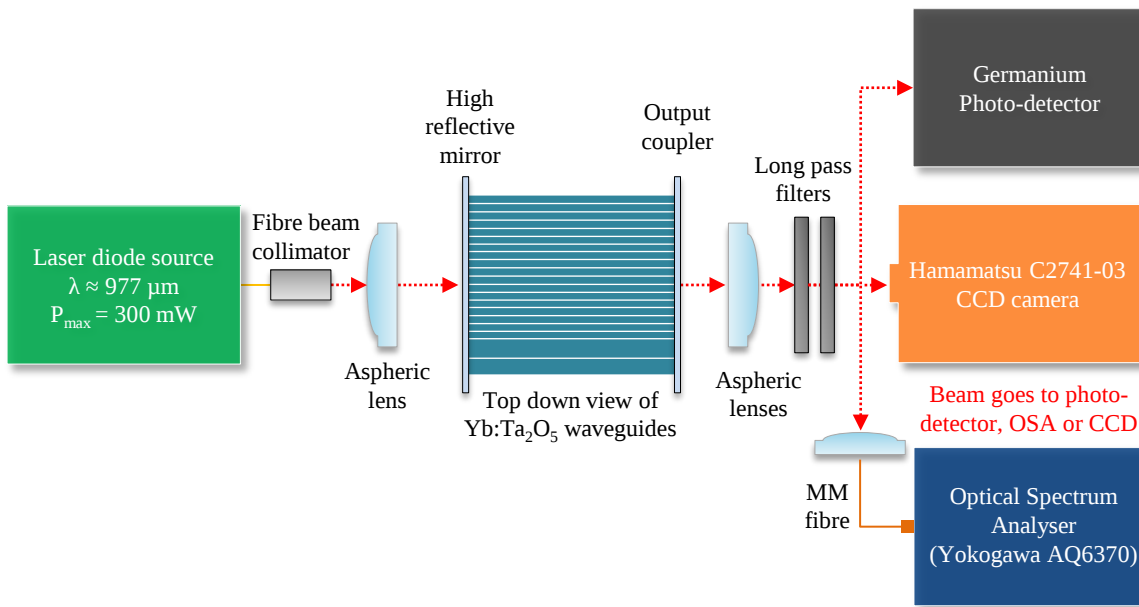


Figure 5.7 Experimental set-up for laser characterization of Yb:Ta<sub>2</sub>O<sub>5</sub> with high reflector (HR) mirror and output coupler (OC) with top down view of waveguide device.

For measuring the laser spectrum filtered output light was focused with another aspheric lens into a MM fibre connected to an OSA. The mode intensity profiles of the lasing mode were also imaged with Hamamatsu C2741-03 CCD with the experimental set-up is shown in figure 5.7.

#### 5.3.1 Determination of launch efficiency of experimental set-up

Experimental determination of the laser slope efficiency and pump power threshold with respect to launched pump power for comparison with theoretical estimation requires a good estimate of the launched pump power. In the case of a rib waveguide with a focused pump beam from a lens, the launch pump power can be estimated from the spatial overlap of the pump laser beam with the fundamental mode of the waveguide. It is therefore important to determine the spot size of the pump beam near the focus of the input lens so that an estimate of the launched power can be made.

A quick and accurate method used to determine the cross-sectional parameters of a laser beam is the knife edge method, which consists of a knife edge translated in a direction perpendicular to that of the propagating beam as shown in figure 5.8. As the blade moves across the beam, the total

power,  $P_T$  detected by a power meter will show a reduction of power until the total power detected has reached a minimum, the position where the blade covers essentially the whole beam.

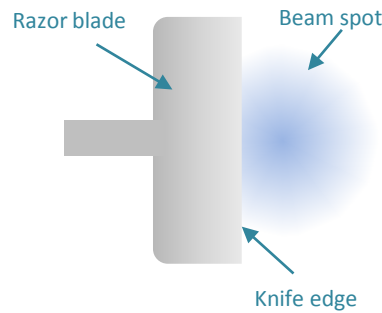


Figure 5.8 Razor edge of a blade moving across a beam.

A plot of the total power against the blade's position will lead to an S-shaped curve, figure 5.9b. The beam waist can be found from the S-shaped curve by either fitting a Gaussian error function on to the curve, or by integrating it giving a Gaussian beam profile which can be then used to find the waist at  $1/e^2$ .

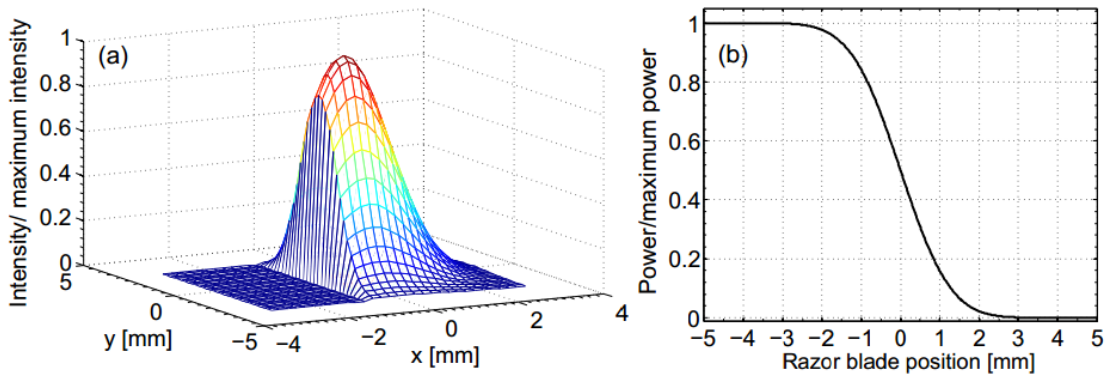


Figure 5.9a) 3D Gaussian beam distribution with partial beam coverage, b) optical power vs. position of the razor blade [29].

The experimental procedure for measuring the transmitted power vs. position of the razor in the  $x$  plane uses the apparatus shown in figure 5.10. A circularly collimated Gaussian beam from the laser diode at a wavelength of 977 nm is launched into an aspheric lens (C330-B-MT) which is used to focus light into the end of rib waveguide. The accurate positioning of the knife edge was made using a 3-axis NanoMax stage with manual differential micro-meter (Thorlabs), with an accuracy of 1  $\mu\text{m}$ . Another aspheric lens (C330-B-MT) was used to collect the covered light and guide the beam into a germanium photo-detector (Newport 918-IR). Measurements were carried out for different positions in the  $z$  axis so the development of the beam waist as it propagates through air can be mapped.

The knife edge method was in practice carried out directly after lasing characterisation without disturbing the input lens and laser diode collimator to find the beam profile launched into the waveguide.

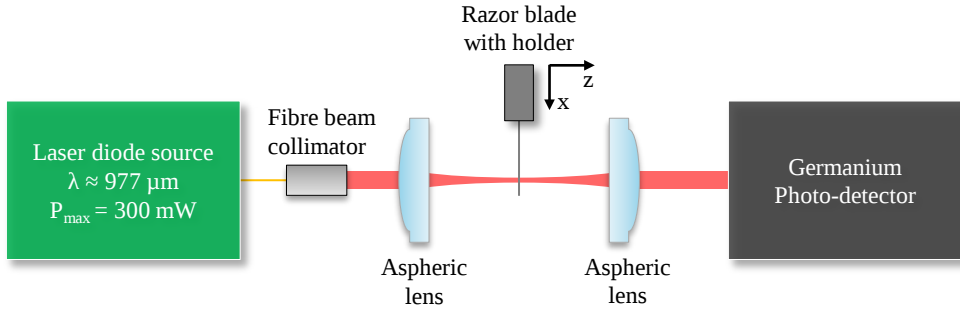


Figure 5.10 Experimental set-up for knife edge method with the razor blade moving across the investigated beam in the  $x$  axis for different positions from the lens along the  $z$  axis.

To characterize the intensity profiles of a Gaussian beam from the data collected, a complementary error function was fitted to the data to evaluate the beam radius using [30]

$$P = \frac{P_0}{2} \operatorname{erfc}\left(\frac{\sqrt{2}x + c}{w}\right) \quad (5.27)$$

where  $c$  is the displacement S-shaped curve in the  $x$  direction,  $P_0$  is the initial power of the beam and  $w$  is the  $1/e^2$  radius of the Gaussian beam. The derivation showing that transmitted power vs. position of the razor blade across the beam can be described by equation (5.27) is shown in Appendix B. Figure 5.11 shows the complementary error fit for the data of a razor edge at a position of 2 mm from the lens, with measurements taken at 10  $\mu\text{m}$  intervals. From the fit, a  $1/e^2$  beam radius of 115  $\mu\text{m}$  was found. Scans were carried out at different distances from the lens, with the fitted  $1/e^2$  beam radius for each scans given in table 5.1.

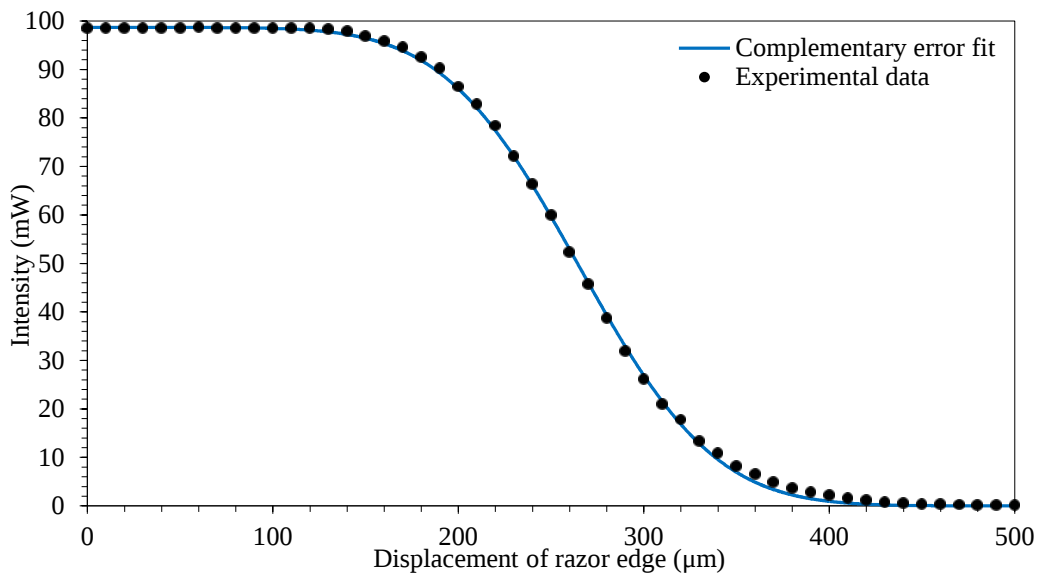


Figure 5.11 Complementary error function fit for knife edge scan of beam at a  $z = 2.0$  mm giving a  $1/e^2$  radius of 115  $\mu\text{m}$ .

Position of beam from lens, z (mm)	Variables		
	$P_0$ (mW)	$c$ ( $\mu\text{m}$ )	$w$ ( $\mu\text{m}$ )
0.50	98.02	-1108.00	540.00
1.00	98.39	-980.80	331.20
1.25	99.77	-562.10	228.90
1.50	98.60	-832.80	112.10
1.60	98.89	-202.90	73.84
1.70	99.72	-71.39	28.57
1.80	99.71	-39.32	7.20
2.00	98.67	-658.60	115.00
2.50	98.46	-744.90	350.60
3.00	98.12	-1233.00	591.00

Table 5.1 Values established from complementary error function fit.

Assuming that lasing with lowest incident pump power threshold occurs when pump radiation being fired into the end-facet of the waveguide is at the minimum beam waist, the corresponding maximum coupling efficiency can be calculated. To find the minimum beam waist of the focused pump beam, a Gaussian beam waist fit using equation (5.28) was applied to the data from table 5.1 of beam waists found using complementary error function fit with respect to the distance of propagation as shown in figure 5.12.

$$w = w_0 \sqrt{1 + \left( \frac{\lambda(z + a)}{\pi w_0^2} \right)^2} \quad (5.28)$$

Equation (5.28) was used to fit the Gaussian beam waist where  $\lambda$  is the pump wavelength ( $\lambda = 977$  nm),  $z$  is the distance along the propagation path,  $a$  is the offset in the  $z$  direction and  $w_0$  is the  $1/e^2$  minimum beam radius. From the measurements of the beam waist using the knife edge experiment,

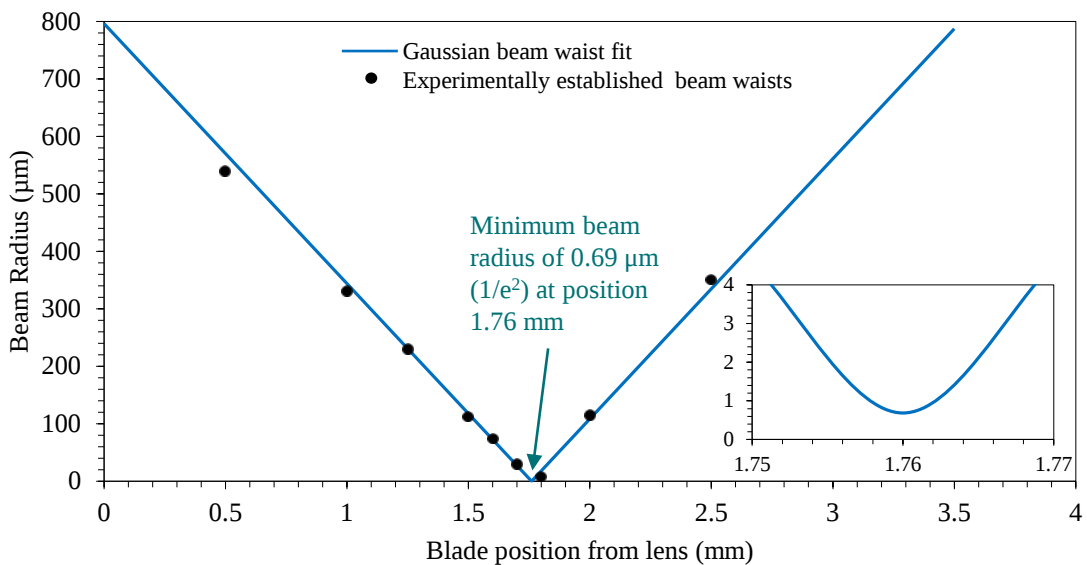


Figure 5.12 Gaussian beam waist fit of beam radius ( $1/e^2$ ),  $w$  found from the complementary error function fit as shown in table 5.1. Insert showing zoom in section at minimum beam radius.

a minimum beam radius was estimated from the Gaussian beam waist fit, shown in figure 5.12, to be  $w_0 = 0.69 \mu\text{m}$  at  $1/e^2$ . This gives a minimum beam waist of  $w_0 = 0.81 \mu\text{m}$  at FWHM in the x and y directions, assuming the collimated beam is circular. The coupling efficiency for the pump laser diode ( $\lambda = 977 \text{ nm}$ ) was calculated using the theoretical model discussed in section 3.5.1.1. Figure 5.13 is a plot of the coupling efficiency with respect to the position of the minimum beam waist at the waveguide end-facet for different rib widths. The theoretical model used the electric field waists of the waveguide's fundamental mode with radiation propagating at a wavelength of 980 nm found from COMSOL simulations discussed in section 2.4. From figure 5.13 it can be seen that the coupling efficiency shows a decreasing trend as the distance between the point of focus of the pump beam and end-facet is increased.

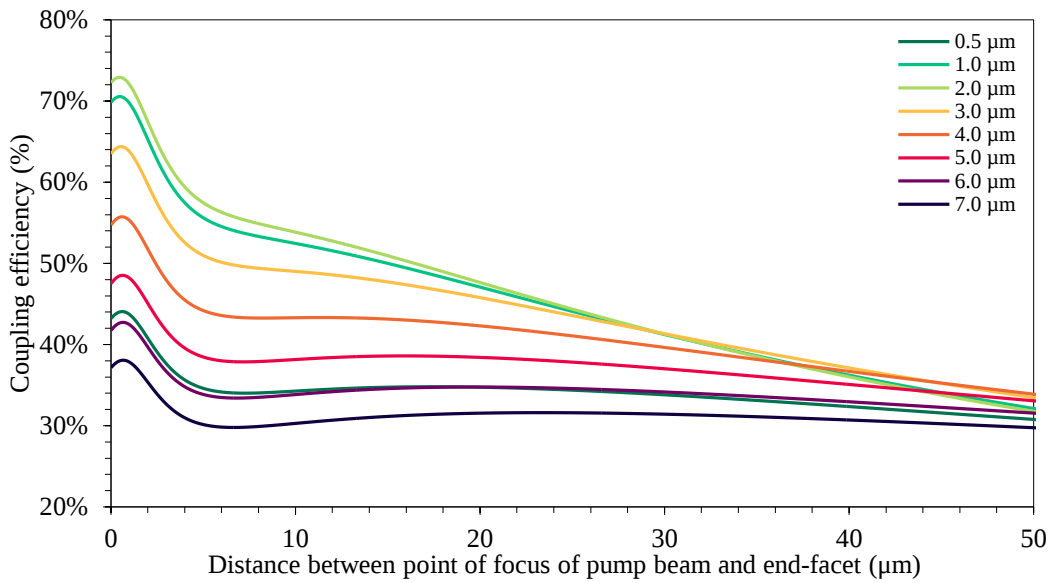


Figure 5.13 Theoretical model of coupling efficiency between 980 nm input laser beam (FWHM of mode intensity profile,  $w_0 = 0.81 \mu\text{m}$ ) and electric field profiles of rib waveguide found with COMSOL simulations.

Assuming that the pump beam is at its estimated minimum beam waist ( $w_0 = 0.81 \mu\text{m}$  at FWHM where  $z \approx 0$ ) at the end-facets of the waveguides, the maximum coupling efficiencies for different rib widths can be calculated. Figure 5.14 shows the coupling efficiency for various rib widths at distance  $z \approx 0$  between the point of focus of the pump beam and end-facet. The largest coupling efficiency of nearly 75% occurred for a rib width of  $\approx 1.4 \mu\text{m}$ ; as the width of the rib increases or decreases from the rib width of  $\approx 1.4 \mu\text{m}$ , the modal spot size increases in the horizontal direction, matching the pump spot size less well and causing a decrease in coupling efficiency.

The measurements for the lasing performance in the characterisation section were carried out on a waveguide with a width of 5.4. Calculation of the pump launch system coupling efficiencies and assuming lasing occurs at the beam waist of the focused pump beam, led to an estimated pump launch efficiency of 46%.

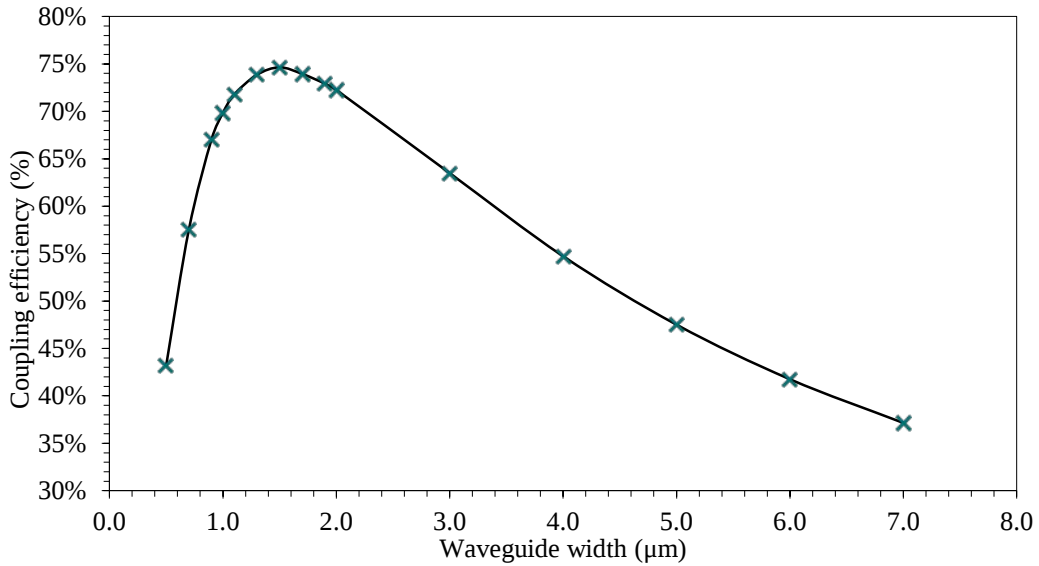


Figure 5.14 Maximum coupling efficiencies for different rib widths when minimum beam waist of the 980 nm laser focused with aspheric lens is at position  $z \approx 0$  mm (minimum beam waist) from the waveguide end-facet.

#### 5.4 Continuous wave laser performance

A 10.8 mm long waveguide chip with parallel optically polished end-facets was used for laser measurements. Initially, the laser cavity was formed by reflections from the end-facets alone. The waveguide-air interfaces were estimated to have Fresnel reflectivity of 12%. Subsequently, mirrors were end-butteted to the waveguides and held in place by surface tension between the mirror and waveguide end-facet using fluorinert (FC-70, Sigma Aldrich). The waveguide laser output power and residual pump power of a waveguide with a width of 5.4 μm was measured with respect to the incident pump power for different mirror and end-facet combinations. Observation of the near-field mode intensity profile at the pump wavelength at the waveguide output was used to ensure efficient pump coupling into the waveguide fundamental mode. The mode intensity profiles for a 5.4 μm wide waveguide laser with and without long pass filters are shown in figure 5.15.

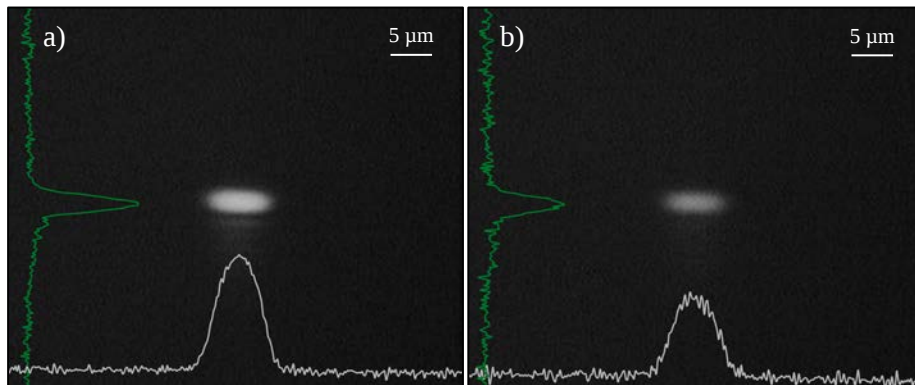


Figure 5.15 Mode intensity profiles for 5.4 μm wide waveguide of a) both the pump and lasing wavelengths, and b) only the lasing wavelength. Image taken with Hamamatsu C2741-03 camera with 40x microscope objective collection lens.

To deduce the estimated absorbed pump power for the laser performance characterization two sets of measurements of the output light were carried out. The first data set consisted of the lasing

power alone with the residual pump power filtered out,  $P_L$ . The second set was the residual pump power as well as the lasing power (removal of pump filter),  $P_T$ . Subtracting  $P_L$  from  $P_T$  will give the absorbed pump power,  $P_a$ . These measurements in combination with the estimated pump launch efficiency gave an allowed determination of the laser output power with respect to the absorbed pump power.

Figure 5.16 shows the laser output power with respect to the absorbed pump power for four different mirror configurations. Figure 5.16a shows the case with the output facet being simply the polished end while the input facet is either the polished end or an (HR) reflector with reflectivity >99.9% at the lasing wavelength. Figure 5.16b shows the case where the input facet has an HR mirror affixed, while the output coupler (OC) is either 5% or 10% (compared with 88% transmission for a bare end facet). The lasing thresholds,  $P_{th}$ , and slope efficiencies,  $\eta_{sl}$ , extracted from figure 5.16 are shown in table 5.2.

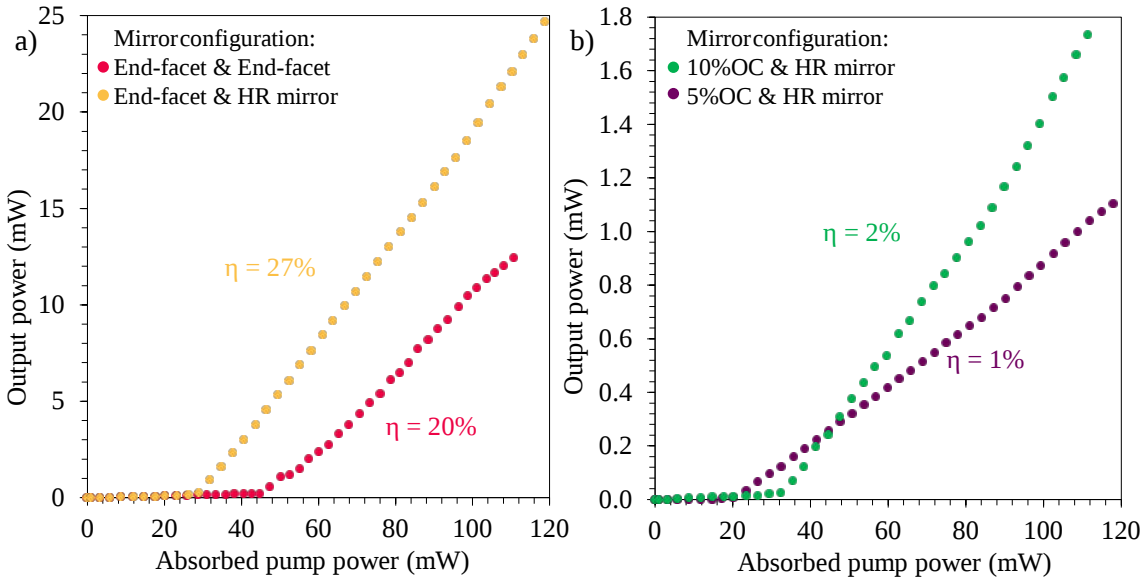


Figure 5.16 Laser output power vs absorbed pump power plotted for different mirror configurations with calculated coupling efficiency of 44%. Mirror configurations used: a) EF/EF & EF/HR, b) 10%OC/HR & 5%OC/HR.

The highest single-ended output power and slope efficiency of  $\approx 25$  mW and  $\approx 26\%$  respectively were found to be from the cavity formed from an HR mirror and end-facet of the waveguide, with the highest single-ended output power limited by the maximum input pump power from the LD.

Mirror configuration	Threshold (mW), $P_{th}$		Slope efficiency (%), $\eta_{sl}$	
	Experimental	Theoretical	Experimental	Theoretical
EF/EF	$47 \pm 2.0$	17.35	$19 \pm 1.0\%$	32
EF/HR	$30 \pm 1.5$	16.91	$26 \pm 1.5\%$	47
10% OC/HR	$35 \pm 1.5$	16.50	$2 \pm 0.1\%$	4
5% OC/HR	$22 \pm 1.0$	16.49	$1 \pm 0.1\%$	2

Table 5.2 Laser parameters for different mirror configurations established experimentally and estimated theoretically.

The slope efficiencies measured are systematically lower than predicted by equation (5.22), as well as the measured laser thresholds higher than predicted by equation (5.22). The reduced slope

efficiencies and increased laser threshold may be a combination of i) the estimate of absorbed pump power assumes perfect alignment of a pump beam with a very small waveguide mode, ii) pump loss competing with pump absorption, or iii) non-unity quantum efficiency. In addition losses introduced by the mirrors affixed at the end-facets as a result of damaged and misalignment can cause the increase of threshold and reduction of slope efficiency.

## 5.5 Yb:Ta<sub>2</sub>O<sub>5</sub> laser spectrum

The Yb:Ta<sub>2</sub>O<sub>5</sub> waveguide laser output spectrum just below and above threshold for a cavity formed with a HR mirror and a 5% OC of a waveguide width of 5.4  $\mu\text{m}$  is shown in Figure 5.17. The lasing peaks occur within this waveguide between wavelengths of 1015 nm and 1030 nm, which is not unexpected as this is within the emission fluorescence bandwidth shown in Chapter 4.

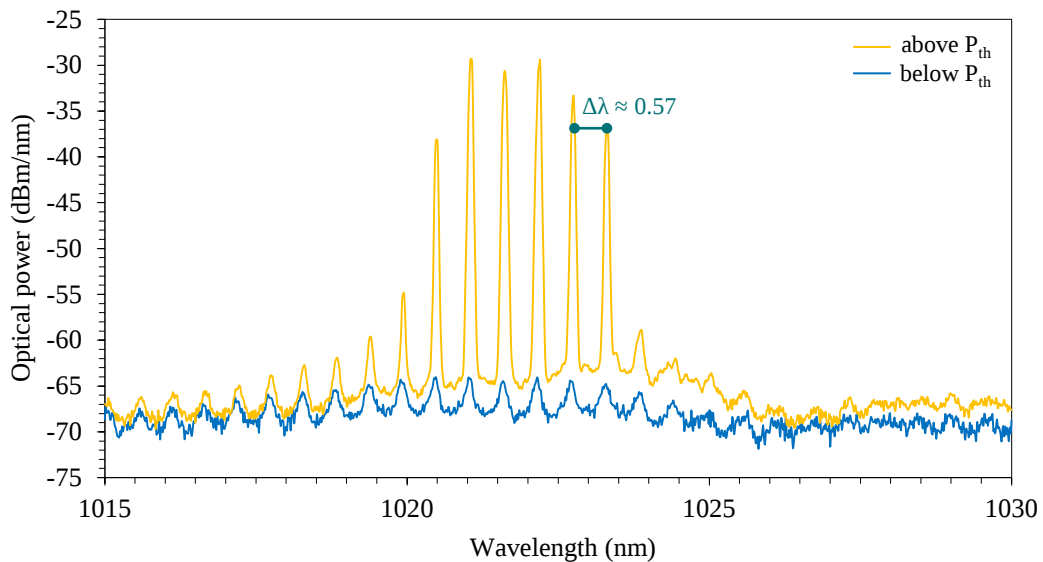


Figure 5.17 Lasing spectrum of Yb:Ta<sub>2</sub>O<sub>5</sub> waveguide with a width of 5.4  $\mu\text{m}$ , focusing around region lasing occurs with lasing spectrum development just below (blue) and above (yellow) threshold for cavity formed with a HR mirror and 5% OC.

Further spectral measurements were carried out in addition to the 5.4  $\mu\text{m}$  wide waveguide, for rib widths of 4  $\mu\text{m}$ , 6  $\mu\text{m}$ , 7  $\mu\text{m}$ , 8  $\mu\text{m}$  and 9  $\mu\text{m}$  of laser waveguide cavities formed with a HR and 5% OC. The spectra are shown in figure 5.18 and illustrate the development of the lasing wavelength with respect to the width of the rib. For the waveguide with a rib width of 4  $\mu\text{m}$  (Figure 5.18a) lasing occurred between 1010 – 1020 nm with the peaks seen at irregular spectral intervals unlike that seen in figure 5.17. Figure 5.18c, d, and e show the lasing spectrum for widths of 6  $\mu\text{m}$ , 7  $\mu\text{m}$ , and 8  $\mu\text{m}$  where lasing occurs between 1025 – 1035 nm. The lasing peaks are similar to that seen for lasing of a waveguide with a rib 5.4  $\mu\text{m}$  wide where they have regular spectral intervals. The lasing wavelength region shifts to longer wavelengths at a rib width of 9  $\mu\text{m}$  with lasing now occurring at wavelengths between 1040 – 1050 nm.

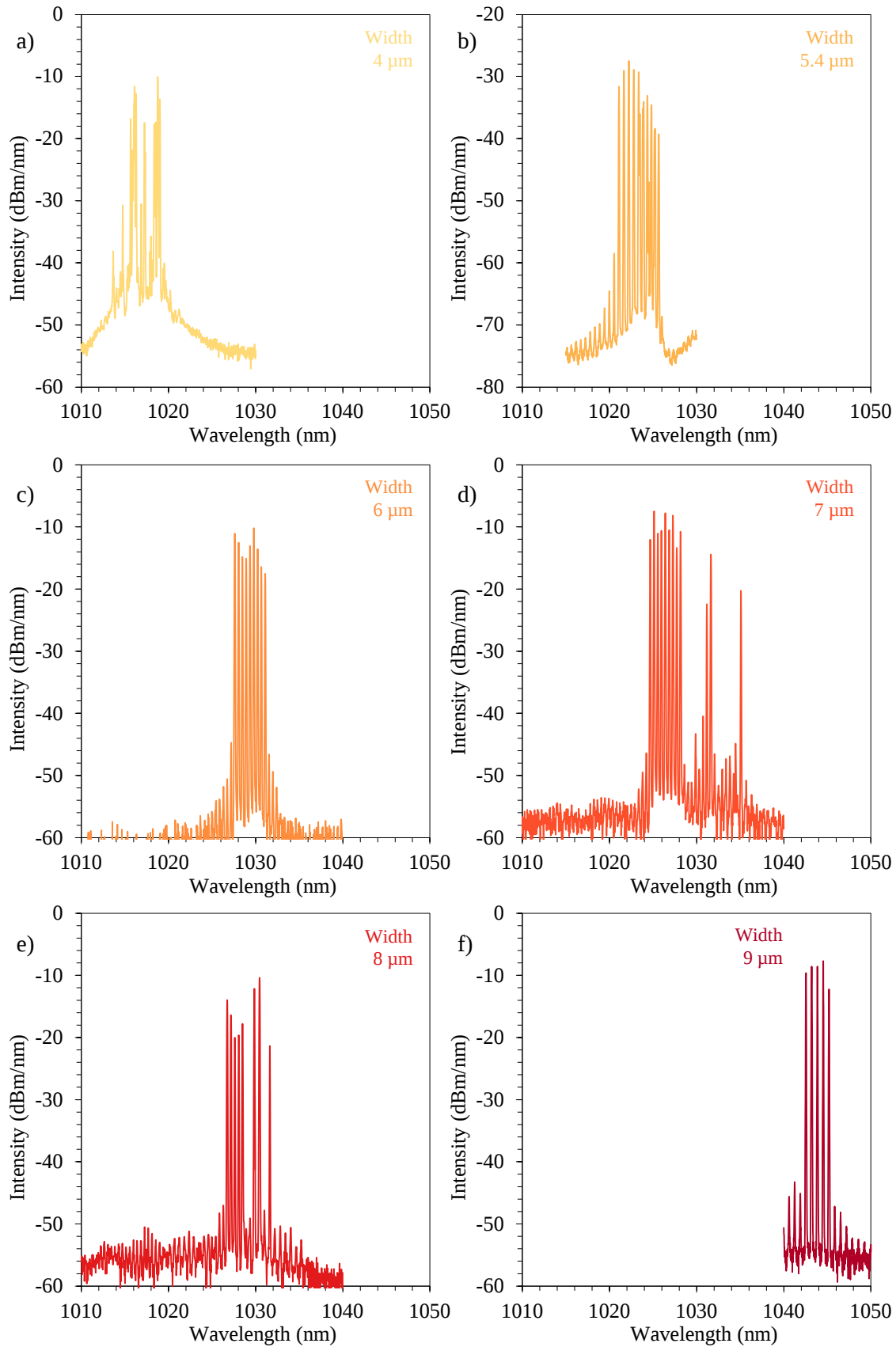


Figure 5.18 Lasing spectra for different width waveguides of a cavity formed from a HR mirror and 5% OC with waveguides widths of a) 4  $\mu\text{m}$ , b) 5.4  $\mu\text{m}$  (from figure 5.17), c) 6  $\mu\text{m}$ , d) 7  $\mu\text{m}$ , e) 8  $\mu\text{m}$ , & f) 9  $\mu\text{m}$ .

This centre wavelength shift with waveguide width occurs because as the rib waveguides increase in width, the number of supported modes propagating increases and have less interaction with the surface waveguide as the geometry of the core increases, reducing the propagation losses to a minimum at various wavelength regions forcing lasing operation to occur. Therefore due to the broad gain spectrum, shown in section 4.3 a wide range of lasing wavelengths can occur. Wavelength selection or tuning over a wide bandwidth can therefore be achieved with the introduction of adjustable intra-cavity losses.

The spectra shown in figure 5.18 ranging between 1010 nm to 1050 nm shows multiple lasing peaks occurring around the central wavelength which do not correspond with the peak separation of 0.023 nm associated with the length of the laser cavity, which were not fully resolved by the OSA at its best resolution of 0.02 nm. The optical path length (in air) which would correspond to the observed separation of the laser emission peaks is 0.89 mm. This behaviour is most likely due to modal beating in the waveguide which, for this width, is multimode at the emission wavelength.

## 5.6 Conclusion

Ta<sub>2</sub>O<sub>5</sub> rib waveguides doped with  $6.2 \times 10^{20}$  ions/cm<sup>3</sup> ytterbium ions were fabricated by RF magnetron sputtering from a powder-pressed target onto silicon wafer with thermally-grown silica under-cladding. Channels were etched into the core layer using a combination of conventional photolithography and argon ion beam milling, with an encapsulating SiO<sub>2</sub> over-cladding sputtered onto the Yb:Ta<sub>2</sub>O<sub>5</sub> to create a symmetrical waveguide. Integrated waveguide lasers in Yb:Ta<sub>2</sub>O<sub>5</sub> were demonstrated for the first time, using a 10.8 mm long chip and characterised for both mirrored and mirror-less cavities, with reflections occurring off the polished end-facets in the latter cases. To establish an accurate estimate of the absorbed pump, the pump launch efficiency was calculated using knife-edge experiments to measure the launched pump beam waist and overlap integrals of the pump beam waist and simulated mode intensity distribution. For a rib waveguide 5.4 μm wide lasing was observed between 1015 nm and 1030 nm when end-pumped with a 977 nm laser diode, leading to estimated 46% launch efficiency. The highest output power of 25 mW at a wavelength of 1025 nm was achieved with an absorbed pump power of 120 mW for a cavity formed by a high reflector mirror and an estimated 12% Fresnel reflection at the output. In this case, the absorbed pump power threshold and slope efficiency were measured to be  $\approx 30$  mW and  $\approx 26\%$  respectively. Tunability of lasing wavelength was demonstrated through tailoring the geometry of the rib waveguide by changing the width of the rib. This can lead to selection of a desired wavelength required for individual application. There is scope for improvement of the laser performance achieved in terms of optimization of length of the waveguide and concentration of the ytterbium ions in the waveguide, as well as reducing the propagation loss of the fabricated rib waveguides, therefore reducing the intra-cavity loss leading to higher slope efficiencies and lower thresholds.

Lasing in a waveguide system with a high index contrast between core ( $n_{\text{core}} \approx 2.124$ ) and cladding ( $n_{\text{clad}} \approx 1.46$ ) leads to tight confinement of the optical mode with low bend loss and coupled with demonstration of lasing with ytterbium rare-earth ions leads to great potential for mass-producible, integrated optical circuits on silicon using conventional CMOS fabrication technologies.

## 5.7 Bibliography

- [1] C. Florea and K. A. Winick, "Ytterbium-doped glass waveguide laser fabricated by ion exchange," *J. Light. Technol.*, vol. 17, no. 9, pp. 1593–1601, 1999.
- [2] M. Ams, P. Dekker, G. D. Marshall, and M. J. Withford, "Monolithic 100 mW Yb waveguide laser fabricated using the femtosecond-laser direct-write technique," *Opt. Lett.*, vol. 34, no. 3, pp. 247–249, 2009.
- [3] A. A. Lagatsky, A. Choudhary, P. Kannan, D. P. Shepherd, W. Sibbett, and C. T. A. Brown, "Fundamentally mode-locked, femtosecond waveguide oscillators with multi-gigahertz repetition frequencies up to 15 GHz," *Opt. Express*, vol. 21, no. 17, pp. 19608–14, 2013.
- [4] R. Mary, S. J. Beecher, G. Brown, R. R. Thomson, D. Jaque, S. Ohara, and A. K. Kar, "Compact, highly efficient ytterbium doped bismuthate glass waveguide laser," *Optics Letters*, vol. 37, no. 10, p. 1691, 2012.
- [5] E. H. Bernhardt, H. A. G. M. van Wolferen, K. Wörhoff, R. M. de Ridder, and M. Pollnau, "Highly efficient, low-threshold monolithic distributed-Bragg-reflector channel waveguide laser in Al<sub>2</sub>O<sub>3</sub>:Yb<sup>3+</sup>," *Opt. Lett.*, vol. 36, no. 5, pp. 603–605, 2011.
- [6] D. C. Hanna, J. K. Jones, A. C. Large, D. P. Shepherd, A. C. Tropper, P. J. Chandler, M. J. Rodman, P. D. Townsend, and L. Zhang, "Quasi-three level 1.03  $\mu\text{m}$  laser operation of a planar ion-implanted Yb:YAG waveguide," *Optics Communications*, vol. 99, no. 3–4, pp. 211–215, 1993.
- [7] J. Siebenmorgen, T. Calmano, K. Petermann, and G. Huber, "Highly efficient Yb:YAG channel waveguide laser written with a femtosecond-laser," *Opt. Express*, vol. 18, no. 15, pp. 16035–16041, 2010.
- [8] J. K. Jones, J. P. de Sandro, M. Hempstead, D. P. Shepherd, A. C. Large, A. C. Tropper, and J. S. Wilkinson, "Channel waveguide laser at 1  $\mu\text{m}$  in Yb-indiffused LiNbO<sub>3</sub>," *Optics Letters*, vol. 20, no. 13, p. 1477, 1995.
- [9] M. Fujimura, H. Tsuchimoto, and T. Suhara, "Yb-diffused LiNbO<sub>3</sub> annealed/proton-exchanged waveguide lasers," *IEEE Photonics Technol. Lett.*, vol. 17, no. 1, pp. 130–132, Jan. 2005.
- [10] D. Geskus, S. Aravazhi, E. Bernhardt, C. Grivas, S. Harkema, K. Hametner, D. Günther, K. Wörhoff, and M. Pollnau, "Low-threshold, highly efficient Gd<sup>3+</sup>, Lu<sup>3+</sup> co-doped KY(WO<sub>4</sub>)<sub>2</sub>:Yb<sup>3+</sup> planar waveguide lasers," *Laser Phys. Lett.*, vol. 6, no. 11, pp. 800–805, 2009.
- [11] F. M. Bain, A. A. Lagatsky, R. R. Thomson, N. D. Psaila, N. V Kuleshov, A. K. Kar, W. Sibbett, and C. T. A. Brown, "Ultrafast laser inscribed Yb:KGd(WO<sub>4</sub>)<sub>2</sub> and Yb:KY(WO<sub>4</sub>)<sub>2</sub> channel waveguide lasers," *Opt. Express*, vol. 17, no. 25, pp. 22417–22422, 2009.

- 
- [12] A. Choudhary, W. Bolaños, P. Kannan, J. J. Carvajal, M. Aguilò, F. Diaz, and D. P. Shepherd, "Low-threshold, mirrorless emission at 981 nm in an Yb,Gd,Lu:KYW inverted rib waveguide laser," in *Solid State Lasers XXII: Technology and Devices*, 2013, vol. 8599, p. 859905.
- [13] W. Bolaños, F. Starecki, A. Braud, J.-L. Doualan, R. Moncorgé, and P. Camy, "2.8 W end-pumped Yb<sup>3+</sup>:LiYF<sub>4</sub> waveguide laser," *Opt. Lett.*, vol. 38, no. 24, pp. 5377–80, 2013.
- [14] A. Aghajani, G. S. Murugan, N. P. Sessions, S. J. Pearce, V. Apostolopoulos, and J. S. Wilkinson, "Spectroscopy of ytterbium-doped tantalum pentoxide rib waveguides on silicon," *Opt. Mater. Express*, vol. 4, no. 8, p. 1505, 2014.
- [15] B. Unal, M. C. Netti, M. A. Hassan, P. J. Ayliffe, M. D. B. Charlton, F. Lahoz, N. M. B. Perney, D. P. Shepherd, Chao-Yi Tai, J. S. Wilkinson, and G. J. Parker, "Neodymium-doped tantalum pentoxide waveguide lasers," *IEEE J. Quantum Electron.*, vol. 41, no. 12, pp. 1565–1573, Dec. 2005.
- [16] A. Z. Subramani, C. J. Oton, D. P. Shepherd, and J. S. Wilkinson, "Erbium-doped waveguide laser in tantalum pentoxide," *IEEE Photonics Technol. Lett.*, vol. 22, no. 21, pp. 1571–1573, Nov. 2010.
- [17] C. Chaneliere, J. L. Autran, R. a. B. Devine, and B. Balland, "Tantalum pentoxide (Ta<sub>2</sub>O<sub>5</sub>) thin films for advanced dielectric applications," *Mater. Sci. Eng. R Reports*, vol. 22, no. 6, pp. 269–322, 1998.
- [18] C.-Y. Tai, J. Wilkinson, N. Perney, M. Netti, F. Cattaneo, C. Finlayson, and J. Baumberg, "Determination of nonlinear refractive index in a Ta<sub>2</sub>O<sub>5</sub> rib waveguide using self-phase modulation," *Opt. Express*, vol. 12, no. 21, pp. 5110–5116, 2004.
- [19] A. Subramanian, "Tantalum pentoxide waveguide amplifier and laser for planar lightwave circuits," Ph.D. Thesis, University of Southampton, U.K., 2011.
- [20] O. Svelto, *Principles of Lasers*, 5th ed. Springer US, 2010.
- [21] R. C. Hilborn, "Einstein coefficients, cross sections, f values, dipole moments, and all that," *Am. J. Phys.*, vol. 50, no. 11, p. 982, 1982.
- [22] A. E. Siegman, *Lasers*. University Science Books, 1990.
- [23] W. T. Silfvast, *Laser fundamentals*, 2nd Edit. Cambridge: Cambridge University Press, 2004.
- [24] W. Koechner, *Solid-state laser engineering*, vol. 1. New York, NY: Springer New York, 2006.
- [25] W. P. Risk, "Modeling of longitudinally pumped solid-state lasers exhibiting reabsorption losses," *J. Opt. Soc. Am. B*, vol. 5, no. 7, p. 1412, Jul. 1988.
- [26] T. Taira, W. M. Tulloch, and R. L. Byer, "Modeling of quasi-three-level lasers and operation of cw Yb:YAG lasers," *Appl. Opt.*, vol. 36, no. 9, pp. 1867–1874, 1997.
- [27] T. Y. Fan and R. Byer, "Modeling and CW operation of a quasi-three-level 946 nm Nd:YAG laser," *IEEE J. Quantum Electron.*, vol. 23, no. 5, pp. 605–612, May 1987.

- [28] M. J. Digonnet and C. J. Gaeta, "Theoretical analysis of optical fiber laser amplifiers and oscillators," *Appl. Opt.*, vol. 24, no. 3, p. 333, 1985.
- [29] J. Westberg and A. Khodabakhsh, "Characterization of a Gaussian shaped laser beam: Lab, LL03." UMEA University, Department of Physics, 2014.
- [30] J. Magnes, D. Odera, J. Hartke, M. Fountain, L. Florence, and V. Davis, "Quantitative and qualitative study of gaussian beam visualization techniques," *Arxiv Prepr. physics/*, no. 2, pp. 1–5, 2006.

# CHAPTER 6

## Conclusion and Future Work

### 6.1 Conclusion

The work described in the thesis presents i) a numerical study of mode intensity profiles for different rib waveguides sizes in Ta<sub>2</sub>O<sub>5</sub> on silicon substrate, ii) a numerical feasibility study on the integrated planar Kerr lens elements for the potential of modelocking, iii) fabrication and spectroscopic characterisation of Yb:Ta<sub>2</sub>O<sub>5</sub> rib waveguides, and iv) experimental demonstration of lasing action in Yb:Ta<sub>2</sub>O<sub>5</sub> for the first time.

*Modelling of channel waveguides and devices in tantalum pentoxide:* A comprehensive numerical analysis of the mode profile behaviour for different rib waveguide designs were carried out using COMSOL multi-physics finite element analysis software. Symmetrical Ta<sub>2</sub>O<sub>5</sub> rib waveguides with a core thickness of 1 μm and SiO<sub>2</sub> cladding were investigated for mode profiles propagating with a wavelength of  $\lambda = 980$  nm, as it is close to range of the operating wavelength of the laser pump source  $\approx 977$  nm as well as close to the expect wavelength of a typical Yb-doped lasers. The simulations were implemented for rib etch depths of 150 nm, 300 nm, 500 nm, and full etch of 1 μm for rib widths from 0.3 μm to 20 μm. From the study it was found that for rib widths smaller than 1 μm the waveguide behaves as a slab waveguide with a thickness of the outer slab region (difference between thin film thickness and etch depth) with large FWHM of the spot size in the horizontal directions. It was seen for all etch depths that as the rib width increases the mode intensity profile in the horizontal direction reaches a minimum near 1 μm width and then increases in a linear fashion. As there is an increase in the etch depth of the rib, the confinement of the mode intensity increases with the mode profile in the horizontal direction becoming smaller. From the study, tailoring mode profiles for desired applications within Ta<sub>2</sub>O<sub>5</sub> material can be achieved by selecting the corresponding etch depth and rib width.

The simulation of using a planar Kerr lens element as a passive loss modulator to create a passive mode locked laser was also carried out to determine its feasibility. Kerr lens element was designed with a rib waveguide with inner film thickness of 1 μm, etch depth of 850 nm in Ta<sub>2</sub>O<sub>5</sub> material which propagated and launches light into an open slab region. The designed Kerr element was optimised to enhance the Kerr effect for self-focusing, and it was found that for longer Kerr

element length ( $K_L$ ), the focusing of the diffracting beam became more apparent while shorter  $K_L$  the effect was less as the input intensity is increased. By tailoring the structure's dimensions and input intensity of the laser beam, the effect of the Kerr lens device can be specifically designed for required modulation depth needed to cause modelocking.

*Fabrication and waveguide characterisation:* Using CMOS fabrication technologies Yb:Ta<sub>2</sub>O<sub>5</sub> films 1 μm thick were fabricated by RF magnetron sputtering from a powder-pressed target ( $\approx 6.2 \times 10^{20}$  ions/cm<sup>3</sup> Yb ions) onto a silicon wafer. Shallow rib channels with an etch depth of 150 nm were defined using a combination of photolithography and ion beam milling. The waveguides were encapsulated in thermally-grown silica under-cladding and RF magnetron sputtered silica over-cladding. In preparation for characterisation waveguide chips 10.8 mm long were cut and optically polished. The fabricated rib waveguide structure were found not to have vertical inner rib side walls but instead to have a double slope with an initial slope pitch of approximately 53° with the next connecting slope levelling out with the slab outer slab region with an angle of 5°. COMSOL simulations were carried out to investigate the effect the double sloped side wall would have on the size of mode intensity profile compared to straight vertical edged side wall. From the simulation and comparison it was found that the FWHM of the spot size for the sloped side wall in the vertical direction increased by  $\approx 0.5\%$  and in the horizontal direction increased by  $\approx 12\%$  for a rib 2 μm wide, with this increase reducing to 4% for larger rib widths of 10 μm. Characterisation in the form of imaging of the mode intensity profiles were carried out and analysed and showed partial agreement with simulations results for straight edged side wall waveguide with effects of PSF and sloped side walls causing increase in FWHM of the spot size. Propagation loss measurements were carried out through transmission measurements combined with the estimation of the launch efficiency of 1064 nm light into the waveguide. As discussed within this chapter the mode intensity profiles of fabricated rib waveguides did not closely follow the simulated mode intensity profiles, therefore the approximation of the launch efficiency will introduce an error as the calculation of coupling efficiency used the simulated mode intensity profiles. FP loss measurements were also presented. The loss measurements resulted in a large variation of the estimated propagation losses for the FP method, as losses ranged between 1.3 dB/cm to 12.7 dB/cm with the origin of this variability unknown.

*Ytterbium doped tantalum pentoxide waveguide spectroscopy:* Yb-doped Ta<sub>2</sub>O<sub>5</sub> material was for the first time investigated as a possible laser host, with spectroscopic properties such as absorption and emission cross-sections, gain bandwidth and excited-state lifetime studied [1]. An absorption spectroscopy was carried out on a 3 mm long Yb:Ta<sub>2</sub>O<sub>5</sub> waveguide by measuring the attenuation spectrum from white-light coupled directly into the waveguide from a SM fibre through butt-coupling at the end-facet. The light coupled out of the waveguide's end-facet was collected using a MMF and fed into an OSA. The resulting absorption spectrum showed a peak and sub-peak

absorption at wavelengths of 975 nm and 935 nm, with the corresponding absorption cross-section giving a peak cross-section of  $2.75 \pm 0.2 \times 10^{-20} \text{ cm}^2$  at 975 nm. A fluorescence spectrum was measured using a 977 nm laser source butt-coupled against the end-facet of the waveguide, with the fluorescence capture using a MMF positioned vertically above the waveguide's input inlet. This showed a broadband emission band from 990 nm to 1090 nm with a separate strong peak at 975 nm while being pumped at 971 nm. Using the McCumber analysis the emission cross-section was estimated to be  $2.90 \pm 0.7 \times 10^{-20} \text{ cm}^2$  at 975 nm. The excited-state life time was measured to be  $0.25 \pm 0.03 \text{ ms}$ . The material properties established from this study demonstrated that lasing is possible in Yb:Ta<sub>2</sub>O<sub>5</sub> and can be used in the development of on-chip planar waveguide lasers and mode-locked laser, as result of the combination of high material gain and broad bandwidth.

*Ytterbium doped tantalum pentoxide waveguide laser:* This thesis, for the first time presented integrated waveguide lasers in Yb:Ta<sub>2</sub>O<sub>5</sub>, using a 10.8 mm long chip and characterised for both mirrored and mirror-less cavities, with reflections occurring off the polished end-facets in the latter cases [2]. To establish an accurate estimate of the absorbed pump, the pump launch efficiency was calculated using knife-edge experiments to measure the launched pump beam waist and calculate an overlap integral of the pump beam waist and simulated waveguide mode intensity distribution. For a rib waveguide 5.4 μm wide lasing was observed between 1015 nm and 1030 nm when end-pumped with a 977 nm laser diode, leading to estimated 46% launch efficiency. The highest output power of 25 mW at a wavelength of 1025 nm was achieved with an absorbed pump power of 120 mW for a cavity formed by a high reflector mirror and an estimated 12% Fresnel reflection at the output. In this case, the absorbed pump power threshold and slope efficiency were measured to be  $\approx 30 \text{ mW}$  and  $\approx 26\%$  respectively. Tunability of lasing wavelength was demonstrated through tailoring the geometry of the rib waveguide by changing the width of the rib.

The work presented in this thesis is an effort towards establishing tantalum pentoxide as an all-purpose material for different photonic applications and devices. The work presented in this thesis focuses on the clear advantage of high index contrast of tantalum pentoxide with the demonstration of a waveguide laser in Yb:Ta<sub>2</sub>O<sub>5</sub> building a foundation for realising more complex optical devices on a single platform for fully integrated multi-function photonic circuits.

## 6.2 Future work

The work presented in this thesis on Yb:Ta<sub>2</sub>O<sub>5</sub> waveguide lasers can be used as the foundation for many future on-chip integrated devices for a wide range of applications. Some of them are listed below in addition to further improvements in fabrication and design aspects of the waveguide laser.

- *Improvement and optimisation of Ta<sub>2</sub>O<sub>5</sub> rib waveguides:* One of the main reasons why relatively high propagation losses are seen in the fabricated rib waveguides has to do with the quality of the etched side walls by the argon ion beam milling process. Limitations of

the etching process meant that etch depths greater than 350 nm and small waveguide features less than 2  $\mu\text{m}$  cause material reposition and rough side walls, leading to higher propagation losses. Alternative etching processes such as reactive ion etching (RIE) could be used to fabricate channels in  $\text{Ta}_2\text{O}_5$  with no re-deposition and lower damage to the surface of the thin-film. This is achieved because the etching process combines chemical and physical etching through a chemically reactive plasma and has been researched for dielectric films such as  $\text{Al}_2\text{O}_3$ ,  $\text{Y}_2\text{O}_3$  and  $\text{Ta}_2\text{O}_5$  [3], [4]. This leads to better selectivity and anisotropic etching for much lower loss waveguides with narrower, deeper etches with smoother vertical side walls.

- *Mode-locking with external saturable absorber:* As demonstrated in this work, continuous wave lasing was achievable in Yb-doped  $\text{Ta}_2\text{O}_5$  and combined with broad gain bandwidth gives a promising implication that modelocking is possible. Many waveguide lasers have been demonstrated with external semiconductor saturable absorber mirrors (SESAMs) used to force the waveguide into the modelocking regime by introducing a saturable loss within the laser cavity [5]–[7]. By replacing a cavity mirror affixed at the facet of the waveguide with a SESAM it is possible to create the necessary conditions of pulsed lasing to occur.
- *Fabrication and characterisation of planar Kerr lens elements for internal saturable absorber elements:* Kerr lens modelocked (KLM) lasers are pulsed lasers that use a passive saturable absorber based on the optical Kerr lensing phenomenon [8]. KLM systems have been mostly developed through free space laser systems where the propagating beam passes through a non-linear bulk material. Although KLM has the ability to produce short, fast pulses it is difficult to initiate modelocking in a self-starting manner as it is required for the cavity mirrors setup to have precise alignment, with these free space set-up arrangements suffering from stability issues from external influences [9]. The aim would be to miniaturise and integrate the Kerr lens element into an Yb-doped waveguide laser cavity, eliminating alignment and stability issues. The modelled behaviour of self-focusing in  $\text{Ta}_2\text{O}_5$  within this thesis is the initial design stage, with the next steps being fabrication of these elements in  $\text{Ta}_2\text{O}_5$  for many different lengths of the diffracting region and characterising the saturable and non-saturable losses of the devices.
- *Generation of frequency comb:* In recent times development of systems which generate optical frequency combs for spectroscopy of biomedical agents has pushed that research in a new direction. A frequency comb is a light source whose spectrum is a series of precisely spaced, sharp spectral lines enabling unprecedented measurement capabilities and new applications in a wide range of topics that include astronomical observations [10], precision spectroscopy [11], atomic clocks [12], molecular fingerprinting [13]. Frequency combs are used to detect and measure optical absorption spectra at each discrete frequency,

over a large bandwidth range. The gain of such a device is only limited by the transparency window of the resonator material (in the case of Ta<sub>2</sub>O<sub>5</sub> ranging from ~300 nm - 8 μm), and dispersion effects which are tailor-able in a channel waveguide system. The generation of a frequency comb of this can be tackled by through two methods. First utilizing the strong third-order non-linearity of Ta<sub>2</sub>O<sub>5</sub> by pumping a tuneable continuous wave laser and amplifier system into a pure Ta<sub>2</sub>O<sub>5</sub> ring resonator. The second method to tackle would be using a modelocked laser to supply a pulse to a resonator in Ta<sub>2</sub>O<sub>5</sub> where comb arises from the periodic train of pulses emitted.

### 6.3 Bibliography

- [1] A. Aghajani, G. S. Murugan, N. P. Sessions, S. J. Pearce, V. Apostolopoulos, and J. S. Wilkinson, "Spectroscopy of ytterbium-doped tantalum pentoxide rib waveguides on silicon," *Opt. Mater. Express*, vol. 4, no. 8, p. 1505, 2014.
- [2] A. Aghajani, G. S. Murugan, N. P. Sessions, V. Apostolopoulos, and J. S. Wilkinson, "Waveguide lasers in ytterbium-doped tantalum pentoxide on silicon," *Opt. Lett.*, vol. 40, no. 11, p. 2549, Jun. 2015.
- [3] J. D. B. Bradley, F. Ay, K. Wörhoff, and M. Pollnau, "Fabrication of low-loss channel waveguides in Al<sub>2</sub>O<sub>3</sub> and Y<sub>2</sub>O<sub>3</sub> layers by inductively coupled plasma reactive ion etching," *Appl. Phys. B*, vol. 89, no. 2–3, pp. 311–318, Nov. 2007.
- [4] K. P. Lee, K. B. Jung, R. K. Singh, S. J. Pearton, C. Hobbs, and P. Tobin, "Comparison of plasma chemistries for dry etching of Ta<sub>2</sub>O<sub>5</sub>," *J. Vac. Sci. Technol. A Vacuum, Surfaces, Film.*, vol. 18, no. 4, p. 1169, 2000.
- [5] U. Keller, "Recent developments in compact ultrafast lasers," *Nature*, vol. 424, no. 6950, pp. 831–838, Aug. 2003.
- [6] J. B. Schlager, B. E. Callicoatt, R. P. Mirin, and N. A. Sanford, "Passively mode-locked waveguide laser with low residual jitter," *IEEE Photonics Technol. Lett.*, vol. 14, no. 9, pp. 1351–1353, Sep. 2002.
- [7] A. Choudhary, A. A. Lagatsky, Z. Y. Zhang, K. J. Zhou, Q. Wang, R. A. Hogg, K. Pradeesh, E. U. Rafailov, W. Sibbett, C. T. A. Brown, and D. P. Shepherd, "A diode-pumped 1.5 μm waveguide laser mode-locked at 6.8 GHz by a quantum dot SESAM," *Laser Phys. Lett.*, vol. 10, no. 10, p. 105803, Oct. 2013.
- [8] T. Brabec, C. Spielmann, P. F. Curley, and F. Krausz, "Kerr lens mode locking," *Opt. Lett.*, vol. 17, no. 18, p. 1292, Sep. 1992.
- [9] D. E. Spence, P. N. Kean, and W. Sibbett, "60-fsec pulse generation from a self-mode-locked Ti:sapphire laser," *Opt. Lett.*, vol. 16, no. 1, p. 42, Jan. 1991.
- [10] T. Steinmetz, T. Wilken, C. Araujo-Hauck, R. Holzwarth, T. W. Hansch, L. Pasquini, A. Manescau, S. D'Odorico, M. T. Murphy, T. Kentischer, W. Schmidt, and T. Udem, "Laser frequency combs for astronomical observations," *Science*, vol. 321, no. 5894, pp. 1335–1337, Sep. 2008.

- [11] M. J. Thorpe and J. Ye, “Cavity-enhanced direct frequency comb spectroscopy,” *Appl. Phys. B*, vol. 91, no. 3–4, pp. 397–414, Jun. 2008.
- [12] R. Holzwarth, M. Zimmermann, T. Udem, and T. W. Hansch, “Optical clockworks and the measurement of laser frequencies with a mode-locked frequency comb,” *IEEE J. Quantum Electron.*, vol. 37, no. 12, pp. 1493–1501, 2001.
- [13] A. G. Griffith, R. K. W. Lau, J. Cardenas, Y. Okawachi, A. Mohanty, R. Fain, Y. H. D. Lee, M. Yu, C. T. Phare, C. B. Poitras, A. L. Gaeta, and M. Lipson, “Silicon-chip mid-infrared frequency comb generation,” *Nat. Commun.*, vol. 6, p. 6299, Feb. 2015.

# Appendix A

## Matlab code for determination of FWHM of Gaussian beam profile

This matlab function and code is used to find the full width at half maximum FWHM of a Gaussian beam intensity profile.

### FWHM function code

```
function width = fwhm1(x,y)
% function width = fwhm(x,y)
% Full-Width at Half-Maximum (FWHM) of the waveform y(x) and its polarity.
% The FWHM result in 'width' will be in units of 'x'
% Rev 1.2, April 2006 (Patrick Egan)
y = y/max(y);
N = length(y);
lev50 = 0.5;
if y(1) < lev50          % find index of center (max or min) of pulse
    [garbage,centerindex]=max(y);
    Pol = +1;
    disp('Pulse Polarity = Positive')
else
    [garbage,centerindex]=min(y);
    Pol = -1;
    disp('Pulse Polarity = Negative')
end
i = 2;
while sign(y(i)-lev50) == sign(y(i-1)-lev50)
    i = i+1;
end %first crossing is between v(i-1) & v(i)
interp = (lev50-y(i-1)) / (y(i)-y(i-1));
tlead = x(i-1) + interp*(x(i)-x(i-1));
i = centerindex+1; %start search for next crossing at centre
while ((sign(y(i)-lev50) == sign(y(i-1)-lev50)) & (i <= N-1))
```

---

```

        i = i+1;
end
if i ~= N
    Ptype = 1;
    disp('Pulse is Impulse or Rectangular with 2 edges')
    interp = (lev50-y(i-1)) / (y(i)-y(i-1));
    ttrail = x(i-1) + interp*(x(i)-x(i-1));
    width = ttrail - tlead;
else
    Ptype = 2;
    disp('Step-Like Pulse, no second edge')
    ttrail = NaN;
    width = NaN;
end

```

#### Code for running FWHM function with data

```

clc; close all; clear
clear pd
pd.p = [...
-----
Enter data here!!
x-data      y-data
-----
];
pd.x = pd.p(1,:);
pd.y = pd.p(2,:).^2;
pd = rmfield(pd,'p');
plot(pd.x,pd.y);
width = fwhm1(pd.x,pd.y);

```

## Appendix B

### Background theory of knife edge method

This section describes the background theory of the Knife edge measurement technique. To characterize the intensity profiles of a Gaussian beam from the data collected requires an expression for the transmitted power vs. position of the razor blade across the beam. Beginning with observing a Gaussian beam (propagating in the  $z$  direction) in the  $x, y$  plane given by [1]

$$I(x, y, z) = \frac{2P_0}{\pi w(z)} \exp\left[-\frac{2(x^2 + y^2)}{w(z)^2}\right] \quad (6.1)$$

where  $w(z)$  is the beam radius measured at the  $1/e^2$  of the beam from its peak intensity and  $P_0$  is the power of the beam given by the double integral:

$$P_0 = \int_{-\infty}^{\infty} \int_{-\infty}^{\infty} I(x, y) dx dy \quad (6.2)$$

If part of the beam is covered by the razor blade, the transmitted power meter is given by the total power,  $P_0$  reduced by the covered power  $P_c$ . Hence the transmitted power can be expressed as

$$P_T = P_0 - P_c \quad (6.3)$$

$$= \int_{-\infty}^{\infty} dy \int_{-\infty}^{\infty} dx' (x', y, z) - \int_{-\infty}^{\infty} dy \int_{-\infty}^x dx' (x', y, z) \quad (6.4)$$

$$= \int_{-\infty}^{\infty} dy \int_x^{\infty} dx' (x', y, z) \quad (6.5)$$

$$= \frac{2P_0}{\pi w(z)} \int_{-\infty}^{\infty} dy \int_x^{\infty} dx' \exp\left[-\frac{2(x'^2 + y^2)}{w(z)^2}\right] \quad (6.6)$$

$$\therefore P_T = \frac{P_0}{2} \left[1 - \operatorname{erf}\left(\frac{\sqrt{2}x}{w(x)}\right)\right] = \frac{P_0}{2} \left[\operatorname{erfc}\left(\frac{\sqrt{2}x + c}{w(x)}\right)\right] \quad (6.7)$$

Where  $c$  is additional variable inserted as an offset of the curve in the  $x$  direction,  $\operatorname{erf}(x)$  is the Gaussian error function and  $\operatorname{erfc}(x)$  is the complementary error function defined as

$$\operatorname{erf}(x) = \frac{2}{\sqrt{\pi}} \int_0^x e^{-t^2} dt \quad (6.8)$$

$$\operatorname{erfc}(x) = 1 - \operatorname{erf}(x) \quad (6.9)$$

$$= \frac{2}{\sqrt{\pi}} \int_x^\infty e^{-t^2} dt = e^{-x^2} \operatorname{erfc}(x) \quad (6.10)$$

Figure B.1 shows the knife edge experimental data for Gaussian beams at various positions from the lens, with data taken at 10  $\mu\text{m}$  intervals. The scans at a distance of 0.5 mm, 1.0 mm, 2.5 mm and 3.0 mm from the lens have the expected S-shaped curve but require the razor blade to travel further to fully cover the beam than scans at a distance of 1.5 mm and 2.0 mm. This means that the beam waist reaches a minimum between 1.5 mm and 2.0 mm.

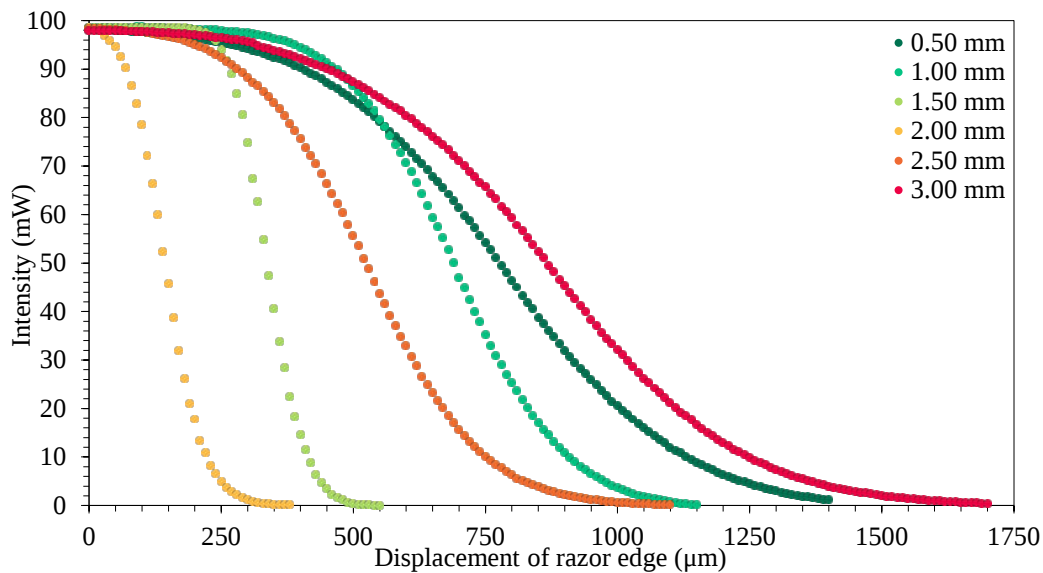


Figure B.1 Knife edge scans at various distances from the input aspheric lens.

- [1] J. Magnes, D. Odera, J. Hartke, M. Fountain, L. Florence, and V. Davis, “Quantitative and qualitative study of gaussian beam visualization techniques,” *Arxiv Prepr. physics/*, no. 2, pp. 1–5, 2006.